Dissertation

submitted to the

Combined Faculties of the Natural Sciences and Mathematics

of the Ruperto-Carola-University of Heidelberg, Germany

for the degree of

Doctor of Natural Science

Put forward by

Diplom-Physiker Kai-Martin Dittkrist

Born in: Mannheim, Germany

Oral Examination: 02.02.2016

Aspects of planet formation

A model of migration

and

SADFACE:

a 1-dimensional vertically integrated disk model for planet population synthesis calculations

Referees: Priv.-Doz. Dr. Hubert Klahr

Prof. Dr. Andreas Quirrenbach

Zusammenfassung

Diese Dissertation diskutiert zwei Aspekte von Planetenentstehung. Zum einen präsentiert sie ein Modell der Planetenmigration während sich der Planet noch in der Staub- und Gasscheibe befindet und dort wächst. Zum Zweiten enthält sie ein Modell, das Sternen- und Scheibenentstehung und -entwicklung verbindet und zukünftig für Planetenpopulationssynthesen genutzt werden soll. Resultat des ersten Teils ist, das mit der Einbindung von neuesten Resultaten von Typ I Migration, nämlich mögliche Wanderung von leichten Planeten in der Scheibe nach aussen, die Verwendung eines künstlichen Faktors zu Reduktion von Typ I Migration unnötig wird. Wir finden zwischen zwei und dreimal so viele "kalte" Planeten mit dem neuen Modell im Vergleich zum Alten. Resultat des zweiten Teils sind Wahrscheinlichkeiten für Kombination von Anfangsbedingungen für Scheiben und Sternenentstehung. Der Vergleich mit Beobachtungsdaten zeigt, dass das Modell diese gut beschreiben kann. Die Anfangsbedingungen stimmen im Fall der Wolkenmasse und Temperatur auch mit den Vorhersagen des Modells überein.

Abstract

We discuss two aspects of planet formation in this thesis. At first we present a model of type I migration which includes new results of outward migration of low mass planets. The second part contains SADFACE, a 1-dimensional vertically integrated disk model for planet population synthesis calculations. Results of the first part is that with the inclusion of thus modes of outward migration no artificial fudge factor to reduce the speed of type I migration is needed. We find two to three times as many ”cold” planets when we include outward migration than without. Results of the second part is that in the scope of the model we can find initial conditions that fit observed disks quite well. We also present likelihood of initial conditions which can be further used for planet population synthesis calculations. We also find that rotation and temperature of a cloud are correlated and can not be independently chosen.

Contents

List of Figures

List of Tables

Chapter 1

Introduction

Since 1995, when the first planet orbiting a star in close orbits of only a few days was observed (Mayor and Queloz, 1995) by radial velocity measurements, over 2030 exoplanets around 1288 stars (http://exoplanet.eu) have been found with various methods. While first only single planets orbiting a star were found, due to the limitations of the methods, new data, mainly transit measurements, shows that many stars host multiple planets like our own solar system.

Those systems, and single planets, spawn a huge range of properties. Some planets being much closer to their host star than Mercury is to our sun, weighting a few Jupiter masses, while others are smaller than earth (e.g. Kepler-444, Campante et al., 2015). Multiple Jupiter like planets in one system were also observed (e.g. HR8799, Marois et al., 2010). The formation of such diverse planetary systems stems from a diverse birth environment, which is thought to be disks of gas and dust surrounding stars during their early phases of evolution.

The theory of star formation starts with cold cores of gas and dust mostly in groups, clusters or filaments found in molecular clouds (Lada and Lada, 2003). Those clouds are at pressure equilibrium before they get disturbed and start to collapse. The range of properties of those collapsing clouds is understood to create the variety in observed disks (Myers, 2008). This collapsing gas does not fall directly onto one central point due to conservation of angular momentum. Even a slight rotation of those clouds give them enough angular momentum that most gas will fall first onto the disk surrounding the central protostar before it gets accreted onto it. This first phase of this infall onto the protostar is shielded from observation by the surrounding gas. After the cloud collapsed onto the star-disk system the disk contains most of the angular momentum. This angular momentum has to be transported through the disk away from the star to let the gas of the disks fall further onto the star. This accretion of gas onto the star is widely observed in star forming regions (Natta et al., 2006).

The physical source for the transport of angular momentum in the disk is turbulence of some kind (gravo turbulence, MRI or hydrodynamic instabilities like the baroclinic instability) in the disk. While most of this gas gets accreted onto the star some of it forms the observed planets. There are two leading theories. Either the disk is massive enough that it fragments further by gravitational instability and some

of those fragments collapse directly in massive gaseous planets (Boss, 1997). This is probably true in the outer regions of disks. The second theory (see also D'Angelo et al., 2010; Mordasini et al., 2010) starts with the dust contained in the gas. It starts to grow from (sub)-micrometer to millimeter sized grains (Testi et al., 2014) while it settles to the midplane and drifts inward due to the difference in orbital speed between the gas grains and gas. From thus grains, planetesimals form in some way, which further grow by gravitational attraction to form planet cores and rocky planets.

If these planet cores grow fast enough to reach at least a few Earth masses, while the gaseous disk is still present, it can start to bind gas to itself and grow an envelope, which collapses further onto the core and form the gas giants. During the formation of thus planets the protoplanet interacts with the disk. Gas gets deflected by the gravity of the core and the corresponding torques lead to a change in semimajor axis of the planet. The planet migrates mostly inward, yet under some circumstances, depending on the mass of the planet the the thermodynamic state of the disk, it can also be pushed outwards. If the planets becomes more massive these torques can alter the shape of the disk to form gaps which can be found in some disks.

Finally, while accretion onto the star and planets accounts for the most of mass loss of the disk, a variety of other processes are also thought to help with the dispersal of the protoplanetary disk. Magnetic fields from the star or generated in the disk itself launches jets or disk winds to remove mass and angular momentum from the system. Also ultraviolet radiation from the accretion onto the star or from stars in the vicinity can evaporate mass from the surface of the disk (Pudritz et al., 2007).

Planet population synthesis calculation (e.g. Mordasini et al., 2009a; Ida and Lin, 2004) tries to capture most of those processes, sometimes in reduced or simplified versions, into one model to create populations of planets that can be compared statistically with observed planets. Changing one aspect of the model changes the population, thus giving a handle on how important a process is to the whole picture of understanding planet formation.

1.1 About this Thesis

This thesis is twofold. In the first part we present our paper on a model of planet migration (Dittkrist et al., 2014). It includes inward and outward movement in type I migration, the change of semimajor axis of planets to small to open a gap in the disk, transition into the slower type II migration (for planets large enough to open a gap) and type II migration itself. This model is included in planet population synthesis calculations to study the effect of the outward migration on the distribution of an simulated population of planets.

In the second part we will present SADFACE (star and disk formation and concurrent evolution): a 1-dimensional vertically integrated disk model for planet population synthesis calculations. It includes the processes mentioned above for disk and star formation out of infalling clouds. The aim of this model is be included into the planet population synthesis model and improve on some aspects of the current one.

In Chapter 3 we will present a model to calculate the midplane temperature of a protoplanetary disk. Chapter 4 includes descriptions of the other different parts of the model, like stellar model or photoevaporation. In Chapter 5 we present the results of disk evolution for a grid of different initial conditions and comparison of thus results with observed disks. Chapter 6 contains a short summary, conclusion and outlook.

Chapter 2

Impacts of planet migration models on planetary populations

In the following chapter I present my first published paper (Dittkrist et al., 2014) word by word.

2.1 abstract

Several recent studies have found that planet migration in adiabatic disks differs significantly from migration in isothermal disks. Depending on the thermodynamic conditions, that is, the effectiveness of radiative cooling, and on the radial surface density profile, planets migrate inward or outward. Clearly, this will influence the semimajor axis-to-mass distribution of planets predicted by population-synthesis simulations.

Our goal is to study the global effects of radiative cooling, viscous torque desaturation, gap opening and stellar irradiation on the tidal migration of a synthetic planet population.

We combined results from several analytical studies and 3D hydrodynamic simulations in a new semi-analytical migration model for the application in our planet population synthesis calculations.

We find a good agreement of our model with torques obtained in 3D radiative hydrodynamic simulations. A typical disk has three convergence zones to which migrating planets move from the in- and outside. This strongly affects the migration behavior of low-mass planets. Interestingly, this leads to a slow type II like migration behavior for low-mass planets captured in these zones even without an ad hoc migration rate reduction factor or a yet-to-be-defined halting mechanism. This means that the new prescription of migration that includes nonisothermal effects makes the previously widely used artificial migration rate reduction factor obsolete. Outward migration in parts of a disk helps some planets to survive long enough to become massive. The convergence zones lead to potentially observable accumulations of low-mass planets at certain semimajor axes. Our results indicate that more studies of the

mass at which the corotation torque saturates are needed since its value has a main impact on the properties of planet populations.

2.2 Introduction

The huge diversity found in the properties of extrasolar planets is challenging to reproduce with global theoretical planet formation models. The goal of such a model is to explain all the different planet types, which range from low-mass rocky planets such as Kepler-10 b (Batalha et al., 2011) and multiplanet systems like our solar system to high-mass planets orbiting far from their star, such as NR 8977 (Marois et al., 2008).

The only way to study this problem is to use the results of global formation and evolution models and to compare them statistically with the steadily increasing number of known planets and their physical properties. This is done in planet populations synthesis calculations, in which the evolution of one or several planets and the harboring protoplanetary disk is calculated at the same time in Monte Carlo simulations to create whole populations of planets. Several groups presented studies based on this method, for example, Ida and Lin (2004),Ida and Lin (2010), Thommes et al. (2008),Miguel and Brunini (2008),Hellary and Nelson (2012), or by our group, Mordasini et al. (2009a),Mordasini et al. (2009b),Mordasini et al. (2012b),Mordasini et al. (2012a), and Alibert et al. (2011).

One general result found in all these models is that giant planets close to the star ("hot" Jupiters) do not form *insitu*: the extrapolation of disk properties found at larger distances to small distances indicates that there is probably not enough solid material close-in to form a sufficiently large core that whould be able to accrete gas. The amount of material a core can accrete locally is given by the isolation mass $M_{\rm iso}$. According to the empirical minimum-mass solar nebula model (MMSN), the isolation mass is only a fraction of the Earth mass ($M_\oplus$) inside of 1 AU (Ida and Lin, 2004). Therefore an increase of solid matter by roughly two orders of magnitude compared with the MMSN would be needed (Ida and Lin, 2004). This means that to explain the close-in "hot" Jupiters, they would have to form initially at larger separations from the star and move inward by some mechanism (e.g., planet-planet scattering (Rasio and Ford, 1996), Kozai mechanism (Nagasawa et al., 2008), or tidal interactions with the gas disk (Goldreich and Tremaine, 1980; Tanaka et al., 2002)). In the planet formation model used in this work, we consider only one core per disk, which means that only migration caused by tidal interactions can be studied. This migration is generally described by two different regimes that depend on the mass of the protoplanet. The first is type I migration for low-mass planets, which are too small to form a gap in the disk, and the second is type II migration for planets that open a gap (D'Angelo et al., 2002).

In our previous work (e.g. , Mordasini et al., 2009a; Alibert et al., 2011), we used the results obtained for isothermal disks reported in Tanaka et al. (2002) to calculate type I migration rates. The migration rate in this model only depends on the disk surface density profile and not on the temperature profile of the disk because it assumes a globally isothermal disk. Migration rates obtained with this model always lead to

rapid inward migration in disks with profiles similar to the MMSN. We showed (Mordasini et al., 2009a) that to obtain a synthetic population compatible with observations, one needs to artificially reduce the isothermal type I migration rate by a large factor. Ida and Lin (2004) used a similar type I migration prescription and found necessary reduction factors of $\lesssim 0.1$ for the migration rate.

Recent studies of type I migration in 2D or 3D hydrodynamical simulations also found outward migration for some masses or semimajor axes, depending on the disk temperature structure (Masset et al., 2006; Paardekooper and Mellema, 2008; Kley et al., 2009). More analytical work derived a formulation that could be used in planet population synthesis calculations (Casoli and Masset, 2009; Masset and Casoli, 2009, 2010). Finally, Paardekooper et al. (2010) derived a formalism for type I migration in adiabatic or locally isothermal disks and improved this even more in Paardekooper et al. (2011).

In the present work we describe a semi-analytical type I migration model that can be applied to a wider range of planet and disk properties than that of Paardekooper et al. (2011). For this we used the adiabatic and locally isothermal migration equations from Paardekooper et al. (2010) and ratios of relevant time scales to determine the transition between different regimes. We then studied the global consequences of the physics included in the migration model in new sets of population synthesis calculations.

As an overview of this work, the new semi-analytical model we created is introduced in Section 2, where we also compare torques obtained with this model with torques obtained with the model of Paardekooper et al. (2011) and data obtained in 3D radiative hydrodynamic simulations of Kley et al. (2009) and Bitsch and Kley (2011). We discuss in Section 3 a reference synthetic planet population calculated with the nominal model, and in Section 4 we study the effect of different migration models on planetary populations. In Section 5 we draw our conclusions and summarize our results.

2.3 Migration model

The migration module in our planet formation model (Alibert et al., 2004) distinguishes three main regimes, type I, disk-dominated type II, and planet-dominated type II migration (Armitage and Rice, 2005). Low-mass planets up to typically a few 10 Earth masses migrate in the type I regime, followed by migration in disk-dominated type II regime for more massive planets, which finally pass into planet-dominated type II migration when they reach masses of typically 100-200 $M_\oplus$. We first describe our improvements to the description of the type II regime and introduce the new type I migration model afterwards.

2.3.1 Type II model and outward migration

In the old model, the type II migration rate was calculated using the equilibrium flux of gas in the disk, which was always assumed to be directed inward (Mordasini et al., 2009a). Now the direction and rate of type II migration is numerically calculated by considering the radial velocity $v_{\rm gas}$ of the (nonequilibrium) flux of gas at the position of the planet. It therefore allows outward migration if the planet is in a part of the disk where the gas is flowing outward (Veras and Armitage, 2004). The planetary migration rate is then

$$\dot{a}_{\rm p,T2} = v_{\rm gas} \times {\rm Min}(1, 2\Sigma a_{\rm p}^2 / M_{\rm p}), \tag{2.1}$$

where $a_{\rm p}$ is the semimajor axis of the planet, $M_{\rm p}$ is its mass, and Σ is the gas surface density.

This mechanism has been invoked to explain the formation of exoplanets with semimajor axes larger than 20 AU, which cannot have formed in situ via the core accretion model (Veras and Armitage, 2004). However, we find in the syntheses using the nonequilibrium model that outward migration in type II is seldom important, and no large-scale net outward migration over more than $\sim 1\ AU$ typically occurs due to it. The reason is twofold:

The radius of velocity reversal (or of maximum viscous couple) $R_{\rm MVC}$ (Lynden-Bell and Pringle, 1974) is relatively close-in only early in the disk evolution. But, at these early times, the planets have usually not yet grown to a mass regime in which they migrate via type II. The evolution of the disk leads to the subsequent recession of $R_{\rm MVC}$ to larger radii. This occurs faster than the growth of the planets. Therefore type II outward migration is a very rare event during the spreading phase of the disk: at the moment planets have grown massive enough to migrate in type II, they are most of the time already located inside the $R_{\rm MVC}$.

Another chance of outward migration exists towards the end of the disk lifetime, when parts of the disk flow outward because mass is removed at the outer border due to external photoevaporation. The gas surface densities, however, are typically already quite low at the position of the planet at this moment, so that the reduction factor of the planet's migration rate relative to the viscous velocity $\propto \Sigma a_{\rm planet}^2 / M_{\rm planet}$ (see Alibert et al., 2005) is low as well, leading again to only modest amounts of outward migration. As in the original model, we assumed a linear reduction factor if $M_{\rm planet} > 2\Sigma a_{\rm planet}^2$ ("fully suppressed" planet-dominated type II), because this agrees a better with hydrodynamical simulations than a square-root dependence on the planetary mass (Alexander and Armitage, 2009). Outward migration during effective photoevaporation is additionally limited because the remaining disk-lifetime is short.

2.3.2 Type I migration regimes

Here we discuss the migration of low-mass planets below a few tens of Earth masses. As mentioned above, one of the problems with the original description of orbital migration of low-mass planets is the short time scale found in isothermal type I migration (Tanaka et al., 2002), which resulted in too many close-in planets in planet population

synthesis calculations (see also the comparison in Section 2.5.1). These rates had to be artificially reduced by correction factors to produce enough "cold" giant planets at larger semimajor axes (Mordasini et al., 2009b; Ida and Lin, 2008) to fit the observations.

On the other hand, Paardekooper and Mellema (2006) and Kley et al. (2009) showed that migration of small-mass bodies is not always inward because in a non-isothermal disk migration can be directed outward for some masses. Outward migration in the Type I regime can also occur in isothermal disks if full MHD turbulence is considered (see also Uribe et al., 2011; Guilet et al., 2013), but these new effects are not considered here because they need to be studied in more detail more studies before they can be parametrized.

Recently, Paardekooper et al. (2010) derived semi-analytical formulas for migration in the limiting case of adiabatic disks. Here we combine different formulas that are valid in different thermodynamical regimes into a model that can be applied to the wide range of planet masses and thermodynamic properties of the disk that are needed for our population-synthesis models.

Type I fit formula

Nonisothermal migration rates are more complex than isothermal rates. Generally, the gravitational interactions of the planet and the gas disk can lead to three characteristic flow regions that produce different types of torques:

- Lindblad torques:

  Gas sufficiently far from the planet is only slightly perturbed and orbits the star on nearly circular orbits inside or outside the planet's orbit. The gravitational interaction generated by the planet in the regions outside and inside the corotation region produces the Lindblad torques.

- Corotation torque:

  If the orbit of a gas parcel is closer to the planet, its flow is more and more deflected, until it passes the planet's orbit in front or behind the planet. Thus it forms so-called horseshoe orbits (see Fig. 2.1). The gas in the horseshoe orbits produces by deflection the so-called horseshoe drag or corotation torque. The strength of this torque depends on the thermodynamic regime of the interaction between the planet and the disk and the mass of the planet.

For typical properties (radially decreasing density and temperature) of the disk the Lindblad torques lead to inward migration, whereas the isolated torques from the corotation region can result in either inward or outward migration. For certain thermal and surface density profiles in the disk, these torques can be stronger than the Lindblad torques. Thus the combination of Lindblad and corotation torques can lead to either inward or outward migration, depending on their relative strength, which is determined by the disk properties.

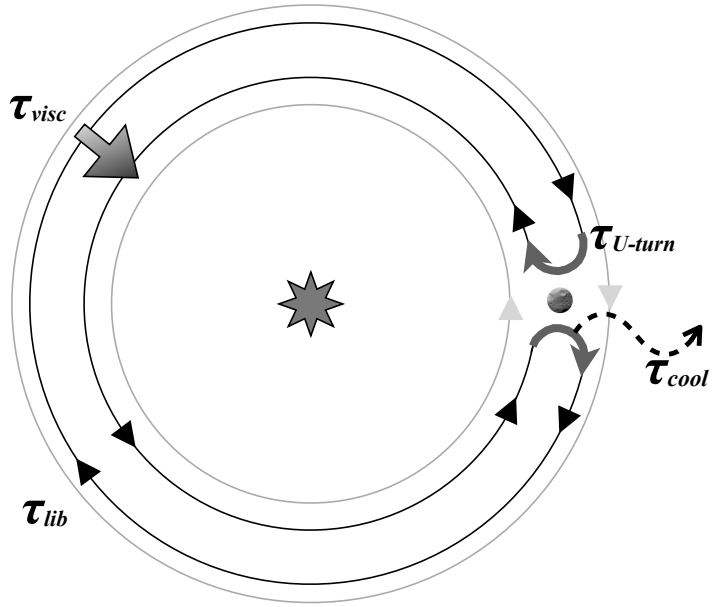

Figure 2.1 Schematic representation of the relevant time scales involved in type I migration. Flow lines of gas parcels are indicated in a system of reference that rotates with the planet. The planet is indicated on the right. In the center is the star. Close to the planet, the flow lines bend and make a u-turn during a time equal $\tau_{\mathrm{u-turn}}$. During that time, the gas on the flow lines cool on a time scale τ_{cool}. One full libration around the planet (indicated by the black lines) takes a libration time, τ_{lib}. During this time, viscosity acts on a viscous time scale τ_{visc}. The corotation region lies between the two black lines. Inside and outside this region, gas parcels do not make u-turns, but have a velocity relative to the planet because of to the Keplerian sheer (gray lines).

The total torque Γ can be expressed in the following way, as shown in Tanaka et al. (2002), Paardekooper et al. (2010) or Masset and Casoli (2010):

$$\tilde{\Gamma} = \frac{\Gamma}{M_\mathrm{p}} = \tilde{C} a_\mathrm{p}^2 \Omega_\mathrm{p}^2 \quad \text{, where} \tag{2.2}$$

$$\tilde{C} = C \frac{a_\mathrm{p}^2}{h^2} \Sigma_\mathrm{p} \frac{M_\mathrm{p}}{M_\mathrm{star}^2} = \frac{\dot{a}_p}{2 a_\mathrm{p} \Omega_\mathrm{p}} = \frac{1}{4\pi N_\mathrm{orb}} = \frac{\tau_\mathrm{orb}}{4\pi \tau_\mathrm{mig}}, \tag{2.3}$$

In these equation, $\tilde{\Gamma}$ is the specific torque (torque per unit mass). With a small p we denote all quantities of or at the position of the planet. M_p is the total mass of the planet and a_p the semimajor axis, while M_star is the mass of the star, $h = H/a$ is the aspect ratio of the disk with a vertical scale height H. Ω_p is the Keplerian frequency of the planet and Σ_p the gas surface density. The dimensionless factor C in the second part of Eq. 2.3 gives the direction and strength of the migration and is discussed below for different thermodynamical regimes (Sect. 2.3.2). The dimensionless number $\tilde{C}$ is proportional to the migration rate $\dot{a}_p$ and inversely proportional to the number of orbits needed for a planet to migrate over the distance of its semimajor axis N_orb. It is also proportional to the ratio of the two time scales for migration τ_mig and orbital motion τ_orb

Additional parameters in the following equations are β_Σ as the local power-law exponent of the gas surface density ($\Sigma \propto r^{\beta_\Sigma}$), β_T the local power-law exponent of the temperature ($T \propto r^{\beta_\mathrm{T}}$), and γ the adiabatic index (ratio of the heat capacities) of the gas.

Depending on the properties of the disk, C is a combination of various torque contributions of variable importance. Before we describe how we combined the contributions, we introduce expressions for their individual strength.

Paardekooper et al. (2010) derived that the Lindblad torque in an adiabatic disk is proportional to (their Eq. 47, part 1)

$$C_\mathrm{Lind} = \frac{1}{\gamma} \left(-2.5 + 1.7\beta_\mathrm{T} - 0.1\beta_\Sigma\right). \tag{2.4}$$

They also found that the horseshoe drag in the adiabatic case is proportional to (their Eq. 47, part 2)

$$C_\mathrm{HS,adia} = \frac{1}{\gamma} \left(1.65 + \beta_\Sigma(9 - 7.9/\gamma) - 7.9\beta_\mathrm{T}/\gamma\right). \tag{2.5}$$

The coefficient C in the adiabatic regime due to the combination of the Lindblad and corotation torques is

$$C_\mathrm{adia} = C_\mathrm{Lind} + C_\mathrm{HS,adia}. \tag{2.6}$$

Paardekooper et al. (2010) also found that the total torque in a locally isothermal regime, where the temperature T is constant in time but not with semimajor axis, is proportional to (their Eq. 49)

$$C_\mathrm{loc} = -0.85 + 0.9\beta_\mathrm{T} + \beta_\Sigma. \tag{2.7}$$

Subtracting from this the Lindblad torque in the adiabatic regime, but setting $\gamma = 1$ (compare Paardekooper et al. (2010) Sect. 5.4 [1]), one finds the horseshoe drag part in the locally isothermal regime as

$$C_{\mathrm{HS,loc}} = 1.65 - 0.8\beta_{\mathrm{T}} + 1.1\beta_{\Sigma}. \tag{2.8}$$

Compared with Eq. 2.4, Masset and Casoli (2010) derived a partially different Lindblad torque. We study the effect of this weaker Lindblad torque in Sect. 2.5.2.

$$C_{\mathrm{Lind,2}} = \frac{1}{\gamma}\left(-2.5 + 0.5\beta_{\mathrm{T}} - 0.1\beta_{\Sigma}\right). \tag{2.9}$$

2.3.3 Time Scales

The proper mix of the above described torque contributions can be determined by investigating the relevant time scales. For instance a disk behaving adiabatically produces a different torque than a locally isothermal one. Here the relevant time scales are the cooling time in comparison to the dynamic time.

To decide in which subtype the planet belongs to, we compared four characteristic time scales in total. The different time scales are schematically shown in Figure 2.1. In all the following estimates of the time scale, the important characteristic length scale is the width of the horseshoe region x_{s} given as (Masset et al., 2006; Baruteau and Masset, 2008; Paardekooper et al., 2010)

$$x_{\mathrm{s}} = 1.16 a_{\mathrm{p}} \sqrt{\frac{q}{h\sqrt{\gamma}}}. \tag{2.10}$$

In this equation q is the ratio of the planet mass to the stellar mass.

The first two time scales we compared are the cooling time and the u-turn time to distinguish between the locally isothermal and the adiabatic regime. The u-turn time is the time a gas particle needs to undergo one turn in front or behind the planet. Its value is approximately given as (Baruteau and Masset, 2008)

$$\tau_{\mathrm{u-turn}} = \frac{64 x_{\mathrm{s}} h^2}{9 q a_{\mathrm{p}} \Omega_{\mathrm{p}}}. \tag{2.11}$$

The cooling time of a gas blob undergoing a turn is calculated by solving the 1D equation (Kley et al., 2009)

$$\frac{dT}{dt} = -\frac{1}{\rho C_{\mathrm{V}}} \frac{\partial}{\partial a}\left(F\right), \tag{2.12}$$

where F is the heat flux, ρ the gas density, and C_{V} the heat capacity at constant volume. We assumed a cooling over the length l_{cool}, which is the minimum of H, and x_{s}, which corresponds to either horizontal cooling over the width of the horseshoe region or vertical cooling through the disk. The flux F in the optically thin case, when $\rho\kappa l_{\mathrm{cool}} < \sqrt{1/8}$ is $F = \tau\sigma T^4$, and in the optically thick case in the diffusion description $F =$

[1] One infers the locally isothermal regime by taking the limit $\gamma \to 1$, which invokes infinitely efficient thermal diffusion.

$\frac{4acT^3}{3\rho\kappa}\frac{\partial T}{\partial a}$ (Kley et al., 2009). This means that we have two different types of the cooling time scale with a smooth transition when the optical depth is $1/\sqrt{8}$

$$\tau_{\rm cool} = \frac{l_{\rm cool}\rho C_V}{8\sigma T^3}\left(8\rho\kappa l_{\rm cool} + \frac{1}{\rho\kappa l_{\rm cool}}\right). \tag{2.13}$$

In a similar way we compared the viscous time scale and the libration time scale to find out whether the horseshoe drag is saturated or not (Masset and Casoli, 2010). The viscous time scale is

$$\tau_{\rm visc} = \frac{x_{\rm s}^2}{\nu}, \tag{2.14}$$

while the libration time is given as (Baruteau and Masset, 2008)

$$\tau_{\rm lib} = \frac{8\pi a_{\rm p}}{3\Omega_{\rm p} x_{\rm s}}. \tag{2.15}$$

We denote the ratios of the relevant time scales as

$$s_1 = f_{\rm cool}\frac{\tau_{\rm cool}}{\tau_{\rm u-turn}} \tag{2.16}$$

and

$$s_2 = f_{\rm visc}\frac{\tau_{\rm visc}}{\tau_{\rm lib}}. \tag{2.17}$$

An equivalent approach can also be found in Casoli and Masset (2009) and Masset and Casoli (2009).

These time scales are typically order-of-magnitude estimates. Therefore, we introduced two factors, $f_{\rm cool}$ and $f_{\rm visc}$, of order unity to adjust the point of transition between different regimes to obtain a better agreement with radiative hydrodynamic simulations. In this work we set $f_{\rm cool} = 1.0$, since this proved toagree well with numerical results of migration rates, as we show in Section 2.3.5. There, we also study the influence of various values of $f_{\rm visc}$. In general, we find that in nonirradiated α disks, planets transit from the locally isothermal into the adiabatic regime before the corotation torque saturates (Sect. 2.4.5).

We also note that for a given h, the ratio of the u-turn time and libration time is constant:

$$\tau_{\rm u-turn} = \frac{1.16^2 8}{3\pi}\frac{h}{\sqrt{\gamma}}\tau_{\rm lib} \approx 1.14\frac{h}{\sqrt{\gamma}}\tau_{\rm lib}. \tag{2.18}$$

2.3.4 Type I migration formula

To combine the migration rates of these different regimes we defined an arbitrary transition function z to obtain a smooth shift from the locally isothermal to the adiabatic regime as a function of the variable s_1:

$$z(s_1) = \frac{1}{1+s_1^b}, \tag{2.19}$$

which has the properties that for $s_1 \rightarrow 0, z(s_1) \rightarrow 1$ and for $s_1 \rightarrow \infty, z(s_1) \rightarrow 0$. Furthermore, depending on the value of b, the transition from 1 to 0 occurs more or less quickly around $s_1 = 1$. Therefore, uncertainties in overlap of different regimes can be approximated with a lower b value. Additionally, the continuity of the transition function allows one to use longer numerical time steps in a simulation when the planet is close to the transition from one regime into another.

For individual transitions (e.g., locally isothermal to adiabatic, or type I into type II), other studies (Paardekooper et al. (2011); Masset and Casoli (2010)) derived physically motivated transition functions. But the comparison of physically motivated transition functions Paardekooper et al. (2011) with our simple transition function defined above shows little difference in population synthesis models (see Section 2.5.1). We set $b = 4.0$, but the actual value of b is again not very important for the global outcome seen in a population if $1.5 \lesssim b \lesssim 100$ (see Appendix 2.9.2).

We multiplied the horseshoe part with $\min(1/s_2, 1)$ to account for the saturation of the torque that originates in the horseshoe region. As shown in previous studies (Masset (2002) and Masset and Casoli (2010)), even when the cooling time is shorter than the u-turn time, and thus it is also much shorter than the libration time, viscosity is the driving factor for the saturation of the horseshoe region. This yields the following type I migration coefficient C_{T1} (in the second term of Equation 2.3):

$$C_{\mathrm{T1}} = C_{\mathrm{Lind}} + \min\left(1/s_2, 1\right)\left(z(s_1) C_{\mathrm{HS,loc}} + \left(1 - z(s_1)\right) C_{\mathrm{HS,adia}}\right). \tag{2.20}$$

This assumes that even when cooling is much faster than the libration time scale the horseshoe drag will saturate without sufficient viscous coupling of the horseshoe region to the rest of the disk. The horseshoe part itself shifts between the adiabatic and the locally isothermal value depending on the ratio s_1 of the cooling time scale to the u-turn time scale (if h is constant also with respect to the libration time scale (Eq. 2.18)).

The reduction of the surface density at the planet's location due to the beginning gap formation for more massive planets will also modify the migration behavior. Crida and Morbidelli (2007) derived a formula to estimate the depth of the gap relative to the unperturbed disk. In their definition, a gap is formed when the surface density is reduced to 10% of the unperturbed value. They defined a factor (their Eq. 12)

$$P_\Sigma = \frac{3h}{4\sqrt[3]{q/3}} + \frac{50\nu}{q a_{\mathrm{p}}^2 \Omega_{\mathrm{p}}} \tag{2.21}$$

as a combination of two criteria (the thermal and the viscous condition) and used this factor to approximate the depth of the gap as

$$f_\Sigma(P_\Sigma) = \begin{cases} \frac{P_\Sigma - 0.541}{4.0} & \text{if } P_\Sigma < 2.4646\,, \\ 1.0 - \exp(\frac{P_\Sigma^{3/4}}{-3.0}) & \text{otherwise}\,. \end{cases} \tag{2.22}$$

We multiplied Σ_{p} in Eq. 2.3 with this factor to reduce the surface density in our torque calculations. This means that the type I migration rate is reduced by a factor of up to 10 at the point of transition to type II migration. This reduced type I migration rate

is still about one order of magnitude higher than the type II migration rate for typical disk conditions (Sect. 2.3.5), which necessitates using a smooth transition function necessary.

Eventually, when the planet mass reaches the gap opening mass $M_{\rm gap}$, that is, the mass at which $f_\Sigma = 0.1$, the torque transitions to type II:

$$C = z\left(\frac{M_{\rm p}}{M_{\rm gap}}\right) C_{\rm T1} + \left(1 - z\left(\frac{M_{\rm p}}{M_{\rm gap}}\right)\right) C_{\rm T2}. \tag{2.23}$$

We used the same functional dependency as in (Eq. 2.19) for a smooth transition from the type I to the type II torque. Here, we set the smoothing parameter $b = 10.0$ (fast transition), because the reduction of the surface density already partly smoothes the transition (see Sect. 2.9.2). The transition factor $s_{\rm typeII}$ is in this case the ratio of the planet mass to the mass at which the planet would open a gap in the disk:

$$s_{\rm typeII} = \frac{M_{\rm p}}{M_{\rm gap}}. \tag{2.24}$$

The factor $C_{\rm T2}$ is the corresponding type II migration coefficient in the same dimensions as $C_{\rm T1}$, given as

$$C_{\rm T2} = \frac{\dot{a}_{\rm p,T2} M_{\rm star} h^2}{2 a_{\rm p}^3 \Sigma_{\rm p} q \Omega_{\rm p}}. \tag{2.25}$$

2.3.5 Comparison with other models

In this section we compare our model with that of Paardekooper et al. (2011) for a specific choice of parameters. The global consequences in a full planetary population are shown in Section 2.5.1. Here, we use a simple, nonevolving 1D-disk and compare the torques predicted by the two models in such a disk with results from the 3D radiation-hydrodynamic simulations of Kley et al. (2009) and Bitsch and Kley (2011).

Paardekooper et al. (2011) developed a more complex migration model trying to use first principles to derive in particular the transition functions compared with our model described in Sect. 2.3. They derived their torques by calculating the effect of viscosity and thermal diffusion onto the horseshoe region itself. From this they found transition functions between different parts of the corotation torque, using thermal diffusion time scales and viscous time scales as transition criteria between barotropic and entropy-related parts of the horseshoe drag and the linear corotation torque and also the saturation of both. On the other hand, we altered our torque according to the ratio of these time scales using an arbitrary transition. They called their ratio of these time scales p_ν and p_χ with p_ν^2, the ratio scaling the saturation due to viscosity, being equal to our s_2 ratio if $f_{\rm visc} = 0.75$. For p_χ one can show that

$$\frac{\pi}{3} p_\chi^2 = \frac{1.16^2 8}{9} \frac{h}{\sqrt{\gamma}} s_1. \tag{2.26}$$

The numerical factors in front of both sides of the equation are almost equal 1. The transition functions in Paardekooper et al. (2011) and our work are different. Therefore

we considered the turnover points to compare the transitional behavior. In our model it occurs when $s_1 = 1$. For typical values of h and γ this leads to a value of $p_\chi \approx 0.2$. While not as easy to characterize due to the multiplication of several factors (see their Eqs. 23, 30, 31, and 53), this is in the range where the transition in the entropy torques occurs also in the model of Paardekooper et al. (2011). The main difference in the description is the separate treatment of the "entropy" and "barotropic" parts in Paardekooper et al. (2011) with three slightly different transition functions between different parts of the torque. We only used one transition function between the locally isothermal and adiabatic regime to attribute the dependence of the torque on cooling processes. Finally, they used only one free parameter, the smoothing factor for the planetary potential, which we set to 0.4 in our comparison here. They also stated that their model is mostly applicable to planets with a mass of a few Earth masses, while our model is intended to be applicable to a wider mass range.

To quantify the impact of the differences, we next compared the torques predicted by our simple model with those in 3D radiation hydrodynamic simulations, and also with the results found with the Paardekooper model. As will become clear, one finds that despite the simplifications in our model, we can fit the numerical results relatively well.

The 1D disk for the comparison was set up to be as similar as possible to the disk from the 3D simulations of Kley et al. (2009) and Bitsch and Kley (2011). The surface density Σ is a power-law in semimajor axis with a fixed slope of -0.5, and the temperature T is a power-law in semimajor axis of -1.5 inward of 2.5 $a_{\rm Jup}$, where $a_{\rm Jup}$ is the semimajor axis of Jupiter. Farther out, when the temperature almost reaches 10 K, its power-law exponent $\beta_{\rm T}$ increases and approaches 0. We used the same EOS (Saumon et al., 1995) and opacity tables (Bell and Lin, 1994) as in our full model. The viscosity was set to the same value as in Kley et al. (2009). All other disk parameters, such as disk height H or density ρ, were calculated from Σ and T. In this disk we then calculated the specific torques on planets of either different mass or different semimajor axes. With $\beta_\Sigma = -0.5$ and $\beta_{\rm T} = -1.5$ there will be no type II torque since there is no radial gas flow in this disk. We stress that our disk model for the planet population synthesis calculations is in contrast a time-evolving 1+1D α model and is summarized in Sect. 2.4.1.

In Fig. 2.2 we plot torques from our model as a function of planetary mass and compare them with simulations from Kley et al. (2009), while in Figure 2.3, we compare our model with Bitsch and Kley (2011), where torques at different semimajor axes for a 20 $M_\oplus$ planet were calculated. In both figures we also show the torque as predicted from the model of Paardekooper et al. (2011) (for their suggested optimal free parameter $b = 0.4$).

We plot the migration rates for our model with and without the reduction of the surface density due to gap formation (solid and dashed lines respectively). This reduction was not only applied to our own model but also to the Paardekooper et al. (2011) prediction. For the dependency of planet masses (Fig. 2.2), the curves with the gap reduction remain closer to the data obtained by Kley et al. (2009). At around 200 $M_\oplus$ when the transition to type II occurs, this factor causes a 10 times lower type I torque than without the reduction. Therefore with the zero type II torque in this disk-setup,

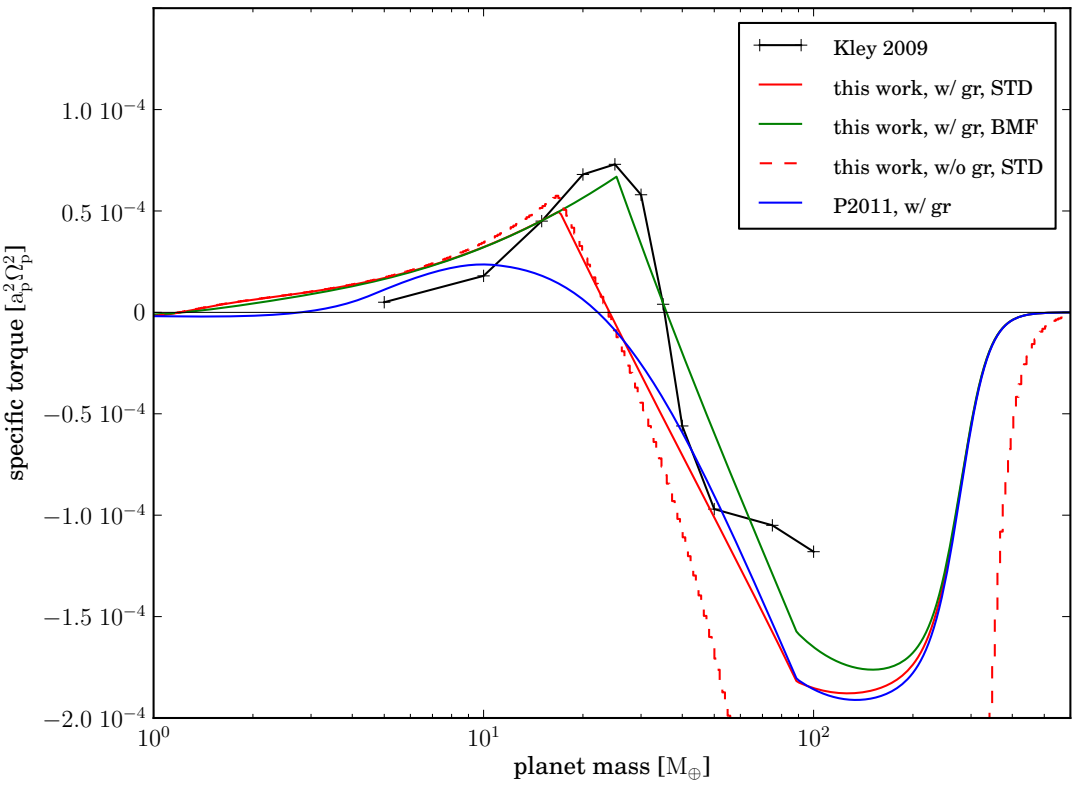

Figure 2.2 Specific torque for different planet masses in the range from 1 to 600 $M_\oplus$ at 5.2 AU. The red solid line shows torques obtained with our nominal case ($f_{\rm visc} = 1.0$), the green line is from the BMF model ($f_{\rm visc} = 0.55$). The red dashed line does not include the reduction of the surface density due to gap formation (gr), otherwise it is identical to the nominal model. The black line with crosses shows torques from the 3D-radiative hydrodynamic simulations of Kley et al. (2009). A blue line shows torques obtained with the model of Paardekooper et al. (2011). The solid green line is our model of choice for the population synthesis models because it fits the results of full 3D simulations best.

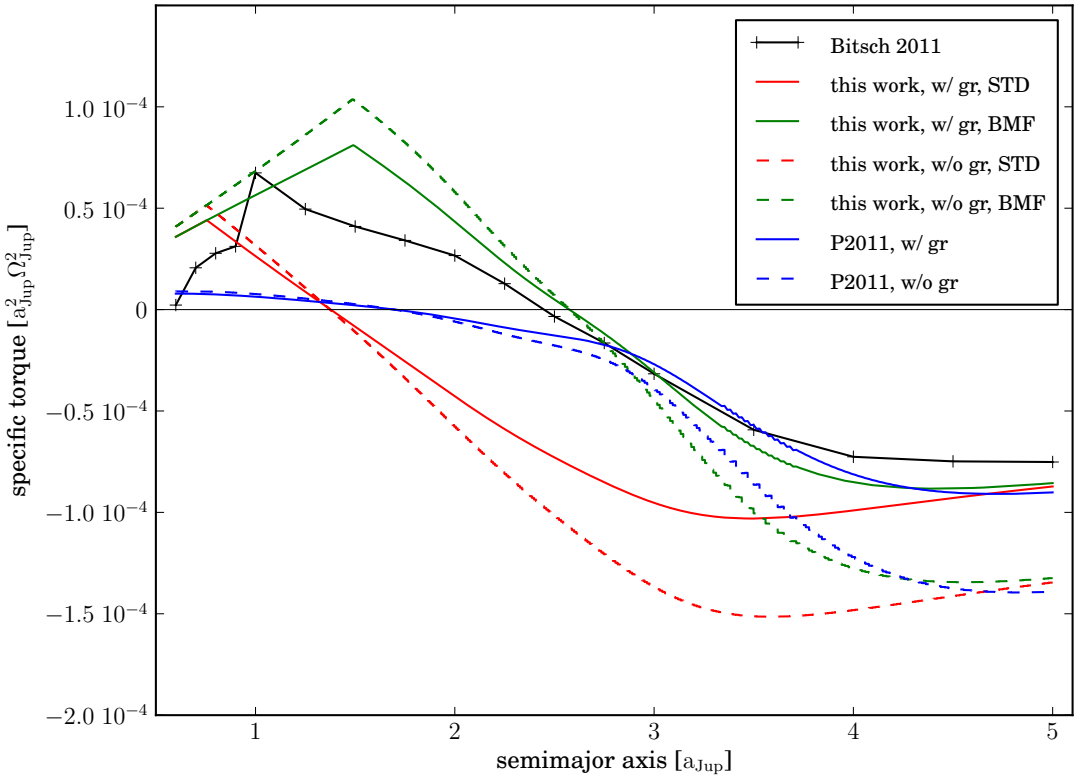

Figure 2.3 Specific torque for different semimajor axes in units of the semimajor axis of Jupiter $a_{\rm Jup}$ for a 20 Earth mass planet. The red lines show torques obtained with our STD model ($f_{\rm visc} = 1.0$), the green lines with the BMF model ($f_{\rm visc} = 0.55$). The solid (dashed) lines do (not) include the reduction of the surface density due to gap formation (gr). The line with black crosses shows torques found in the 3D-radiative hydrodynamic simulations of Bitsch and Kley (2011). The blue line shows torques obtained with the model of Paardekooper et al. (2011). The solid green line is our model of choice for the population synthesis models because it fits the results of full 3D simulations best.

the overall torque is also 10 times smaller. The red lines correspond to our model described above (with $f_{\rm visc} = 1$: hereafter the STD "standard"-model), while the green lines are our model with $f_{\rm visc} = 0.55$ (hereafter the BMF "best mass fit"-model). The latter value for $f_{\rm visc}$ was chosen to increase the saturation mass in a way so that the mass of zero torque in our own semi-analytical model agrees with the data of Kley et al. (2009). The associated reduction of transition parameter s_2 could be interpreted as a more efficient viscous injection of angular momentum into the horseshoe region from the rest of the disk than in the STD-model. Only a factor ~ 2 is needed to bring our model in agreement with the hydrodynamic simulations, meaning that the simple estimate of the transition using the characteristic time scales leads to relatively accurate results. Setting $f_{\rm visc} = 0.55$ also increases the maximum specific torque, which follows the data from Kley et al. (2009) more closely than our model with $f_{\rm visc} = 1$, or the model of Paardekooper et al. (2011), at masses larger than 15 $M_\oplus$.

In Figure 2.3 we compare torques on a planet of a fixed mass (20 $M_\oplus$) as a function of semimajor axis. Here we see as well that the BMF-model provides the best agreement with the data of Bitsch and Kley (2011). The semimajor axis at which the torque vanishes is with 2.7 $a_{\rm Jup}$ relatively close to the 2.5 $a_{\rm Jup}$ found in the hydrodynamical simulations. The model of Paardekooper et al. (2011) places the position of zero torque at 1.8 $a_{\rm Jup}$, while in the STD-model it occurs at 1.4 $a_{\rm Jup}$. Thus, for planets closer than 2.5 $a_{\rm Jup}$ the BMF-model seems to be the best representation of both sets of numerical simulations.

At larger distance from the star the BMF-model and Paardekooper et al. (2011) again yield similar results and compare relatively well to the data. All curves also indicate that including the reduction of the surface density in Eq. 2.3 due to gap formation leads to a better agreement with the torques found in the hydrodynamic simulations, especially in the outer parts of the disk. In summary, we see that by setting $f_{\rm visc} = 0.55$, the model agrees fairly well with the data provided from 3D simulations.

Some diskrepancy exists for the innermost point considered in the hydrodynamic simulation. It is most likely caused by effects of the change of the opacity due to ice evaporation, which is handled in a different way in our model vs. the 3D full models, so that the gradient of temperature and surface density differ.

Note that this comparison in principle only applies for a fixed value of the Prandtl number. The latter depends on γ and the optical depth τ (Paardekooper et al. (2011)), which varies, for instance with the distance from the star or temperature. In the limit of high optical depth, the Prandtl number approaches $Pr = \frac{9}{4}\gamma(\gamma - 1)$.

Nevertheless, we conclude that our BMF-model can quite adequately reproduce the current understanding of planet migration based on (semi-) analytical models for the modeling purpose of planetary populations.

2.3.6 Model versions

In the last section, we have calibrated our semi-analytical model with the results of a specific set of radiation-hydrodynamic simulations. With these results, we define three versions of the model that are used below to study the (global) effects of these different variants of our migration model:

- **STD model** In the standard version we simply set $f_{\rm visc} = 1.0$ so that the plain time scales as defined in Section 2.3.3 are employed to calculate the point of saturation.

- **BMF model** In the best mass fit version we multiply s_2 by 0.55 ($f_{\rm visc} = 0.55$). This model compares best with the 3D migration simulations as shown above.

- **RED model** In the reduced version we reduce s_2 by multiplying it with 0.125 ($f_{\rm visc} = 0.125$). This results in a four times higher saturation mass than for the STD case. We use this even larger reduction to study the effect of different reduction factors.

2.4 Formation models and migration tracks

In addition to the comparison shown above for the migration rates alone, we are interested in the global effects of the new migration model onto a planet population compared with our older isothermal migration model. The planet formation model used for this is based on the paradigm of core accretion (Perri and Cameron, 1974; Mizuno et al., 1978; Pollack et al., 1996; Alibert et al., 2005). The model is described in detail in Alibert et al. (2005) with later modifications shown in Mordasini et al. (2009a), Mordasini et al. (2010, 2012a,b), and Fouchet et al. (2012). It consists of different computational modules, namely the planet accretion module, the disk module, and the migration module. The migration module is described above and was used in recently published work of Fortier et al. (2013), Mordasini et al. (2012a), and Mordasini et al. (2012b). In the following sections we give a short overview of the disk and accretion modules. Then we present calculations of a few specific planets, show the associated formation tracks and the important features found in them. Finally, we present results from planet population synthesis calculations. Since we concentrate in this paper on the direct effects of the new migration model, we present here only simulations with just one embryo per protoplanetary disk. The interplay of migration and multiple concurrently forming planets (Alibert et al., 2013) will be addressed in future work.

2.4.1 Disk model

As a model for the protoplanetary disk, we used a 1+1D model as in Papaloizou and Terquem (1999) or Bell and Lin (1994), and present only a short summery here. The protoplanetary disk is described as a viscously evolving α disk, where α is assumed to be constant throughout the disk. The viscosity is given as $\nu = \alpha H c_\mathrm{s}$ with H the disk scale height and c_s the sound speed (Shakura and Sunyaev, 1973). Irradiation effects from the host star can be included in the calculations of the vertical structure (Fouchet et al., 2012). For the evolution of the gas surface density Σ over time t and distance a from the star we solved the standard viscous evolution equation from Lynden-Bell and Pringle (1974). For most of our simulations in this paper we neglected stellar irradiation and used only viscous heating if not otherwise mentioned:

$$\frac{d\Sigma}{dt} = \frac{3}{a}\frac{\partial}{\partial a}\left[a^{1/2}\frac{\partial}{\partial a}\left(\nu\Sigma a^{1/2}\right)\right] + \dot{\Sigma}_\mathrm{w}(a). \tag{2.27}$$

As a sink term we included the photoevaporation rate $\dot{\Sigma}_\mathrm{w}(a)$ as given in Mordasini et al. (2009a). Together with α and the initial disk mass it determines the disk lifetime. At the start, the solid surface density of the planetesimals is equal to the gas density times the dust-to-gas ratio $f_\mathrm{D/G}$. It is further reduced inside of the iceline at a temperature $T = 170\,\mathrm{K}$ by a factor of 4. Other than by accretion onto and ejection by the planet, we did not evolve the solid surface density.

2.4.2 Model of accretion and internal structure

We simulated the growth of one planet per disk. For this, we inserted a $0.6\,M_\oplus$ seed embryo at a random position in the disk. The core has a constant density of $3.2\,g/cm^2$ and contains all the heavy matter the planet accretes, that is, we assumed that all planetesimals sink to the core (Pollack et al., 1996). The seed will initially start to accrete mostly planetesimals, which leads to a growth of the core. The amount of energy released from the infalling planetesimals is high at this point and the core mass is low, therefore initially only small amounts of gas are bound. As the core grows, it binds an increasingly massive envelope. The accretion rate of gas is found by solving the standard equations of the structure of planet interiors, but with the simplification that the luminosity is constant throughout the envelope.

In the original model of Mordasini et al. (2009a), the luminosity of the planet is due to the accretion of planetesimals alone. This is usually the dominant source of luminosity at smaller masses (Pollack et al., 1996). Here, we adopted a simplified version of the model described in Mordasini et al. (2012b) to take also into account the luminosity generated by the accretion of gas. In the original model it was sufficient to consider only the luminosity due to the planetesimals, because the migration was always directed inward. This means that the cores always migrate into regions with a high solid surface density. With the new migration model, this is no longer the case: because the positive torques act at certain masses (see Section 2.3.5), it is possible that a core migrates through parts of the disk with a very low solid surface density content. There the luminosity of gas accretion becomes important.

2.4.3 Convergence zones

These positive torques lead to regions in a disk where a planet within the adiabatic migration regime migrates outward instead of inward (Lyra et al., 2010; Mordasini et al., 2011). Figure 2.4 shows the values of C_{adia} (which represents the strength of the migration in the adiabatic regime, see Eq. 2.6) at time equal 0.02, 0.1 and 0.5 Myr in a nonirradiated evolving α-disk with $\Sigma_0 = 420\ g/cm^2$ and $\dot{M}_w = 6.7 \times 10^{-9}\ M_\odot/yr$. These parameters results in a lifetime of the disk of 2.8 Myr.

In Figure 2.4 one can see two regions of outward migration, i.e., with positive values of C_{adia}, from 0.46 AU to 2.6 AU and farther out from 3.6 AU to 11.5 AU at 0.02 Myr (red curve). At later times these regions are closer to the star as the disk evolves. To further illustrate the time evolution of the regions in Figure 2.5 we show the direction of migration as a function of time for this disk. Blue indicates regions of inward migration while green shows outward migration. One can see that these regions slowly move inward as the disk evolves. This occurs on the viscous time scale of the disk (Lyra et al., 2010). Owing to the existence of the outward and inward regimes, there are special locations in the disk. For example, at an age of 0.5 Myr, the migration changes from outward to inward at 10 AU (and at about 1.2 AU) when moving to a larger distance (i.e., these are points of zero torque where the derivative of the torque with distance is additionally negative). Such a point is called a convergence zone (CZ). It is called this because planets in its vicinity converge on this zone from both inside

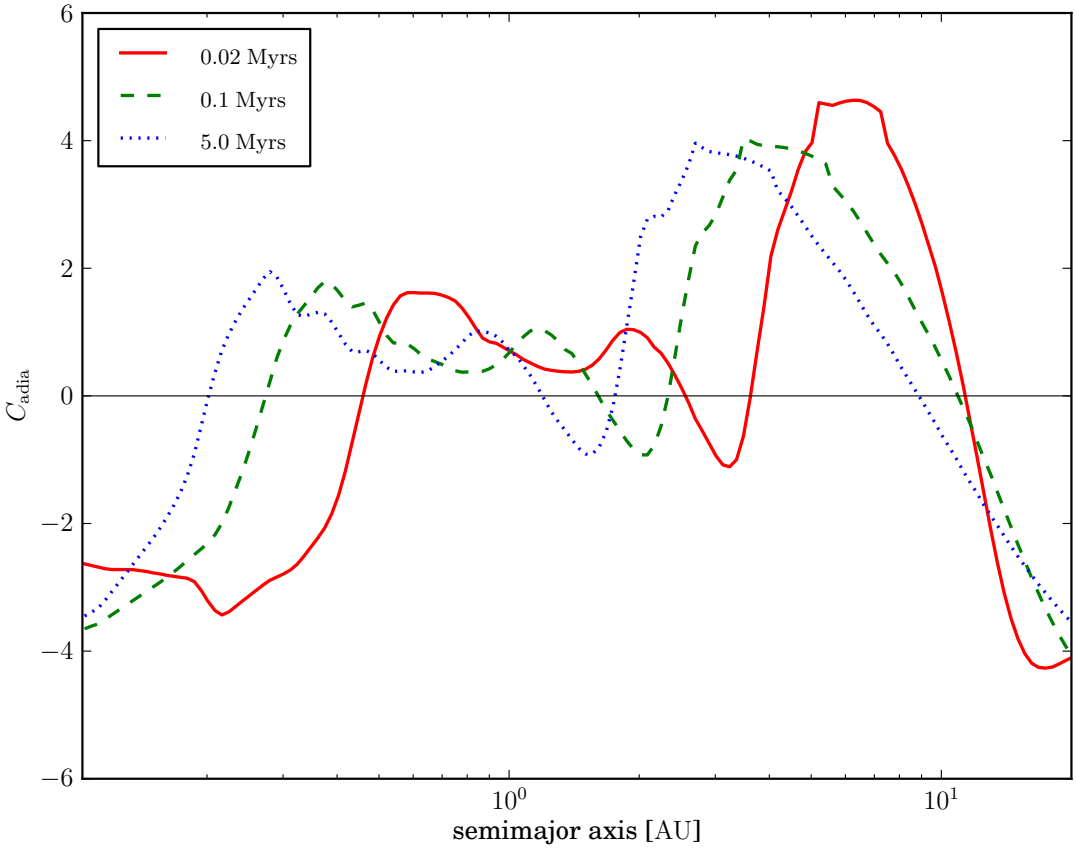

Figure 2.4 Strength of adiabatic migration coefficient $C_{\rm adia}$, plotted as a function of semimajor axis at times equal 0.02 , 0.1 and 0.5 Myr in a nonirradiated, evolving α-disk. Positive values of $C_{\rm adia}$ drive outward migration.

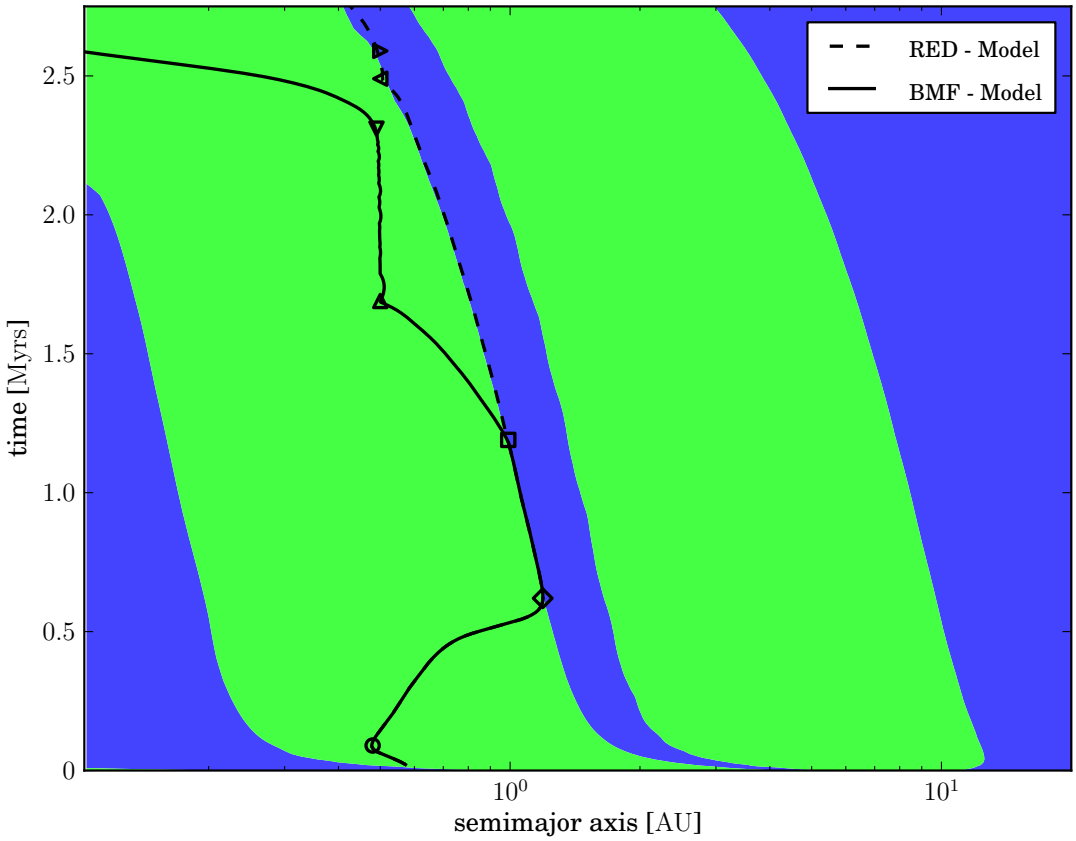

Figure 2.5 Direction of migration in the adiabatic migration regime for a nonirradiated evolving α-disk. Blue indicates regions of inward migration while green shows outward migration. The black lines are the migration tracks of an evolving protoplanet set into the disk at 2000 yr. The track shown with the solid line uses the BMF migration model while the dashed line is calculated with the RED model (see Sect. 2.4.4). The symbols mark important points in the evolution and are discussed in the text.

and outside (see Lyra et al., 2010). The domain in orbital distances from which planets migrate to the convergence zone is the associated convergence region. At 0.5 Myr, the inner convergence region extends from 0.2 to 1.8 AU for example. Similar results for two convergence zones for various disk models were also recently presented by Kretke and Lin (2012) and Yamada and Inaba (2012). After reaching the convergence zone, a planet remains slightly outward, but close to it, so that the net torque pushes the planet inward at the same migration rate as the zone itself.

Once captured in a convergence zone, the planet migrates on a time scale that is at least an order of magnitude longer than typical type I migration time scales. For example, while captured in the inner convergence zone, the planet discussed below has an equivalent migration coefficient C (Eq. 2.3) of 0.034 while C is during normal type I migration on the order of 1 as shown for instance in Fig. 2.4 or Paardekooper et al. (2010).

However, for some conditions, a low-mass planet cannot migrate at a sufficiently high rate to remain close to the CZ. Instead, the planet leaves the CZ and falls behind it (the planet still migrates inward, but is overtaken by the CZ). This occurs especially for the inner convergence zone. Typically, after leaving the inner zone, the planet transitions into the outer one, where it is again captured. The reason is that the type I migration rate is proportional to the planet mass. For a sufficiently low mass of the planet, the type I migration time scale thus becomes longer than the viscous time scale of the disk, which sets the speed at which the CZ moves. This characteristically occurs at the end of the disk lifetime, when the gas surface density is low, so that the type I migration time scale becomes even longer.

The position of the inner CZ is close to the distance of the local minimum in the opacity at a temperature of $\approx 200K$ (Lyra et al., 2010), which is the temperature where ice grains are completely molten in the opacity law of Bell and Lin (1994). The change in the slope of the opacity at this point leads to a change in the temperature power-law exponent β_T, which leads to the change of the sign of C_{adia} and therefore to a convergence zone. The reason for the outer CZ is the change of the temperature slope due to the convergence onto the background temperature in the outer part of the disk.

The convergence zones only exist for a certain range of planet masses (Kretke and Lin, 2012). A low-mass planet will migrate in the locally isothermal regime since the thermal processes in the disk are fast enough to regulate the temperature during a u-turn of the gas. On the other hand, when a planets becomes massive enough, the angular momentum flux through the horseshoe region will be too low to support the unsaturated horseshoe drag, so this part of the torque saturates and in general rapid inward migration sets in.

2.4.4 Migration and formation tracks

The new migration model leads to changes in the evolution of a protoplanet that are different from those described in Mordasini et al. (2009a). We discuss the new behavior in this section where we show the migration and formation tracks of a typical protoplanet of our synthesis simulation. Not every evolving protoplanet in our calculations

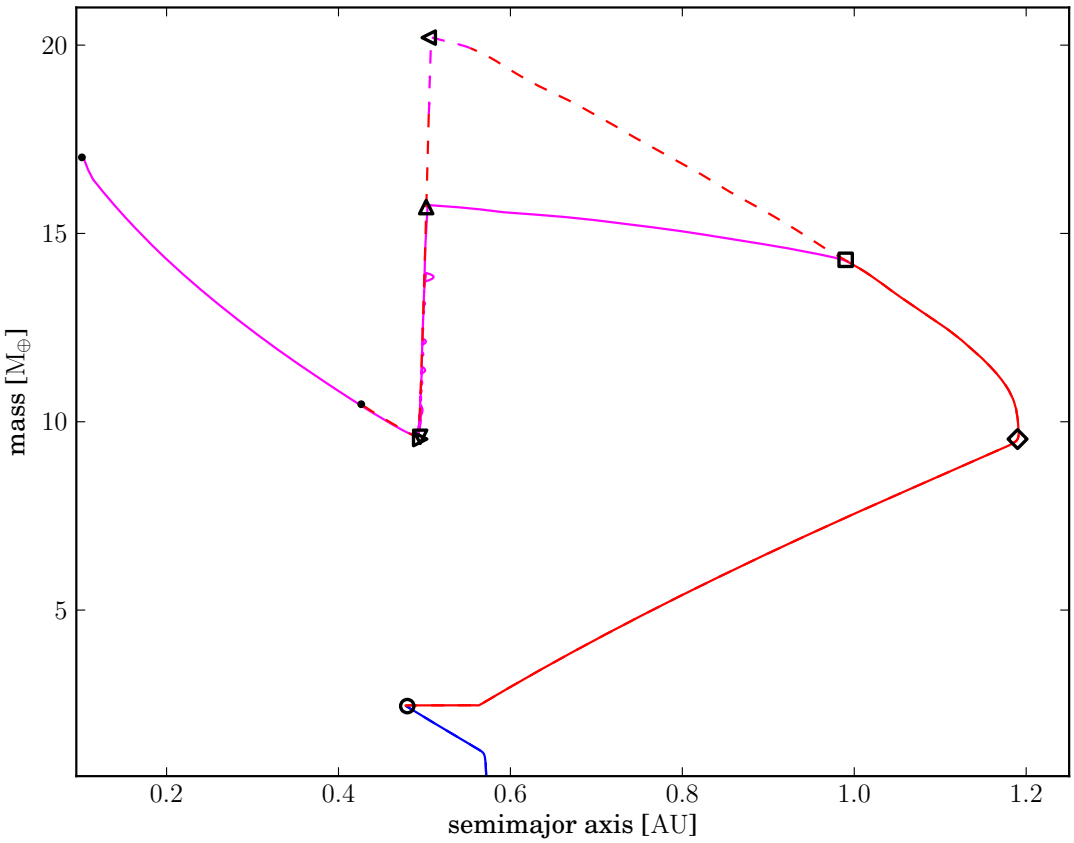

Figure 2.6 Formation tracks, i.e., evolution of the position in the distance-mass plane for a planet in a nonirradiated, evolving α-disk. The track shown as a solid line uses the BMF migration model, while the dashed line uses the RED model. The colors represent the different migration regimes and are also used in this way in subsequent figures. Blue shows unsaturated locally isothermal migration, while red shows unsaturated adiabatic and magenta saturated adiabatic migration. In both cases the planet does not enter the type II or the saturated locally isothermal regime. The symbols mark the same important points in the evolution as in Fig. 2.5 and are discussed in the text. The small filled circles show the final positions of the planets at the end of the simulations.

shows every behavior described below, but most evolutionary tracks of planets feature at least some part of the behavior. The consequences of the new migration model for a whole synthetic population are studied after this.

Further to what was discussed before, Figure 2.5 also shows two tracks of an evolving protoplanet starting at 0.57 AU at 2000 yr after the start of disk evolution. Figure 2.6 shows the corresponding formation tracks of this protoplanet in the semimajor axis mass plane. In both diagrams, the simulation represented by the solid line uses the BMF migration model, where $f_{\rm visc} = 0.55$, while the dashed line is used for the RED model with $f_{\rm visc} = 0.125$ (see Sect. 2.3.6), simulating a larger saturation mass. The beginning of the evolution of the protoplanet is the same in both models. It starts to migrate inward in the locally isothermal migration regime (blue part of the track in Figure 2.6) and accretes solids from its surrounding, depleting this part of the disk of planetesimals. When it reaches a mass of approximately 2.5 $M_\oplus$, its horseshoe region is broad enough that cooling cannot keep the gas that is on horseshoe orbits in a locally isothermal state. The planet enters the unsaturated adiabatic regime, shown in red in Figure 2.6, and starts to migrate outward (at the position marked by a circle in the figures). This occurs at 0.1 Myr as seen in the migration track in Figure 2.5. While migrating outward, the planet does not grow at first because there is almost no solid material left because of its previous passage through this part of the disk. The protoplanet is also still too small to accrete significant amounts of gas. After crossing its initial position, growth by accretion of planetesimals sets back in and the planet migrates outward until it enters the convergence zone at 0.6 Myr (diamond symbol). Here the direction of migration again changes to inward as the planet is now bound to the CZ. While the disk evolves, this zone and the captured planet move slowly inward. The planet again moves through a region that is depleted of almost all planetesimals. But, with a 10 $M_\oplus$ core, the planet is now massive enough to bind nebular gas in its envelope. This is especially true when there is not much solid accretion, which means that the core luminosity is low, and therefore the gas accretion rate is high. The planet grows by accreting gas, until at about 1.25 Myr in the BMF model (solid line), it reaches the mass where saturation sets in (square symbol). The positive horseshoe drag is reduced with increasing mass and is not sufficient to counterbalance the negative Lindblad torques. The planets therefore leaves the CZ and rapidly migrates inward (saturated adiabatic migration regime, magenta in Fig. 2.6).

The planet continues to accrete gas until the inner edge of its feeding zone reaches the distance of the previous closest approach to the star (upward-facing triangular symbol). Again in reach of planetesimals, solid accretion restarts and increases the core luminosity. The envelope expands, heated by this process, and because it is still connected to the disk at this time (attached phase, see Mordasini et al., 2012b), the heating leads to the loss of envelope mass and a corresponding reduction of the total planetary mass (see Sect. 2.4.2). This reduces the level of saturation, which in return increases the horseshoe drag, which can again balance the Lindblad torque resulting in an almost complete stop of migration: if the planet were to migrate outward again, solid accretion would stop and rapid gas accretion would start to increase the mass. This would reduce the horseshoe drag and push the planet back inward. In the opposite case of further inward migration, solid accretion would become stronger. This would increase the core luminosity and remove more envelope mass, and the total

mass decreases. This would increase the outward-directed horseshoe drag because of the reduced saturation of the corotation torques. The planet would thus tend to migrate outward. The combination of these two points means that the planet has reached a quasi-stable point due to the interplay of accretion and migration.

With the evolution of the disk, the saturation mass at a given point in the disk decreases over time. Thus the mass where the partly saturated horseshoe drag balances the Lindblad torques is also reduced with time. Because of the interaction of accretion and migration, the planet's mass remains exactly at this zero-torque mass.

The planet is forced to loose more mass and therefore remains at this semimajor axis for a given moment in time, while, as a result, the planet moves in slowly over longer time scales. It just "nibbles" on the edge of the planetesimal disk that was depleted up to this distance, while reducing its mass. The gas envelope mass is decreased until a level is reached that the planet can support with the full solid accretion rate of normal inward migration.

In case of the BMF model, this is a slow process. The protoplanet remains for 0.5 Myr at 0.5 AU while it looses 6 $M_\oplus$ of the envelope it has accreted while moving inward in the CZ and later in the saturated adiabatic migration regime. At this time it has only 0.1 $M_\oplus$ of envelope left. This is the same amount as at the time it became bound to the CZ. The RED model and its increase of the saturation mass leads to a slightly different behavior of the protoplanet. It remains for a longer time in the CZ and can thus accrete gas for a longer time than the BMF model protoplanet. This results in a larger envelope mass when it reaches the distance of the previous closest approach (left-facing triangle). But since in both cases the protoplanet migrated through the same part of the disk, both have the same amount of solids accreted and thus the same core-mass. Therefore, the increase of the solid accretion rate also leads to a mass loss of the envelope in the RED model case. But here, the planet is still in the unsaturated migration regime while loosing most of its envelope mass. Therefore, the mass loss does not lead to a change in the migration rate. The protoplanet is still bound to the CZ and is pushed by it into the remaining planetesimal disk. Therefore, the mass loss occurs much faster here, the planets looses 11 $M_\oplus$ in only 0.1 Myr.

This illustrates the strong inter-dependence of migration and accretion. The solid accretion rate is set by the amount of solids reachable by the planet, and therefore by the migration that brings the protoplanet into new regions of the disk. But this behavior is only true if the availability of planetesimals themselves, and not the collision rate, is the limiting factor for the solid accretion rate $\dot{M}_{\rm core}$. In the planet-envelope structure model used here, the solid accretion rate, the associated core luminosity, and the mass of the core itself define the envelope structure and thus the envelope mass of a planet.

The small loops in the track that occur while the planet in the BMF model looses mass (between the up- and down- facing triangles) are caused by a finite time-step. Some larger loops are visible in the formation tracks in Figure 2.7. We show here the data obtained during the population synthesis calculations discussed in Sect. 2.4.5 and shown in that figure. We also separately simulated the same case with a much shorter time-step and obtained the same results without these small loops.

We did not consider an increase in the random velocities of the planetesimals due to the presence of a planet. They remain small, as reported in Pollack et al. (1996). A more realistic oligarchic growth model as described in Fortier et al. (2007) and Fortier et al. (2013) leads to higher random velocities and thus a smaller focusing factor in the calculation of the solid accretion rate $\dot{M}_{\rm core}$. This would lead to less envelope loss if $\dot{M}_{\rm core}$ remains small enough.

Another point to consider, in addition to the planetesimal accretion rate, is the treatment of the protoplanetary disk in our model. We did not let the disk evolve except for depletion due to accretion onto the protoplanet. Therefore there is a sharp edge into which the planet can migrate. A more realistic treatment (e.g., planetesimal drifting or diffusion, scattering) would lead to a gradual increase of $\dot{M}_{\rm core}$ and thus to a slower loss of the envelope. But we expect the final outcome to be similar, only the track in the a-M plane would be smoother (mass loss setting in earlier and more gradually).

In both cases shown here, the protoplanet starts again to accrete solids and nebula gas and migrates inward after it looses almost all its envelope mass (down- respectively right-facing triangles in Fig. 2.5 and 2.6). In case of the BMF model it migrates in the faster saturated adiabatic migration regime until in reaches 0.1 AU and a final mass of 17 $M_\oplus$ (0.9 $M_\oplus$ in its envelope) and the simulation stops. In the RED model the simulation ends with the disappearance of the disk at 2.8 Myr and the planet migrated to 0.43 AU with a mass of 10.5 $M_\oplus$ (only 0.1 $M_\oplus$ in the envelope).

2.4.5 Reference population synthesis calculation

After studying the single case, we now look at a population synthesis calculation with 10000 different initial conditions that we used as our reference when we investigated the effects of different migration models on a synthetic planet population. The important parameters of the synthesis can be found in Table 2.1. We used the BMF-migration model and an α parameter of 7×10^{-3} for the nonirradiated disk.

Figure 2.7 shows the tracks of 250 cases, the different migration regimes color coded. The meaning of the colors is described in the caption of Fig. 2.7. One can see that most planets start in the locally isothermal migration regime, changing into the unsaturated adiabatic migration regime before the horseshoe drag saturates and they migrate inward. Some are large enough to transition into type II migration while others end up at 0.1 AU. Two groups corresponding to the inner (inside of 1AU) and outer (outside of 1 AU) convergence zone are visible in Fig. 2.7.

When a planet migrates outward through the iceline, the migration rate does not change, but its solid accretion rate does change by a factor of 4, because the increase in the solid surface density. This results in a bend and a much steeper slope in some of the tracks in the outer zone. Horizontal parts in the formation tracks that indicate migration without growth are also lacking in the tracks of the outer planets. In the outer parts, especially outside of the iceline, the amount of solid matter is too large to be completely accreted onto the planet at the given accretion rates $\dot{M}_{\rm core}$. Thus, planets can also collect material on their second pass through a part of a disk and grow.

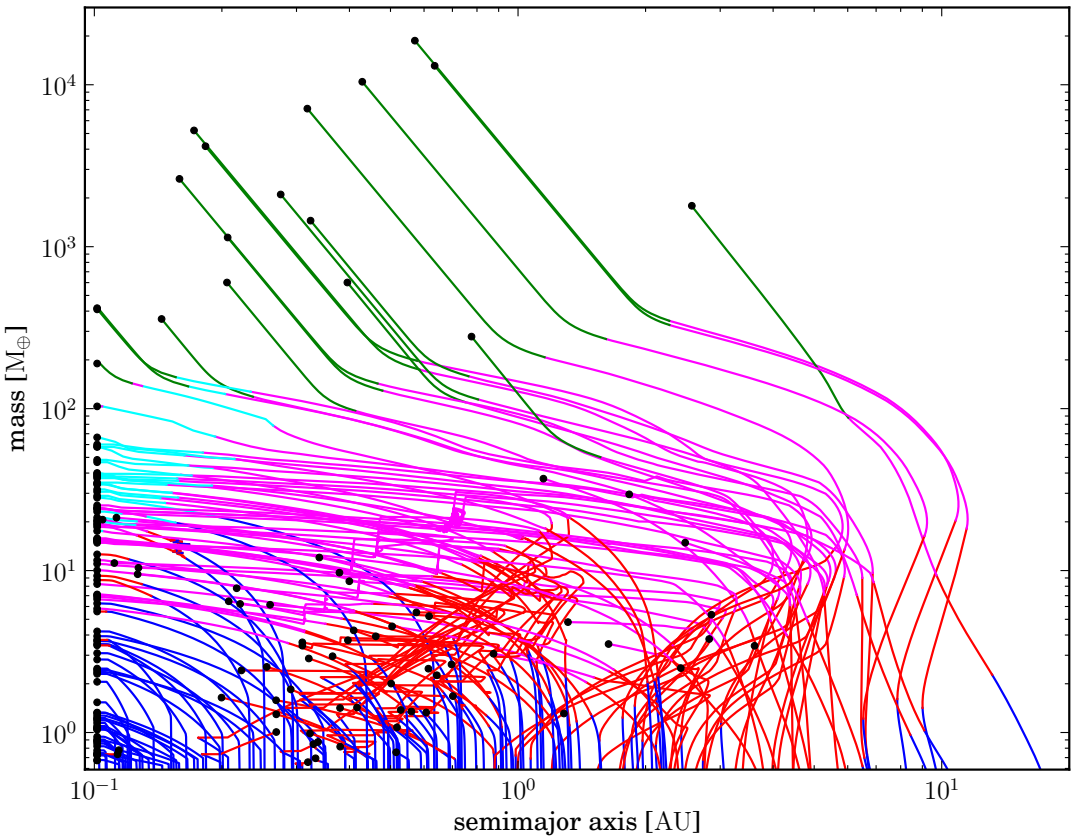

Figure 2.7 Formation tracks, the evolution of the position of the planets in the semi-major axis mass diagram. Color shows the different migration regimes at this point of its formation. Blue shows unsaturated locally isothermal, cyan saturated locally isothermal migration, red shows unsaturated adiabatic and magenta saturated adiabatic migration, finally, green shows type II migration. The filled circles show the final positions of the planets at the end of the simulations.

Quantity	value
Initial disk power-law exponent	-1.5
Disk viscosity parameter α	7×10^{-3}
Inner radius of computational disk	0.1 AU
Outer radius of computational disk	50 AU
Gas surface density at inner radius	continues
Irradiation for disk temperature profile	not included
Iceline	included
Embryo starting mass	0.6 $M_\oplus$
Core density	3.2g/cm^2
Envelope type	primordial H_2/He
dl/dr in the envelope	zero
Grain opacity reduction factor	1.0
Type I migration	BMF-model
Type I migration reduction factor	none
Transition criterion type I to type II	Crida et al. (2007)
Transition exponent	
Type I to type II migration (Eq. 2.23)	10.0
Transition exponent	
Unsat. to saturated migration (Eq. 2.20)	4.0
Cooling reduction factor f_{cool}	1.0
Viscosity reduction factor f_{visc}	0.55
Stellar mass	1 $M_\odot$
Simulation duration	till gas disk vanishes
Number of embryos per disk	1

Table 2.1 Parameters and settings for the reference population synthesis.

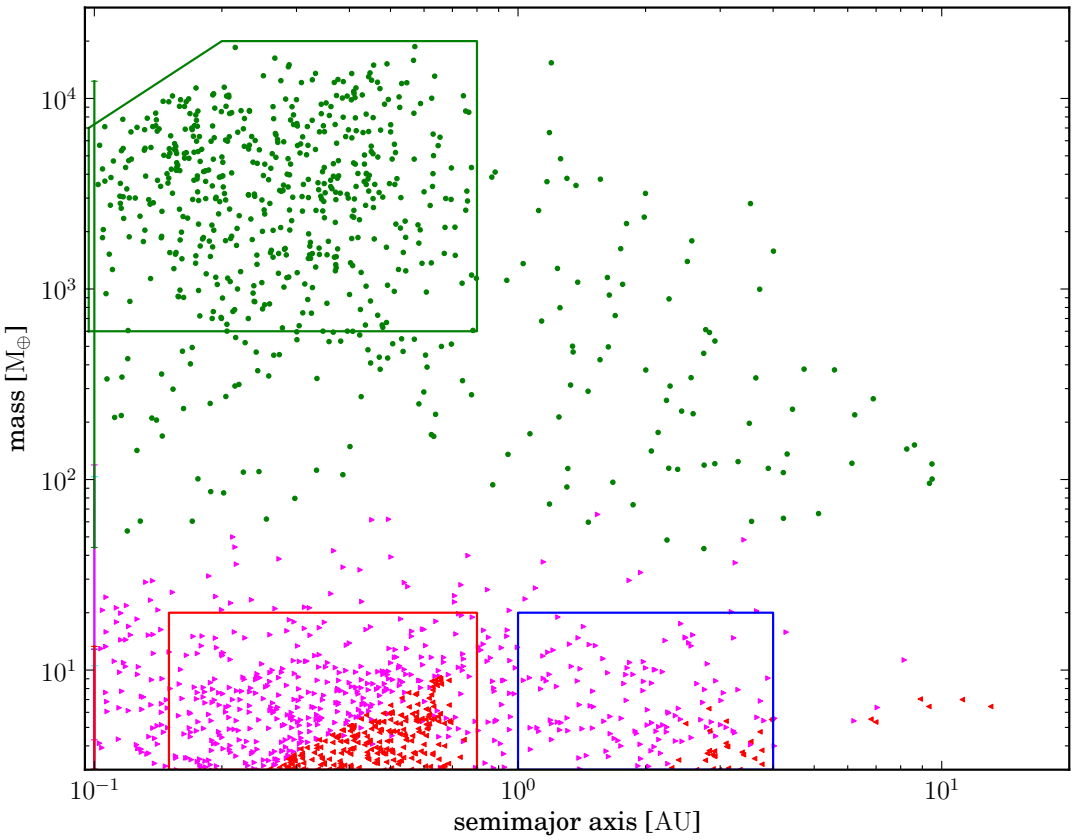

Figure 2.8 Final position of the synthetic planets in the semimajor axis mass diagram. Color shows the different migration regimes a planet is in when the calculation ended. The meaning of the colors is the same as in Fig. 2.7. The bars at 0.1 AU indicate the mass range of the "hot" planets in the different regimes. The boxes indicate clusters of planets described in the text.

The inner and outer CZ are the reason for three groups of planets in the final position a-M diagram. They can be seen in Figure 2.8. A fourth possible cluster is not visible because the BMF-migration model leads to a situation where all those planets migrate inward of 0.1 AU (see Section 2.5.2):

- The first cluster, which is the one with the highest number of planets, lies approximately between 0.15 and 0.8 AU and 1 and 20 $M_\oplus$ (red box in Figure 2.8). It consists of planets captured by the inner convergence zone. Most of the planets are directly attached to the CZ when the disk disappears and the simulation stops. Their mass is too small for a transition into saturated migration and departure of the CZ. A strip of planets extends inward from this cluster. These planets saturated shortly before the disk ended. However, most planets that transition into the saturated migration regime while being in the inner CZ eventually end up at 0.1 AU.

- The second cluster lies farther away from the star (1 AU to 4 AU) but is also in the mass range between 1 and 20 $M_\oplus$ (blue box in Figure 2.8). It consists of planets captured by the outer second CZ. It is less populated because fewer embryos start at the larger distances because the distribution of the starting positions, which are uniform in $\log(a)$. Additionally, the amount of solid material to grow is larger, thus many planets at these distances can reach masses above the saturation mass.

- The third cluster consists of planets that saturated while being in the outer convergence region (green box in Figure 2.8). But they are massive enough and can accrete enough solids on their way in that most of them can transition into type II migration. Here they migrate on the time scale of the disk evolution or slower and can accrete gas until the disk ends. They reach masses between 100 and a few 10000 $M_\oplus$. The planets can reach such high masses because we neglected the effect of gap formation on the gas accretion rate. If the reduction of the gas accretion rate due to gap formation were included, the planet masses would be restricted to lower masses, depending on the disk viscosity and mass (cf. Bodenheimer et al., 2013).

Planets in the inner convergence region will migrate to the inner CZ and thus migrate through a large part of the inner part of the disk. But they remain completely inward of the iceline since the inner convergence region ends there due to opacity transitions. Therefore they are able to accrete most matter in the first few 0.1 AU and thus finally have at least a few Earth masses. In our model we obtain a small planet of several $M_\oplus$ or less only when its starting time is in the last few 0.1 Myr of the disk lifetime. With more than one core per disk one planet alone cannot accrete all the matter in the inner part. The solids will be distributed in many small planets. We therefore overestimate the number of planets between 2 and 30 $M_\oplus$ and underestimate the number of planets smaller than 2 $M_\oplus$.

The synthesis with the new migration model also shows the desert of planets between 30 and 200 $M_\oplus$. This is a feature of the runaway gas accretion that occurrs in the core-accretion model (Pollack et al., 1996). On the other hand, the region of close-in,

low-mass planets, which was empty in Mordasini et al. (2009b), is now well populated with the new nonisothermal migration model.

The spread of the first cluster originates in the spread of the initial conditions of the photoevaporation rate $\dot{\Sigma}_{\rm w}(a)$. In the implementation of our disk module the photoevaporation rate determines the mass of the disk at the end of a simulation and therefore the position of the CZ at the end of a simulation. A single value of $\dot{\Sigma}_{\rm w}(a)$ in all simulations of a synthesis would result in only one position of the CZ and therefore a high concentration of small mass planets on one radius (see also Sect. 2.4.3).

We used some basic statistics, namely the number of "hot" and "cold" planets and the number of massive and small planets (cf. below), to compare synthesis calculations with different migration models. While none of these numbers are compared with those of the observed population of extra-solar planets, the difference between the calculations allows us to see the importance of different parameters or parts of the migration model. Comparison with the observed population will be made in future work when other such as effects like the decrease of the disk mass due to accretion onto the planet or multiple concurrently forming planets (Mordasini et al., 2012b,a; Alibert et al., 2013) are also included. Out of 10000 initial conditions we obtained 6850 planets more massive than our starting mass of 0.6 $\rm M_\oplus$ in the synthesis calculation described above. The remaining 3150 initial conditions have starting times (time when we insert the planet embryo into the disk) longer than the lifetime of the corresponding disk. Out of these 6850 planets 54,4% migrated to 0.1 AU, the inner border of the computational disk, and are called "hot" planets. The other 45,6% ended further out and will be called "cold" planet.

Finally, there are 912 (13.3%) massive planets in total with $M > 100 \rm M_\oplus$. While the majority of all the planets in the synthesis are "hot", the massive planets split into 276 "hot" and 636 "cold" planets. Thus there are more "cold" giant planets than "hot" ones.

2.5 Impact of different migration prescriptions

In this section we compare results from population synthesis calculations where we changed one aspect of the migration model relative to the calculation above (Sect. 2.4.5), but otherwise used the same initial conditions and settings. We therefore refer to the synthesis above as the reference synthesis. We first compare it with migration models described in earlier studies before we change some physics of the model itself.

2.5.1 Earlier prescriptions

We use two earlier prescriptions, the isothermal migration model of Tanaka et al. (2002) used in our earlier work and the migration prescription from Paardekooper et al. (2011).

name	"hot"	"cold"	total massive	"hot" massive	"cold" massive
BMF model, reference synthesis	54.4	45.6	13.3	4.0	9.3
isothermal migration model	79.2	20.8	7.8	2.7	5.1
BMF model, Casoli Lind.	48.8	51.2	15.0	2.9	12.1
RED model	35.4	64.6	19.1	1.4	17.7
STD model	60.5	39.5	11.4	4.5	6.9
Paardekooper, free gamma	55.4	44.6	12.0	4.1	7.9
Paardekooper, gamma = 1.4	59.3	40.7	9.5	4.1	5.4
BMF model, irradiated disks	68.8	31.2	10.1	3.8	6.3

Table 2.2 Statistical results of population synthesis calculations. In the first seven syntheses simulation we consider 6850 planets more massive than 0.6 $M_\oplus$. In the synthesis with the irradiated disk we consider $\approx$ 7700 planets more massive than 0.6 $M_\oplus$. The second column shows the percentage of planets that migrated to 0.1 AU ("hot" planets), while the third column corresponds to "cold" planets ($a > 0.1$AU).We also show the fraction of embryos that grow more massive than 100 $M_\oplus$ (total massive) and how they split into "hot" and "cold" massive planets in columns four to six.

Isothermal migration model of Tanaka et al. 2002

The first comparison was made with calculations preformed with the nonreduced isothermal migration model ($f_1 = 1$) based on the results of Tanaka et al. (2002). While we used the same type I migration model as in Mordasini et al. (2009a), the results here still differ from those published in Mordasini et al. (2009a), since we here use the same transition criteria for the transition from type I into type II migration as in the reference synthesis. This is different from the one in Mordasini et al. (2009a). There only the thermal condition ($H > R_\mathrm{H}$) for the transition into type II was used. This leads to much smaller transition masses than here.

Figure 2.9 shows the final position of the planets in the distance-mass diagram in red, right-facing triangles. Blue, left-facing triangles show the reference synthesis. While the range in mass and distance covered by the planets is the same, there is no clustering caused by the migration into a CZ at small masses (0.6 to 30 $M_\oplus$). The total number of "cold" planets ($a > 0.1\ AU$) is only $\approx$ 45% of the number found in the reference calculation. From the 6850 synthetic planets more massive than 0.6 $M_\oplus$ we find 79.2% "hot" planets with 2.7% "hot" massive planets and only 20.8 % planets outside of 0.1 AU. Of these, 346 are more massive than 100 $M_\oplus$ (5 %). The new nominal nonisothermal migration model in comparison gives twice as many planets that remain outside of 0.1 AU and also almost twice as many massive planets. Some preliminary calculations indicate that this ratio can increase even more with lower values of α. The nominal migration model still leads to a loss of more than half of the planets with more than 0.6 $M_\oplus$ into the inner part of the disk inside of 0.1 AU and therefore potentially into the star. On the other hand, the new model doubles the number of planets outside of 0.1 AU compared with the isothermal migration model without any arbitrary reduction factor.

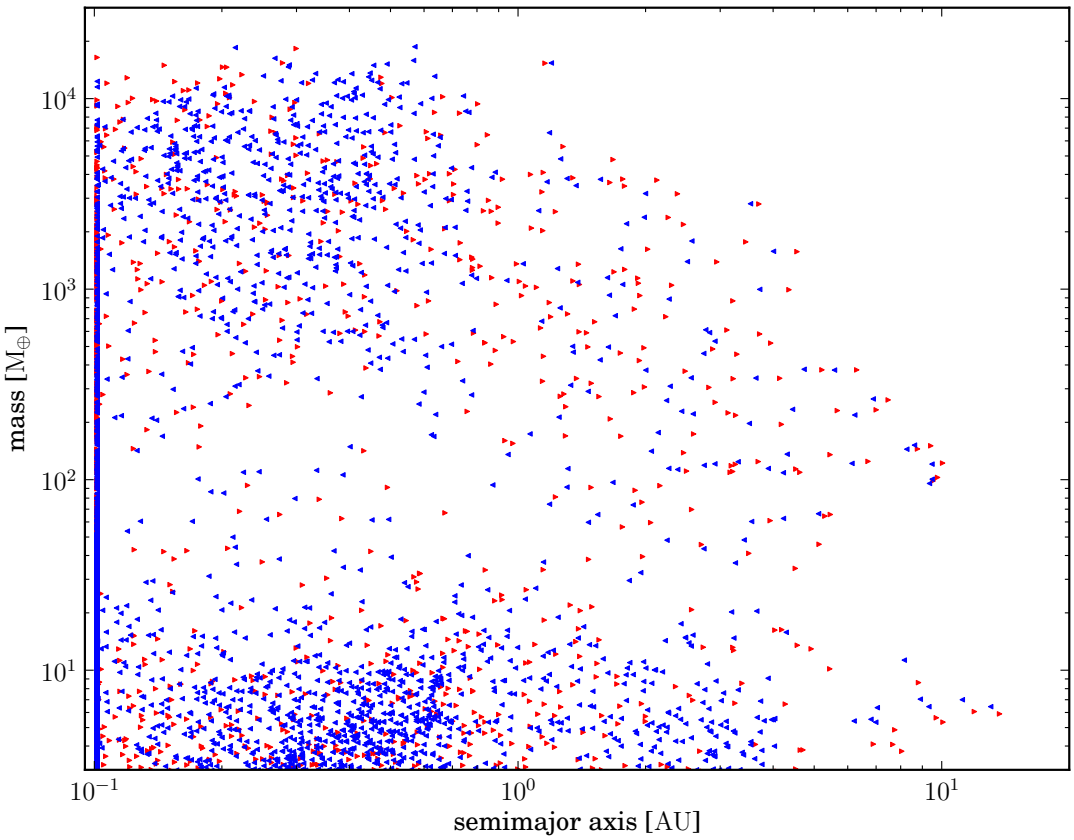

Figure 2.9 Final position of the planets in the distance - mass diagram. Red, right-facing triangles shows the positions obtained with the isothermal migration model. Blue, left-facing triangles correspond to the reference synthesis.

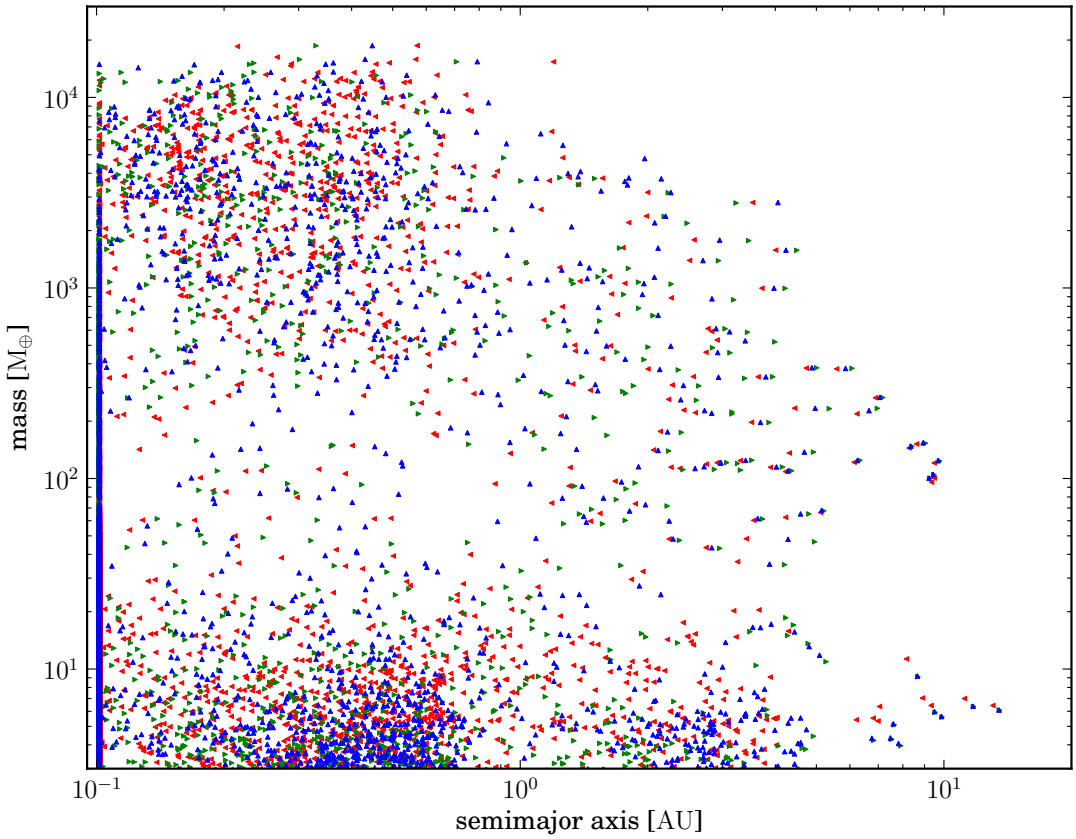

Figure 2.10 Final position of the planets in the distance-mass diagram. Three different syntheses are shown. Blue, up-facing triangles show the reference synthesis. The other two population calculations are made with the migration model of Paardekooper et al. (2011). Red, left-facing triangles represent planets obtained with this model and the adiabatic coefficient γ calculated by our EOS. Green, right-facing triangles show the a-M positions obtained with the Paardekooper et al. 2011 model with a fixed $\gamma = 1.4$.

Paardekooper et al. 2011 migration model

Paardekooper et al. (2011) developed a migration model that is similar to the one described in Section 2.3, but more sophisticated, because it uses thermal-diffusion time scales and viscous time scales as transition criteria between barotropic and entropy-related parts of the horseshoe drag and the saturation of both. The difference between their and our model are discussed in Section 2.3.5, where we compared torque curves from our model with those of this model. We also made two synthesis calculations using this migration model. The final a-M distribution of the two simulations is shown in Figure 2.10. Green dots represent the final positions of the synthetic planets obtained with the Paardekooper et al. (2011) model and a fixed $\gamma = 1.4$. The second calculation is shown in red, here γ was determined with the EOS we usually use (Saumon et al., 1995). The blue symbols show the reference synthesis.

For planet masses larger than three Earth masses there is no real difference be-

tween the three plotted syntheses. The simulation with the free γ produces nearly the same number of "cold" planets, the simulation with the fixed γ slightly $(5-10\%)$ less relative to the nominal BMF model. The situation is slightly different for the number of massive planets with $M_{\rm p} > 100 M_{\oplus}$ outside of 1 AU: the free γ synthesis has only 85% of the number of "cold" massive planets of the BMF-model synthesis and the fixed-gamma simulation about 60% of the nominal model.

The reason for the small differences in the overall amount of "cold" planets but the larger differences for the "cold" massive planets is, as visible in Fig. 2.2 and 2.3, that overall both models produce the same general migration behavior: first planets migrate inward, then outward to a convergence zone, and after saturation inwards again. But the point of crossover from outward to inward migration is closer in and at lower masses for the Paardekooper et al. (2011) model relative to the nominal BMF model. The planets saturate at lower masses and therefore start to rapidly migrate inward earlier in their evolution and fewer planets can reach the type II migration regime and become massive.

Overall, there are no large difference between the different migration models. On the other hand, our simpler BMF model seems to agree better with the torques obtained with the radiative hydrodynamical simulations of Kley et al. (2009) and Bitsch and Kley (2011).

2.5.2 Different input physics

We now study the effect of different Lindblad torques and of different saturation masses onto the synthetic planet population.

Lindblad torques

As stated in Section 2.3.2, there are two different formulas for the Lindblad torques. We changed the Lindblad torque to the one used in Masset and Casoli (2010) for one synthesis. We show the final positions of the planets in the distance-mass diagram in Figure 2.11. The color-coding is the same as before. The resulting Lindblad torque is weaker with the equation of Masset and Casoli (2010), thus the migration in the saturated regime is slower. This results in moving the high-mass, third clusters farther out. In the reference synthesis the outer cluster is located between 0.1 AU and 0.6 AU. Here, it is located between 0.2 AU and 1 AU (red solid box). Inside of 0.2 AU one can see some planets of a fourth cluster. The planets in this inner group originate in part from fast growing planets, that is, those large dust-to-gas-ratios, of the inner convergence zone. The rest are planets from the outer zone, which saturated but grow rapidly enough during their fast inward-migration phase to transition into type II migration. In contrast to the reference synthesis, where all planets of this group migrated to the inner border of the computational domain at 0.1 AU, the planets are now at larger distances and can be seen in the calculation (red dashed box). The third cluster (outside of 1AU) completely consists of planets in the outer convergence zone.

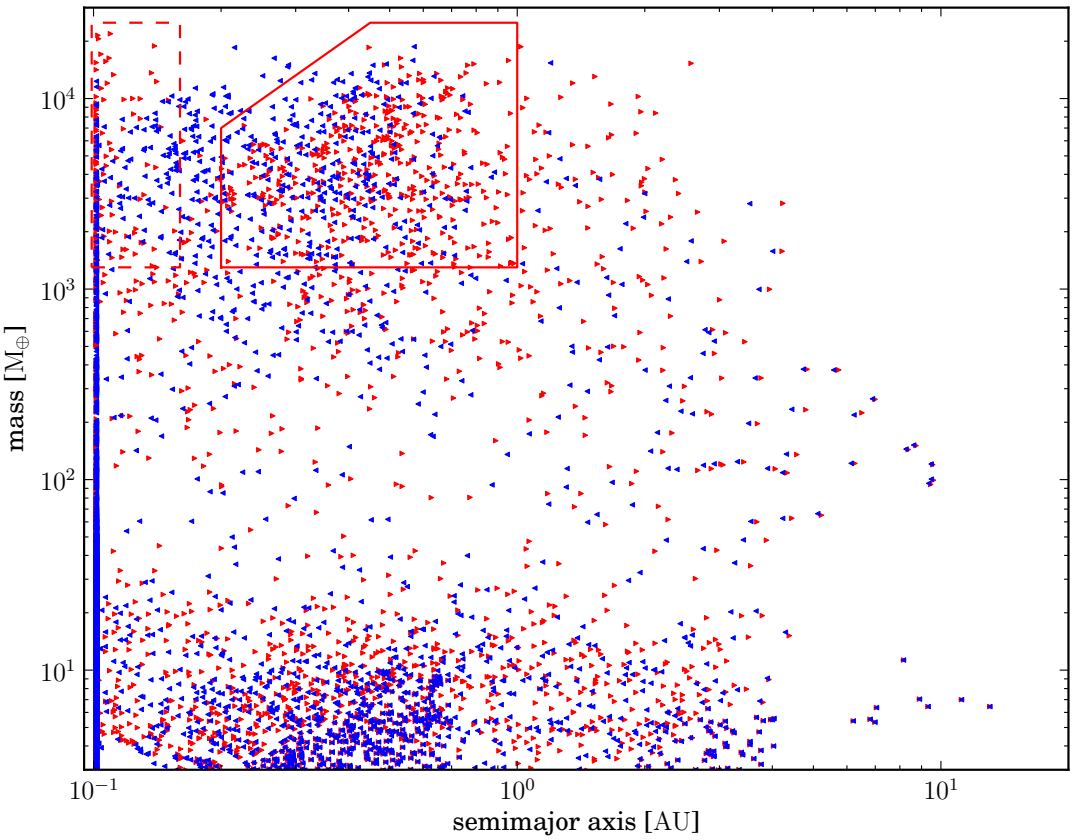

Figure 2.11 Final position of the planets in the semimajor axis mass diagram. Red shows the final position of planets obtained with the BMF model but with a Lindblad torque formula from Masset and Casoli (2010). In blue are depicted the results of the reference synthesis.

The smaller torque also results in a smaller and weaker region of inward migration between the CZ. It is small and weak enough that in some cases, planets can drift from the inner into the outer convergence region, because the migration rate is lower than the movement rate of the CZ due to the evolution of the disk (see Sect. 2.4.3).

For low-mass planets below the saturation mass the differences are smaller between the two syntheses. There are still the two clusters, associated with the two convergence zones.

We can thus conclude that the weaker Lindblad torque results in an shift of the final position of a planet in the distance-mass diagram to the right that is, to larger distances. Because of this we also see more "cold" (increase from 45.6% to 51.2%) and more massive planets relative to the reference synthesis (increase from 9.3% to 12.1%). The calculated migration rate in saturation is only about a factor of 2-3 smaller with the formula of Masset and Casoli (2010) than that of Paardekooper et al. (2010). This seems small compared with the previous reduction of type I migration by a factor of 10-1000. But still, this small change in the description of a part of the torque by a factor of three has observable influence on the distribution of massive planets by up to a factor of 2 in semimajor axis for some cases.

Saturation mass

We furthermore conducted population synthesis calculations with two different values of $f_{\rm visc}$. One with a larger $f_{\rm visc} = 1$ (STD model) and one with a smaller $f_{\rm visc} = 0.125$ (RED model) than the reference synthesis (BMF model, $f_{\rm visc} = 0.55$) (see also 2.3.6). This only affects planets that are massive enough to undergo the transition into a saturated migration regime. An eight times smaller $f_{\rm visc}$ will result in a four times larger saturation mass (Eq. 2.28). Figure 2.12 shows the final positions of the planets in the distance-mass diagram for the two nonnominal calculations and for the reference synthesis. The blue (red) points are the RED (STD) case. For most points of the two clusters of low-mass planets there are only small differences in between these three simulations. They result from the onset of saturation at different masses. For example, some of the planets in these clusters will start to saturate with the STD model while they are still in the unsaturated adiabatic migration regime at the same mass with the RED model and thus migrate faster and also accrete differently because of the different migration rates.

The high-mass clusters are shifted farther out in the synthesis with $f_{\rm visc} = 0.125$ than in the reference calculation. Moreover, the fourth group mentioned in Sect. 2.5.2 is visible for planets obtained from the RED case. In this situation the time planets spend in the saturated migration regime is shorter because of the higher saturation mass, therefore the distance they migrate inward is smaller and the planets end up farther out. This has an effect on the content of heavy elements in the planet. Less migration means that the planet can reach less amount of planetesimals in our disk. The difference is the amount of solids in the annulus of the planetesimal disk that is not visited by the planet with the larger saturation mass. But the difference in the final mass for most massive planets (> 1000 $M_\oplus$) is small, lower than 1%. The reason is that they grow the most while they are in type II migration and the runaway accretion

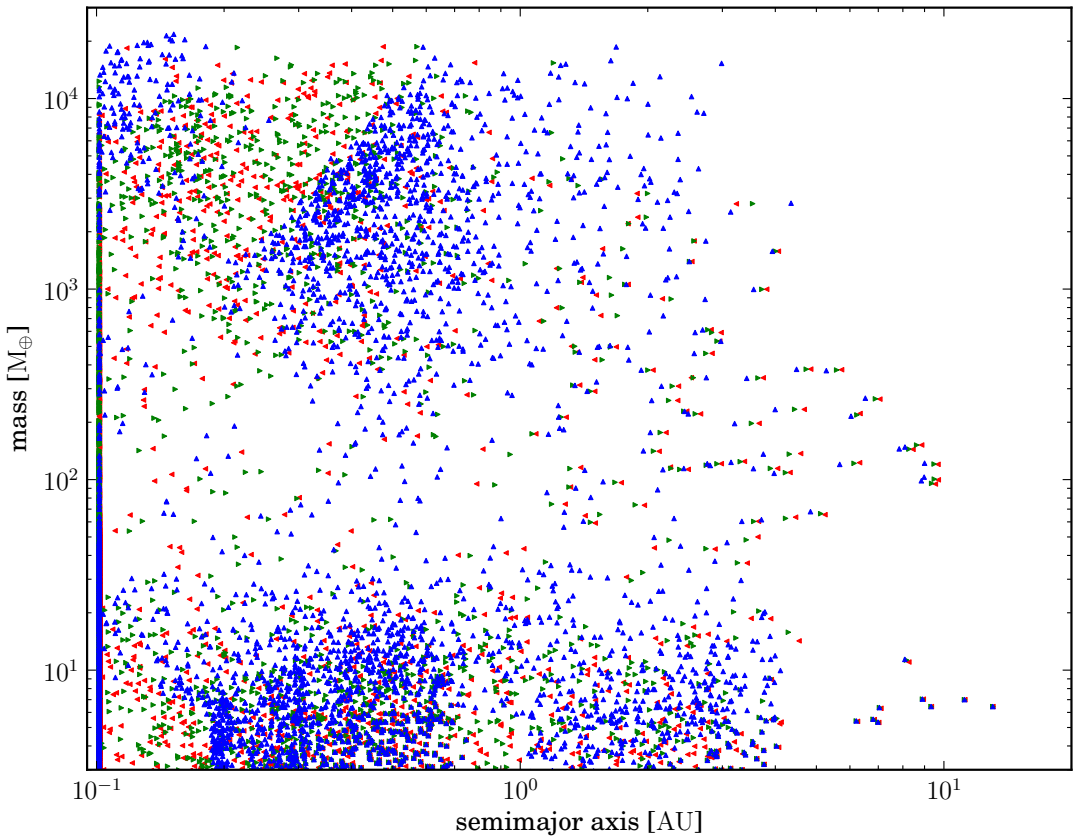

Figure 2.12 Final position of the planets in the semimajor axis mass diagram. Shown are three different synthesis calculations with different values of $f_{\rm visc}$ and therefore three different saturation mass levels. Red shows the calculation with the largest $f_{\rm visc}$, the STD case. In green is shown the BMF case, and in blue the RED case with the smallest $f_{\rm visc}$.

phase. In this phase the accretion is dominated by gas accretion. Here the growth is set by the remaining disk lifetime, and this is almost the same for the different cases.

Note that we made one simplifying assumption: we included the eccentric instability (Kley and Dirksen, 2006). Therefore gap formation does not lead to a reduction of the planetary gas accretion rate. If this effect were not included, the maximal planet masses would be on the order of 10 Jovian masses (Lubow et al., 1999; Armitage, 2007).

Planets beyond 2 AU and between 60 and 400 $M_\oplus$ are closer to the star with a higher saturation mass level than the planets mentioned above. The disk temperature is lower in the outer parts and the slope of the temperature profile begins to become flatter ($\beta_T \to 0$) as the temperature approaches the assumed background temperature of 10 K. This change in the slope leads to a strong change in the horseshoe drag at a radius around 10 AU for early disk times and farther in at later times. It dictates the position of the outer convergence zone (Kretke and Lin, 2012). The change of the slope causes the horseshoe drag itself to become negative not far outside of the outer CZ and pushes the planet inward, as does the Lindblad torque. This means that an increase in the saturation mass will result in faster overall inward migration for the planets that start outside the outer CZ and are saturated in this part of the disk.

When comparing the numbers of "cold" planets in the STD and the RED case we see that the increase of the saturation mass by a factor of 4 results in 64% more "cold" planets and also 156% more "cold" massive planets. The number of "hot" massive planets is reduced from 7.5% to 1.4% as the slower overall migration shifts the clusters outward. Even if we cannot directly compare our results with observations, as a reference, Mayor et al. (2011) stated an observational value of $\approx 1\%$.

2.6 Irradiated vs nonirradiated disks

We recently included irradiation of the host star into the disk model assuming an equilibrium flaring angle (Fouchet et al., 2012). In all calculations presented above, viscous heating only determined the thermal structure of the disk. This is sufficient in the inner parts of the disk at the beginning of the simulations, but leads to too low temperatures in the outer parts of the disk and in the later phases of the disk evolution, when the rate of gas flow through the disk becomes low and the irradiation is dominant. This effect leads to a different temperature gradient, which is important for the strength of the torques (Lyra et al., 2010). The increased heating in the outer parts makes the temperature profile less steep throughout the disk. The temperature is still around 20 K at 50 AU and decreases with distance, while in the nonirradiated case the temperature dropped to the background temperature of 10 K at $20 - 30$ AU and became nearly constant. The temperature structure in the whole disk is set only by the irradiation when the disk is nearly gone and viscous heating is unimportant for the temperature structure of the entire disk. The different profile also affects the shape of the convergence regions. The parts of inward migration in the disk become smaller with time and vanish after a few million years, but still before the disk dissolves (Kretke and Lin, 2012). This affects first the outer and then the inner CZ. Thus, the CZ is no longer a stopping point for type I migration throughout the complete life-

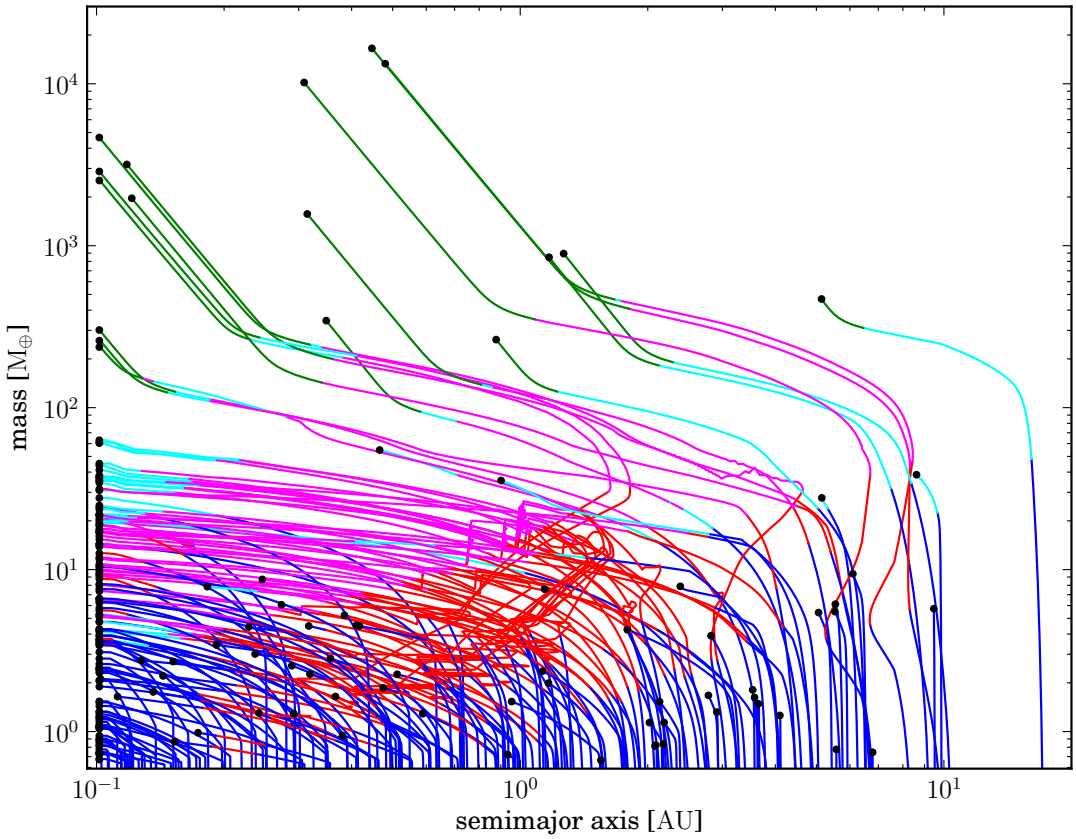

Figure 2.13 Formation tracks for 250 planets of a synthesis with an irradiated disk model. The meaning of the colors is the same as in Fig. 2.7.

time of a disk. Therefore the confinement of planets in a small radius (see Appendix 2.9.1) even when only one value of the photoevaporation rate is used is not the case for irradiated disks.

Figure 2.13 shows the formation tracks of 250 initial conditions and Figure 2.14 shows the final positions of the planets in the distance-mass diagram. In both figures color shows the different migration regimes a planet is in in the same ways as in Figure 2.7. The different symbols in Figure 2.14 indicate if a planet migrated in adiabatic regime during its evolution (empty triangles or circle) or not (filled triangles or circle). The new temperature structure and increase in temperature results in a switch into the adiabatic migration regime at a higher mass than in the nonirradiated disk calculations. Moreovre, as seen in these figures, almost all small planets end in a locally isothermal migration regime even when they went into the adiabatic regime for some part of their evolution (as shown by the red part of the tracks in Figure 2.13) and the unfilled cyan triangles in Fig. 2.14, they end in a locally isothermal regime again when the disk is almost gone. The higher temperature than in the one in nonirradiated disks, especially at the end when almost all gas is gone and only minor viscous heating occurs, leads to a shorter cooling time and therefore to the transition from adiabatic migration into locally isothermal migration.

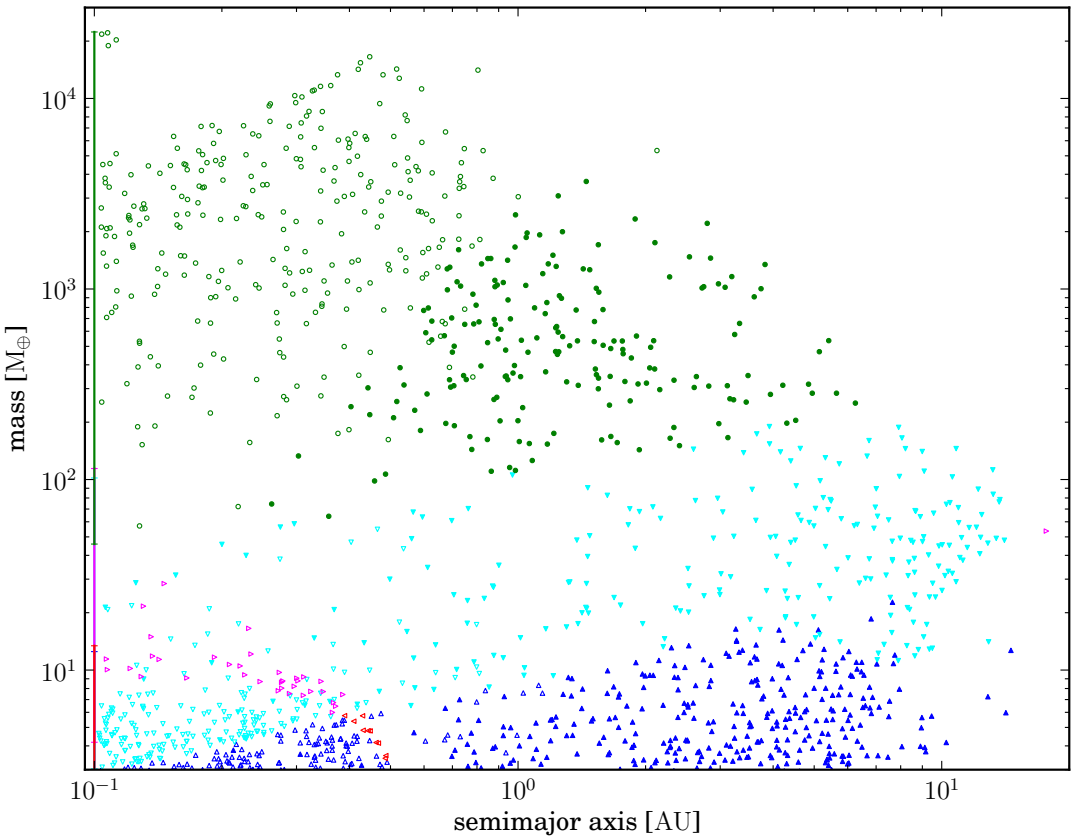

Figure 2.14 Final position of the planets in the semimajor axis mass diagram in the disks including stellar irradiation. The bars at 0.1 AU indicate the mass range of the "hot" planets in the different regimes. The meaning of the colors is the same as in Fig. 2.7. Filled (empty) symbols represent planets that never (sometime) migrated in their evolution in an adiabatic migration regime.

The irradiation also leads to higher disk accretion rates in the outer regions of the disk, since $\nu = \alpha c_s^2/\Omega \propto T$, and therefore to the faster depletion of the outer disk regions. The surface density is therefore lower in the irradiation case than in the non-irradiated at same time of the simulation. This leads to lower migration rates even in locally isothermal migration. This compensates to some degree the larger inward migration zones in our disks and the transition into locally isothermal migration at the end of the disk lifetime.

We used the same initial conditions as in all other syntheses. The different disk model leads to different disk lifetimes, therefore the results are only partially comparable. We considered 7700 planets more massive than 0.6 $M_\oplus$. From these planets 68.8% migrated to the inner border of our computational domain. From the planets with a final distance larger than 0.1 AU from the star $\approx$ 20% are more massive than 100 $M_\oplus$, which is similar to the ratio in our reference synthesis. The larger amount of "hot" planets is the result from the disappearing CZs at toward end of the disk evolution.

2.7 Summary and conclusions

We have compiled a prescription for type I migration based on the latest hydrodynamic simulations of planet-disk interactions. We tested the influence of the prescription on the outcome of the planetary population synthesis calculations. Our migration model is based on the combination of results from Paardekooper et al. (2010) and different time scales to distinguish between different migration regimes. These time scales reflect the thermodynamical behavior of the interaction between the planet and the surrounding disk like the horseshoe drag. We first compared the migration torques of this model with a model of Paardekooper et al. (2011) and with radiative-hydrodynamical simulations from Kley et al. (2009) and Bitsch and Kley (2011). The comparison of the theoretical torque curves with data from Kley et al. (2009) and Bitsch and Kley (2011) suggests that with an adjustment of the viscous time scale in the calculation of the saturation mass (the mass when the corotation torque starts to vanish) by a factor of $f_{\rm visc} \approx 0.55$ our model reproduces the torque better.

We also showed the global effects of different parameters of various migration models in a number of population synthesis calculations. Here, the comparison of our nominal BMF model ($f_{\rm visc} \approx 0.55$) and the migration model of Paardekooper et al. (2011) indicates similar results (Sect. 2.5.2) even with the difference shown in the torque curves.

Like Lyra et al. (2010),Kretke and Lin (2012), and Hellary and Nelson (2012), we also find with our prescription that nonisothermal type I migration leads to convergence zones (CZ), that is, points in a disk to which planets migrate to from the inside and outside. As in previous studies (Hellary and Nelson, 2012), we find that the convergence zones move inward as the disk evolves and take the captured planets with it. This occurs on the slower time scale of disk evolution and therefore the captured planets are trapped in it and also only migrate on this time scale. The planets leave this zone when their horseshoe drag saturates.

The difference between the migration rate of planets captured in a CZ and the migration rate in the saturated regime is significant. This means that an increase of the mass where saturation occurs by a modest factor of 2, for example, the time spent in rapid-saturated type I migration is significantly shortened and therefore also the extent of migration. The level of saturation at a given mass, and the mass at which saturation begins, are among the critical aspects for the evolution of a giant planet since small changes by a factor of 2 in $f_{\rm visc}$ can change the final distribution in the mass semimajor axis diagram by a measurable degree. But a similar degree of change in the final semimajor axis-mass distribution was seen when we changed the description of the Lindblad torque to the formula found by Masset and Casoli (2010).

Finally, we determined the formation tracks of a planet, illustrating that under certain conditions, a planet can loose almost all of its gas mass during its evolution. This mass loss can lead to a stop of migration for a few 10^5 years when the mass loss is strong enough to desaturate the horseshoe drag. The reason for the envelope mass loss is a jump in solid accretion rate, which is caused by the migration of the planet from a solid-depleted into a solid-rich region of the disk. This behavior strongly depends on the treatment of the planetesimal disk. Here we did not evolve the disk or changed the random velocities because of a giant planet. Both change the accretion rate and therefore whether or how this mass loss occurs.

Neither did we consider random variations in the torque due to turbulent density variations in the disk. Recent studies showed that in some cases random migration due to turbulence can dominate the migration behavior for low-mass planets (Papaloizou et al., 2004; Uribe et al., 2011). Depending on the strength of the random torque, it could push planets from the inner into the outer convergence zone even for the stronger Lindblad torque of Paardekooper et al. (2011).

We made no detailed comparison with observed extrasolar planet populations because the migration model is only a small part of the improvements to the overall model, and defer such comparisons to future work. But we quantified the impact of different model settings by studying the fractional yield of different planet types in a synthesis.

With the new nonisothermal migration model described here or that of Paardekooper et al. (2011) there are still about 50% of all low-mass planets lost in the innermost part of the disk. However, it is about a factor two better than the isothermal migration model without any artificial factors. One way to reduce the number of "lost" planets is an increase of the saturation mass. A lower critical mass for runaway gas accretion can also help due to the faster transition into type II migration (Hori and Ikoma, 2011). Furthermore, there are hints that there are additional effects leading to outward migration of planets in 3D simulations of magneto-hydrodynamic disks (Uribe et al., 2011).

We also note that up to now there is a shortcoming of all analytic torque predictions: they all neglect the fact that the horseshoe region is over-wide compared with the prediction used here when $q/h^3 \approx 1$ (Masset et al. (2006)). The fast growth of the width of the horseshoe region in that mass range (a few ten Earth masses to a hundred Earth masses) yields a boost of the corotation torque, which is a strong effect. In the

same mass range gap opening and the transition into type II migration occur. And as shown in Section 2.3.5, saturation plays a main role in the change of the direction of the torque in that mass range as well. Moreover, our fit of the torques data from Kley et al. (2009) and Bitsch and Kley (2011) depends on the progression of the torque curve in that mass range. This means that even when our fit produced the torque data well, a closer study of the torque in the mass range might uncover new effects, that may change the outcome of population synthesis calculations.

Nevertheless, the CZ or a similar effect might explain the concentration of planets in clusters one finds in distance-mass diagrams of observed extrasolar planets for high- and low-mass planets (Mayor et al., 2011). In particular, the absence of close-in, low-mass planets in Mordasini et al. (2009b) is not seen any longer with the updated migration model.

Additional comparisons of our results with new data from radial velocity measurements and Kepler data will be important, especially when we combine the new migration model with new improvements of our model, i.e., the long term evolution of giant planets (Mordasini et al., 2012b) and the concurring evolution of multiple planets per disk (Ida and Lin, 2010; Alibert et al., 2013). Multiple cores in one disk might be collected into one CZ and form one larger core. Therefore the convergence region may function as a large feeding zone of solid matter onto a core captured in a convergence zone and thus enhance the solid accretion rate (Hellary and Nelson, 2012; Sándor et al., 2011; Horn et al., 2012). Moreover, in particular the low-mass planets of the inner cluster only migrated through the inner convergence region. The outer boundary of this region is due to the transition in the gas opacity at the iceline. This means that all these planets moved only through the ice-free part of the protoplanetary disk. We will also study the global effects of different viscous α values and deadzones on the behavior of the convergences zones with population synthesis calculations (cf. Hasegawa and Pudritz, 2011). This brings us closer to a description of orbital migration without ad hoc efficiency factors.

2.8 Acknowledgements

We thank Betram Bitsch for providing important data for the radiation hydrodynamic calculations, and Willy Benz, Kees Dullemond, Willy Kley and Sijme-Jan Paardekooper for enlightening discussions. This work was supported in part by the Swiss National Science Foundation and the European Research Council under grant 239605. We thank an anonymous referee whose comments lead to a substantial clarification of the manuscript. Christoph Mordasini thanks the Max-Planck-Gesellschaft for the Reimar-Lüst Fellowship. Kai-Martin Dittkrist thanks the International Max Planck Research School for Astronomy and Cosmic Physics at the University of Heidelberg.

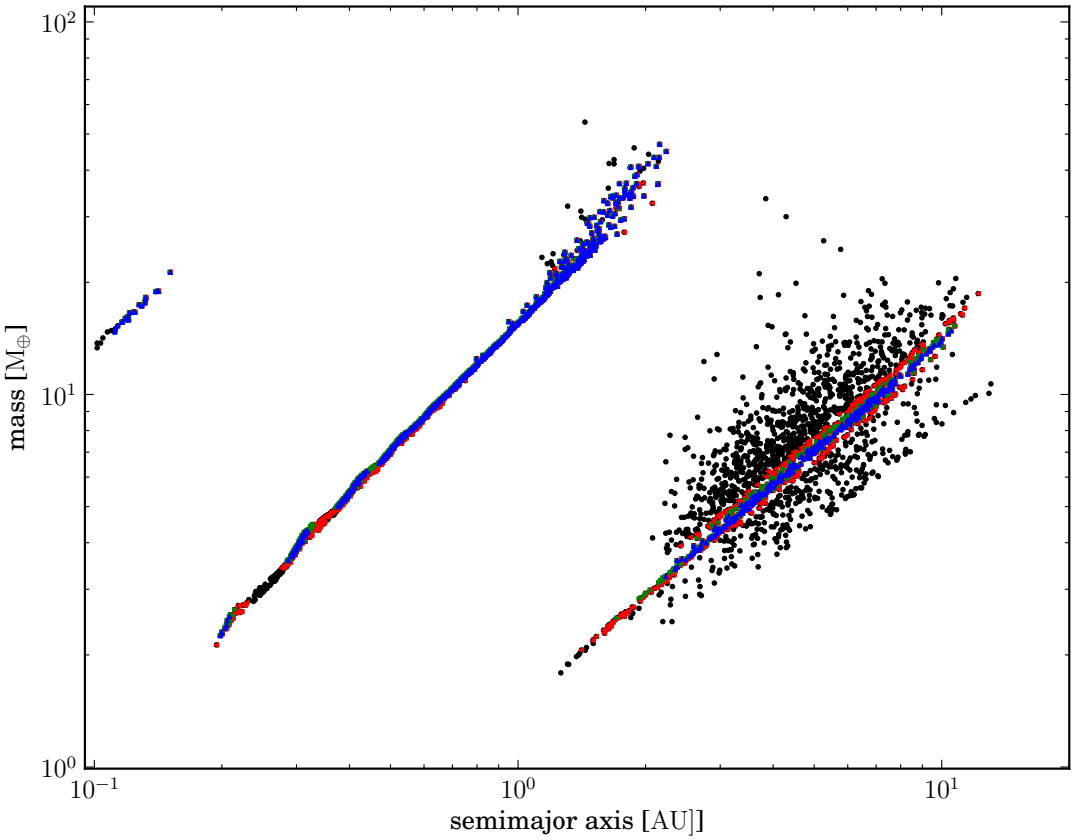

Figure 2.15 Position of a planet in the nominal synthesis calculation when it transitions from the unsaturated adiabatic migration regime into the saturated adiabatic migration regime. Colored are the planet which distance is less than 3% (blue, up facing triangles), 5% (green, right facing triangles) or 10% (red, left facing triangles) from a CZ.

2.9 appendix

2.9.1 Saturation and disk evolution

From the positions of planets at the time of saturation in the formation tracks in Figure 2.7 in Section 2.4.5 one sees that most positions lie on two lines, one for the planets of the inner and one for the outer CZ. We study here the reasons for this feature.

Figure 2.15 shows the positions of the planets at the transition from unsaturated to saturated adiabatic migration, the most common transition into a saturated migration regime. The positions of all planets undergoing this transition are shown in black, while the colored points show that those with a distance between their semimajor axis and the position of the CZ at that time are fewer than 10% of the semimajor axis. There are two large groups, again one of the inner and one of the outer convergence region. Almost all planets of the inner group are in the CZ when they saturate, while the outer ones are much more spread out. But the planets that are in the CZ form a line here as

well. There is a third CZ inside of 0.3 AU in the most massive disks in the synthesis, which leads to a third minor group. However, this CZ evolves quickly and disappears after the first few 0.01 Myr and all associated planets end at 0.1 AU. The dozen points inside of 0.2 AU in Fig. 2.15 correspond to planets in this small CZ.

This behavior results from the interaction of the following points:

One can calculate the saturation mass as a function of the orbital distance a and time t by setting $s_2 = 1$ in Eq. 2.17. There, $f_{\rm visc}$ is 1, 0.55 or 0.125 in each of the model versions.

$$M_{\rm sat}(a,t) = \frac{h(a,t)}{1.16}\left(\frac{8\pi M_{\rm star}\nu(a,t)}{3f_{\rm visc}}\right)^{\frac{2}{3}}\frac{1}{(Ga)^{1/3}}. \tag{2.28}$$

For a fixed orbital distance and stellar mass it only depends on the disk aspect ratio h and the viscosity ν. Both quantities are decreasing with time, as the disk mass decreases, and therefore, the saturation mass also becomes smaller as the disk evolves.

While the photoevaporation rate is important for the lifetime of a disk, the constant value of α in all simulations of one synthesis results in a similar disk structure in the part of the disk where viscosity is dominant. There, the disks go through the same series of disk states (radial profile of temperature, surface density, etc.) and only the speed with which the disks go through the states is different and depends on the photoevaporation rate. Given one semimajor axis a, there is only one disk state where the inner (our outer) CZ lie at this position. Therefore also h and ν are fixed for this semimajor axis of the CZ. Therefore, the semimajor axis of the CZ corresponds to only one saturation mass. And as the CZ moves inward while the disk evolves, the saturation mass decreases. Both processes approximately follow power-laws and thus we see a line-like structure for the planets that saturate while they are in one CZ. Planets that saturate early in the disk evolution do so at a higher mass and farther out than planets that saturate in later times of disk evolution.

Finally, the spread in the outer group results from planets that saturated before they reached the CZ. These are planets in disks with high solid surface densities where the planet cores can grow fast. Compared with the inner group, the outer group also contains more planets that saturate outside of the CZ. The larger amount of solids outside of the iceline leads to higher accretion rates. The scatter is reduced when the saturation mass is increased by reducing $f_{\rm visc}$. The higher saturation mass gives the planets more time to migrate to the CZ and to saturate there.

2.9.2 Impact of numerical parameters

We made several population syntheses calculation to test the effects of different numerical parameters and comment on the effects here.

We made calculations with the STD model and exponents $b = 2.0$ and $b = 10.0$ (nominal value $b = 4.0$) in the transition function between locally isothermal and adiabatic migration regime (Eq. 2.20). This only has a small effect for low-mass planets, while for massive planets the final semimajor axis and mass is almost the same for different values of b. At smaller masses no clear pattern can be seen. An increase of b

can lead to either more or less massive planets and to either larger or smaller distances from the star of a few per cent.

We also made calculations with $b = 4.0$ and a hard jump for the transition function between type I and type II migration (Eq. 2.23) (nominal value $b = 10$. This only affects massive planets and gives only a change in distance from the star of a few percent, with a larger b leading to planets farther away from the star but almost no change in the final mass.

Overall, the range of the different parameters studied here only leads to minor changes in the overall distribution of planets in semimajor axis and mass.

Chapter 3

Temperature Model

The last chapter and similar work (Kretke and Lin, 2012) showed that for small mass planets migration can stop or turn outward. In Mordasini et al. (2012a) the new migration model lead to different planet radius distributions for different masses. One reason for this was, that the inner edge of the disk which is fixed at the inner border of the computational domain. Benítez-Llambay et al. (2011) showed that the inner edge of the disk will at least stop all type I migrating planets. Thus the stopping point of the hot planets in Mordasini et al. (2012a) was at the same position for the different regimes and ages. Nevertheless, the mass distribution of these planets showed features that were also seen in the observed data (Benítez-Llambay et al., 2011). So the real position of the inner edge is important, yet is lies mostly closer than 0.1 AU from the star where the old model ended. Also recent studies showed that type II migration is more complex than our simple description in the previous chapter (Duffell et al., 2014; Edgar, 2007).

The idea of the inclusion of more complex type II migration descriptions and a flexible inner edge led to the idea to create a new disc evolution model, which brings up the need for a description of the midplane temperature for a large range of different conditions.

In this chapter we present the temperature model used to calculate the midplane temperature in our disc model. A short overview of the model and underlying assumptions will be followed by a presentation of the calculation of the relevant equations. We present two temperature models, one called the full temperature model (FTM) and the approximated temperature model (ATM). In the latter, we approximated the gas density at the surface, or photospheric density, which will be called At the end of the chapter we discuss the resulting feature of the midplane temperature profile.

3.1 Two Layer Model

Since the disk will extend close to the star we have to consider not only radiative energy transport from the midplane to the surface but also convective processes. We

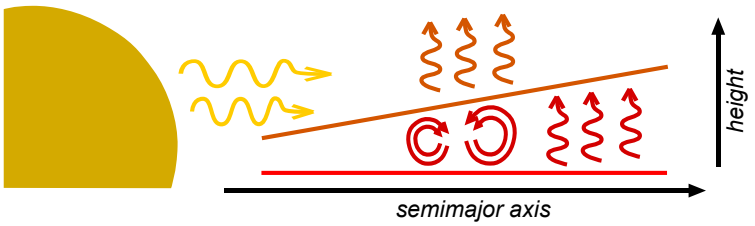

Figure 3.1 Sketch of the temperature model. Irradiated from the star, the disc is assumed to be either completely convective or radiative below the surface and only radiative above the surface.

therefore impose the following assumptions –see Figure 3.1 for an illustration – when we calculate the midplane temperature of the disc:

- The hard nontransparent surface of the disk has a height H_s, at which incoming radiation is absorbed and heat is radiated away.
- The disk is optically thin and in isothermal radiative equilibrium with the surrounding above that height; a isothermal density profile applies.
- The disk is either fully radiative or fully convective below the surface. Midplane temperatures of either transport method are calculated and the lower one is chosen. Furthermore, all internal heating is released at the midplane itself.

This is a simplification of the real processes happening in a disk. Irradiation can penetrate to different depth and viscous processes release energy over the whole vertical scale. Also radiation is ever present, and mostly dominant, so convective processes never account for the whole energy transport (Cassen, 1993). Actually convective processes are responsible for only up to 20% of the vertical energy transport in typical disk. And while in our model the midplane is always hotter than the surface, in reality, temperature inversions can occur if the surface is optically thick for short wavelength radiation, but optically thin for long wavelengths (Dullemond et al., 2002).

In the following paragraphs, we will present the calculation of the relevant quantities, first the surface temperature, then the density at the surface, the height of the surface, and the midplane temperature in both transportation cases.

3.1.1 Radiative surface of the disc

In general, the energy produced by the viscous heating is transported to the radiative surface of the disc and emitted from there. On this surface radiation from the host star is also absorbed. The energy balance for an annulus with the area $A = 2\pi a \Delta a$ at semimajor axis a at the surface therefore leads to:

$$AQ^+ = 2P_{\text{out}} - 2P_{\text{in}}. \tag{3.1}$$

On the left side, we have the viscous heat production rate (Nakamoto and Nakagawa, 1994) in an infinitesimal wide anulus around the host star:

$$Q^+ = -\frac{1}{2\pi a} g_c \frac{\partial \Omega}{\partial a} = \nu \Sigma a^2 \left(\frac{\partial \Omega}{\partial a} \right)^2, \tag{3.2}$$

with viscosity ν, surface density Σ, and the couple (Lynden-Bell and Pringle, 1974)

$$g_c = 2\pi a^3 \nu \Sigma \frac{\partial \Omega}{\partial a}. \tag{3.3}$$

We also neglect self gravity of the disk throughout this work (except for a gravo-turbulent α, see Section 4.4) and radial pressure forces. We thus have a Keplerian profile for the rotation frequency of the gas disk $\Omega = \sqrt{GM_{\text{star}}/a^3}$:

$$\frac{\partial \Omega}{\partial a} = -\frac{3\Omega}{2a}. \tag{3.4}$$

On the right side of Equation (3.1), we have the out going power (thermal radiation of the surface)

$$P_{\text{out}} = \sigma_{\text{SB}} A T_s^4 \tag{3.5}$$

and incoming power P_{in}. T_s denotes the surface temperature of the disk and σ_{SB} the Stefan-Boltzmann constant.

The incoming power consists of luminosity irradiating onto the disk from the host star and from the background environment (Ruden and Pollack, 1991; Hueso and Guillot, 2005):

$$P_{\text{in}} = L_{\text{irr}} = \sigma_{\text{SB}} A T_{\text{star}}^4 \left(\frac{2}{3\pi} \left(\frac{R_{\text{star}}}{a} \right)^3 + \frac{1}{2} \frac{H_s}{a} \left(\frac{R_{\text{star}}}{a} \right)^2 \left(\frac{d \ln(H_s)}{d \ln(a)} - 1 \right) \right) + \sigma_{\text{SB}} A T_{\text{bg}}^4. \tag{3.6}$$

T_{star} denotes the temperature of the host star and R_{star} its radius, T_{bg} is the temperature of the background radiation, which is assumed to be 10 K, and H_s is the height of the disc surface.

Inserting these into Equation (3.1) leads to

$$\frac{1}{2} Q^+ + \frac{L_{\text{irr}}}{2\pi a \Delta a} = \sigma_{\text{SB}} T_s^4, \tag{3.7}$$

which allows us to calculate the surface temperature, given that we know the irradiation profile and the internal heating.

3.1.2 Vertically isothermal part

To obtain the gas density at the surface we first set the vertical temperature and density profile above the radiative surface. The disk is optically thin and isothermal (Blabla, 20xx):

$$T(z > H_s) = T_{\text{iso}} = T_s. \tag{3.8}$$

This leads to a Gaussian vertical density profile above the surface

$$\rho_{\mathrm{iso}}(z) = \rho_{0,\mathrm{iso}} e^{-z^2/(2H^2_{\mathrm{iso,s}})}, \tag{3.9}$$

where $\rho_{0,\mathrm{iso}}$ denotes the hypothetical isothermal midplane density (if the isothermal layer would extend to the midplane) and $H_{\mathrm{iso,s}}$ the scaling length or scale height of the surface. With the isothermal soundspeed

$$c_{\mathrm{s}} = \frac{\partial p}{\partial \rho} = H\Omega, \tag{3.10}$$

we can calculate the surface scale height as

$$H_{\mathrm{iso,s}} = \frac{1}{\Omega}\sqrt{\frac{k_{\mathrm{B}}}{\mu} T_{\mathrm{s}}}. \tag{3.11}$$

Throughout this work we use the general equation of state

$$p = \frac{k_{\mathrm{B}}}{\mu(T,\rho)} \rho T, \tag{3.12}$$

where p is the pressure, T the temperature, ρ the density, k_{B} the Boltzmann constant, and $\mu(T,\rho)$ the mean molecular weight of the gas. The latter one depends itself on the temperature and density of the gas. We use equations from Blabla (20xx) (Klahr/Benz? Need a citation) to calculate the mean molecular weight for a given density and temperature.

To calculate the height H_{s} of the radiative surface, we assume that the optical depth τ above H_{s} equals 2/3, as the disk is optically thin:

$$\frac{2}{3} = \tau_{\mathrm{s}} = \int_{H_{\mathrm{s}}}^{\infty} \kappa_{\mathrm{s}} \rho_{\mathrm{iso}}(z) dz. \tag{3.13}$$

We further assume that the opacity κ_{s} does not change above H_{s}. Formally

$$\tau_{\mathrm{s}} = \kappa_{\mathrm{s}}(T_{\mathrm{s}}, \rho_{\mathrm{s}}) \rho_{0,\mathrm{iso}} \int_{H_{\mathrm{s}}}^{\infty} e^{-z^2/2H^2_{\mathrm{iso,s}}} dz. \tag{3.14}$$

Furthermore we use the hydrostatic equilibrium for a thin disc in combination with the EOS (Equation (3.12)):

$$p_{\mathrm{s}} = \frac{k_{\mathrm{B}}}{\mu} \rho_{\mathrm{s}} T_{\mathrm{s}} = \Omega^2 \int_{H_{\mathrm{s}}}^{\infty} z \rho_{\mathrm{iso}}(z) dz \approx \Omega^2 H_{\mathrm{s}} \frac{\tau_{\mathrm{s}}}{\kappa_{\mathrm{s}}} = \Omega^2 H_{\mathrm{s}} \frac{\tau_{\mathrm{s}}}{\kappa_{\mathrm{s}}}. \tag{3.15}$$

This is similar to the Eddington boundary condition in atmospheres, which states that $Omega^2 H$ equals the vertical gravity. Since $\rho_{\mathrm{iso}}(z)$ drops relatively fast, only the first part of the integral is important. Therefore, $z \approx H_{\mathrm{s}}$. This approximation, which leads to the last part of the equation above, may be to strong. If the integral is evaluated analytically, the approximation simply leads to the conclusion that the density profile fulfills the equation of state. For further discussion, see Section 3.2.1.

Finally, rewriting Equation (3.14), evaluating the integral and substituting $\rho_{0,\mathrm{iso}}$ (3.9) yield:

$$0 = e^{H_\mathrm{s}^2/2H_{\mathrm{iso,s}}^2}\,\mathrm{erfc}\left(\frac{H_\mathrm{s}}{\sqrt{2}H_{\mathrm{iso,s}}}\right) - \frac{\tau_\mathrm{s}}{\kappa_\mathrm{s}(T_\mathrm{s},\rho_\mathrm{s})\rho_\mathrm{s}H_{\mathrm{iso,s}}}\sqrt{\frac{2}{\pi}}. \tag{3.16}$$

We can use this equation to calculate the height of the radiative surface when we know the gas density at the radiative surface ρ_s. This density will depend on whether the transport process below is convective or radiative. Since we use the name *surface density* for the vertically integrated density Σ, we will call ρ_s also the photospheric density throughout this work. The left part of the right hand side has a maximal value of 1. Hence, the equation above is no solvable if the density gets too small. This means that even for a surface height of zero there is not enough gas to make a optically thick midplane layer. Since the disc is assumed to be completely optically thin and isothermal, the midplane temperature is also the surface temperature. This will apply mostly for surface densities below $5{\cdot}10^{-1}\mathrm{g/cm^2}$, as we shown in Section 3.2.

3.1.3 Vertically convective/adiabatic

If the vertical temperature gradient becomes to large a atmosphere will turn from being radiative to adiabatic according to the Schwarzschild criteria (Schwarzschild, 1958).. This means that the energy produced in the midplane is transported by convection to the surface and not by radiation. Before we look at the radiative case in Section 3.1.4, let us first assume the disc is convective from the midplane up to the height of the surface H_s and that the rising and falling eddies do not lose any energy to radiation. This makes the process adiabatic. The following three equations describe in general the vertical structure of a pure convective disk atmosphere (Goldreich and Weber, 1980). The pressure is

$$p(z) = p_\mathrm{A}\left(1 - \left(\frac{z}{H_\mathrm{A}}\right)^2\right)^{\frac{\gamma}{\gamma-1}}, \tag{3.17}$$

the temperature is

$$T(z) = T_\mathrm{A}\left(1 - \left(\frac{z}{H_\mathrm{A}}\right)^2\right), \tag{3.18}$$

and the density

$$\rho(z) = \rho_\mathrm{A}\left(1 - \left(\frac{z}{H_\mathrm{A}}\right)^2\right)^{\frac{1}{\gamma-1}}. \tag{3.19}$$

All values with the subscript A denote the adiabatic midplane values of the quantity. H_A is the adiabatic scale height at which the temperature, the density and the pressure is zero. The adiabatic coefficient γ is given by the EOS evaluated at the midplane. The values at the surface $z = H_\mathrm{s}$ are thus:

$$p_\mathrm{s} = p_\mathrm{A}\left(1 - \left(\frac{H_\mathrm{s}}{H_\mathrm{A}}\right)^2\right)^{\frac{\gamma}{\gamma-1}}, \tag{3.20}$$

$$T_s = T_A \left(1 - \left(\frac{H_s}{H_A}\right)^2\right), \tag{3.21}$$

$$\rho_s = \rho_A \left(1 - \left(\frac{H_s}{H_A}\right)^2\right)^{\frac{1}{\gamma-1}}. \tag{3.22}$$

We can thus also calculate the midplane pressure by extending the hydrostatic equilibrium to the midplane and splitting the integral:

$$p_A = \Omega^2 \int_0^\infty z\rho(z)dz = p_s + \Omega^2 \int_0^{H_s} z\rho(z)dz. \tag{3.23}$$

We insert the density profile, and solve the integral

$$p_A - p_s = \Omega^2 \rho_A H_A^2 \frac{\gamma-1}{2\gamma}\left(1 - \left(1 - \frac{H_s^2}{H_A^2}\right)^{\frac{\gamma}{\gamma-1}}\right). \tag{3.24}$$

Using Equation (3.20) leads to

$$p_A = \Omega^2 \rho_A H_A^2 \frac{\gamma-1}{2\gamma}. \tag{3.25}$$

We apply the EOS to substitute pressure and density and solve for the adiabatic scale height:

$$H_A = \sqrt{\frac{k_B}{\mu} T_A \frac{2\gamma}{\gamma-1}\frac{1}{\Omega^2}}. \tag{3.26}$$

If we compare this with Equation (3.11) one sees that the adiabatic scale height is similar to the isothermal scale height except for the factor $2\gamma/(\gamma-1)$, which makes it always larger than H_{iso}, since the adiabatic coefficient $\gamma \geq 1$.

Inserting this in Equation (3.21), gives us the midplane temperature:

$$T_A = T_s + \frac{\gamma-1}{2\gamma}\frac{\mu}{k_B} H_s^2 \Omega^2. \tag{3.27}$$

So if we know the radiative surface height H_s and temperature T_s, we can calculate the midplane temperature in the adiabatic case.

We can also insert Equation (3.21) into Equation (3.26) to get an expression where H_A only depends on H_s and T_s:

$$H_A = \sqrt{H_s^2 + \frac{k_B}{\mu} T_s \frac{2\gamma}{\gamma-1}\frac{1}{\Omega^2}} = \sqrt{H_s^2 + H_\Delta^2}, \tag{3.28}$$

where we define

$$H_\Delta = \sqrt{\frac{k_B}{\mu} T_s \frac{2\gamma}{\gamma-1}\frac{1}{\Omega^2}}. \tag{3.29}$$

Finally we use the definition of the surface density

$$\Sigma = 2\int_0^\infty \rho(z)dz \tag{3.30}$$

and insert both density profiles to get:

$$\frac{\Sigma}{2} = \rho_{0,\mathrm{iso}}\int_{H_\mathrm{s}}^\infty e^{-z^2/2H_{\mathrm{iso,s}}^2}dz + \rho_\mathrm{A}\int_0^{H_\mathrm{s}}\left(1-\left(\frac{H_\mathrm{s}}{H_\mathrm{A}}\right)^2\right)^{\frac{1}{\gamma-1}}dz. \tag{3.31}$$

We define the integral

$$I_\mathrm{A}\left(\frac{H_\mathrm{s}}{H_\mathrm{A}},\gamma\right) = \int_0^{H_\mathrm{s}/H_\mathrm{A}}\left(1-z'^2\right)^{\frac{1}{\gamma-1}}dz' \tag{3.32}$$

to get

$$\frac{\Sigma}{2} = \rho_\mathrm{s}H_{\mathrm{iso,s}}\sqrt{\frac{\pi}{2}}e^{H_\mathrm{s}^2/2H_{\mathrm{iso,s}}^2}\,\mathrm{erfc}\left(\frac{H_\mathrm{s}}{\sqrt{2}H_{\mathrm{iso,s}}}\right) + \rho_\mathrm{s}H_\mathrm{A}\left(1-\left(\frac{H_\mathrm{s}}{H_\mathrm{A}}\right)^2\right)^{\frac{1}{1-\gamma}}I_\mathrm{A}\left(\frac{H_\mathrm{s}}{H_\mathrm{A}},\gamma\right). \tag{3.33}$$

In most cases the radiation surface H_s will be much higher than $H_{\mathrm{iso,s}}$. And, as can be seen in Equation (3.28) H_A is always larger than H_s.

$$\frac{\Sigma}{2} = \rho_\mathrm{s}H_{\mathrm{iso,s}}\sqrt{\frac{\pi}{2}}e^{H_\mathrm{s}^2/2H_{\mathrm{iso,s}}^2}\,\mathrm{erfc}\left(\frac{H_\mathrm{s}}{\sqrt{2}H_{\mathrm{iso,s}}}\right) + \rho_\mathrm{s}H_\Delta^{\frac{2}{1-\gamma}}\left(H_\mathrm{s}^2+H_\Delta^2\right)^{\frac{\gamma+1}{2(\gamma-1)}}\int_0^{H_\mathrm{s}/H_\mathrm{A}}\left(1-z'^2\right)^{\frac{1}{\gamma-1}}dz' \tag{3.34}$$

Together with Equation (3.28), this gives us the photospheric density

$$\rho_\mathrm{s} = \frac{\Sigma}{2}\frac{1}{H_{\mathrm{iso,s}}\sqrt{\frac{\pi}{2}}e^{H_\mathrm{s}^2/2H_{\mathrm{iso,s}}^2}\,\mathrm{erfc}\left(\frac{H_\mathrm{s}}{\sqrt{2}H_{\mathrm{iso,s}}}\right) + \left(\frac{H_\Delta}{H_\mathrm{A}}\right)^{\frac{2}{1-\gamma}}H_\mathrm{A}I_\mathrm{A}\left(\frac{H_\mathrm{s}}{H_\mathrm{A}},\gamma\right)}. \tag{3.35}$$

We have now two Equations (3.16) and (3.35) to solve simultaneously for the surface height and photospheric density in the adiabatic case. We can then calculate the adiabatic scale height and then also the midplane temperature, the density and the pressure.

3.1.4 Vertically radiative

After evaluating Equations (3.16) and (3.35) to get a set of formulas in the adiabatic regime, we now determine the fully radiative disc profile. For the radiative midplane temperature we use (Hubeny, 1990; Nakamoto and Nakagawa, 1994)

$$T_{0,\mathrm{rad}} = T_\mathrm{s}\left(\frac{3}{8}\tau_\mathrm{R}(T_{0,\mathrm{rad}},\rho_{0,\mathrm{rad}}) + 1 + \frac{1}{2\tau_\mathrm{P}(T_{0,\mathrm{rad}},\rho_{0,\mathrm{rad}})}\right)^{0.25}, \tag{3.36}$$

with the optical depth

$$\tau_{\mathrm{R/P}}(T_{0,\mathrm{rad}}, \rho_{0,\mathrm{rad}}) = 0.5\kappa_{\mathrm{R/P}}(T_{0,\mathrm{rad}}, \rho_{0,\mathrm{rad}})\Sigma, \tag{3.37}$$

where $\kappa_{\mathrm{R/P}}$ denotes the Rossland or Planck opacity respectively and $\tau_{\mathrm{R/P}}$ the corresponding optical depth. We use the same opacity tables (Bell and Lin, 1994) as in our old model. They only contain Rossland mean opacities. To get the Planck values we use the approximation of Nakamoto and Nakagawa (1994) that $\kappa_{\mathrm{P}} \approx 2.4\kappa_{\mathrm{R}}$.

Similar to the isothermal case, we assume a Gaussian density profile also for the part below the surface

$$\rho_{\mathrm{rad}}(z) = \rho_{0,\mathrm{rad}} e^{-z^2/2H_{\mathrm{rad}}^2}, \tag{3.38}$$

where the radiative scale height is

$$H_{0,\mathrm{rad}} = \frac{1}{\Omega}\sqrt{\frac{k_{\mathrm{B}}}{\mu}T_{0,\mathrm{rad}}} \tag{3.39}$$

to calculate the only unknown quantity on the right side, the midplane density $\rho_{0,\mathrm{rad}}$.

We again use the definition of the surface density Equation (3.30) and split it in two parts:

$$\frac{\Sigma}{2} = \rho_{0,\mathrm{iso}} \int_{H_{\mathrm{s}}}^{\infty} e^{-z^2/2H_{\mathrm{iso,s}}^2} dz + \rho_{0,\mathrm{rad}} \int_0^{H_{\mathrm{s}}} e^{-z^2/2H_{0,\mathrm{rad}}^2} dz. \tag{3.40}$$

We us for the first part of the right hand side of Equation (3.32) and for the second part

$$\rho_{0,\mathrm{rad}} \int_0^{H_{\mathrm{s}}} e^{-z^2/2H_{0,\mathrm{rad}}^2} dz = \rho_{\mathrm{s}} H_{0,\mathrm{rad}} e^{H_{\mathrm{s}}^2/2H_{0,\mathrm{rad}}^2} \sqrt{\frac{\pi}{2}} \operatorname{erf}\left(\frac{H_{\mathrm{s}}}{\sqrt{2}H_{0,\mathrm{rad}}}\right). \tag{3.41}$$

This yields

$$\frac{\Sigma}{2} = \rho_{\mathrm{s}} H_{\mathrm{iso,s}} \sqrt{\frac{\pi}{2}} e^{H_{\mathrm{s}}^2/2H_{\mathrm{iso,s}}^2} \operatorname{erfc}\left(\frac{H_{\mathrm{s}}}{\sqrt{2}H_{\mathrm{iso,s}}}\right) + \rho_{\mathrm{s}} H_{0,\mathrm{rad}} \sqrt{\frac{\pi}{2}} e^{H_{\mathrm{s}}^2/2H_{0,\mathrm{rad}}^2} \operatorname{erf}\left(\frac{H_{\mathrm{s}}}{\sqrt{2}H_{0,\mathrm{rad}}}\right). \tag{3.42}$$

Like in the adiabatic case we got a second equation of surface height and photospheric density of the surface. Yet this one also depends directly on the midplane temperature through $H_{0,\mathrm{rad}}$.

3.2 Midplane temperature

With the set of equations given in the previous section, we can calculate the midplane temperature if we know the surface temperature T_{s}, the surface density Σ, and the orbital frequency Ω. Since the model has to work for a huge range of different settings, we use these three variables to tabulate the midplane temperature and all associated quantities like midplane pressure, surface height, mean molecular weight or adiabatic coefficient. This gives us much faster computing times than calculating the temperature on the fly (See Section 4.1.1). We choose those three since they provide us with the

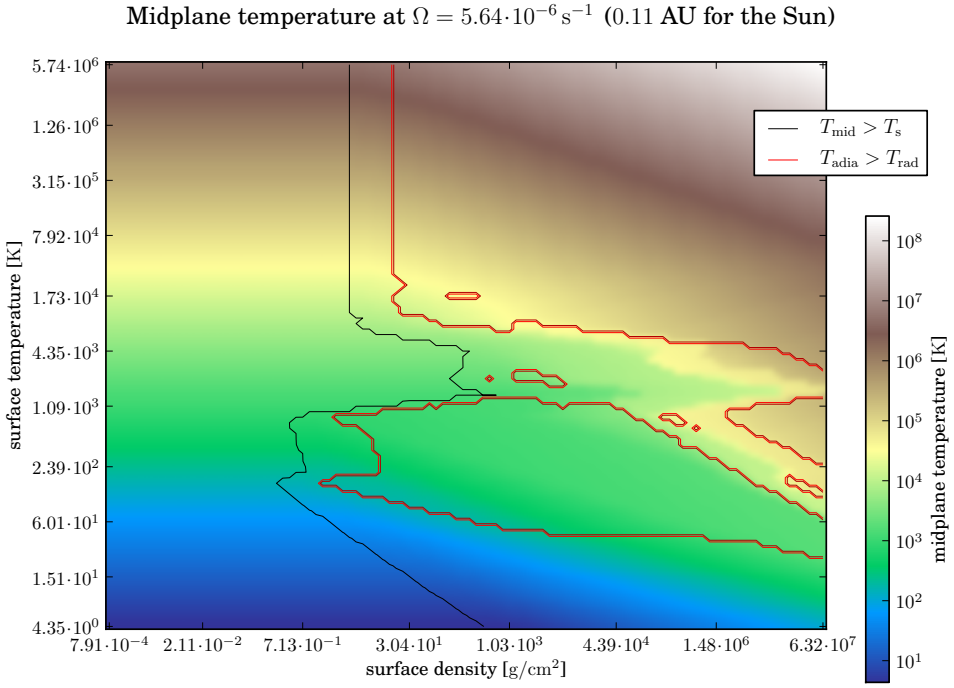

Figure 3.2 Midplane temperature at 0.11 AU of a solar-mass star for different surface densities and temperatures. The black line marks where the midplane temperature rises above the surface temperature. The double red line shows the boundary between the regions where the disc is radiative or convective, the light red line oriented towards the adiabatic/convective region.

smallest set of inputs to get a reasonable sized table. Since we will have varying host star masses, we cannot use the semimajor axis of the gas thus the use of the orbital frequency. Also the surface temperature T_s combines many different quantities and is easily calculated. Of course one of those quantities is the midplane temperature itself (see Equation (3.7)) so we have to iterate a few times to converge onto a self consistent solution.

Our tabulated range is between $0.025 M_{\text{sun}}$ and $5 M_{\text{sun}}$ for stellar masses and 0.003 AU and 30000 AU for the semimajor axis. This leads to a range of approximately $6 \cdot 10^{-15} \text{s}^{-1}$ to $2.7 \cdot 10^{-3} \text{s}^{-1}$ for the orbital frequency Ω. Surface temperatures vary between 5K and $5 \cdot 10^6$K and surface densities between 10^{-3}g/cm^2 and $5 \cdot 10^7 \text{g/cm}^2$. These are the extreme values of the table and are not used in general. E.g. the upper boundary for the surface temperature is in the rage of hydrogen burning, which is not included in the model. The model is thus not realistic at these extreme values. However, if those extreme surface densities or temperatures are reached, it will be in the innermost part of the disk only for a very short time of the evolution. And since the evolution of the disk is regulated by the structure of and mass flow from the outer disk the lifetime and overall shape of the disk is not influenced by this.
The generated table has 103·108·103 data points for surface temperature, surface density and orbital frequency respectively.

Figure 3.2 shows a slice of the midplane temperature over surface density and surface temperature for one of the orbital frequency ($\Omega = 5.64 \cdot 10^{-6} \text{s}^{-1}$) of the table. For a disk around a star with one solar-mass this corresponds to a semimajor axis of ≈ 0.11AU.

Left of the black line midplane temperature and surface temperature are the same. According to the model, the gas densities are too low, such that the disk is optical thin in the vertical direction and the height of the radiative surface drops to zero (see Figure 3.3 of the height of the radiative surface). A small increase in midplane temperature would lead to a huge temperature gradient. This part is assumed to be convective. Yet this convective layer is of zero height. Furthermore, the effective optical depth (see Equation (3.37)) increases after the density drops below a certain value. Hence, the radiative midplane temperature rises again for small surface densities in the model. As can also be seen in the figure, coming from small densities into the regions where the temperature leaves the isothermal part, the radiative midplane temperature rises also before the midplane temperature, while the adiabatic profile overtakes it for almost all surface temperatures.
For low surface temperatures, the model stays adiabatic for all surface densities. The opacity above the radiative surface is here too small to rise the radiative surface height much above zero. The disk is still almost vertically isothermal. The lower border between adiabatic and radiative regions is the iceline transition at midplane temperatures of 170 K. The forming of ice crystals below that temperature leads to an increase in optical depth that lifts the radiative temperature above the adiabatic one. One should also note that the model assumption of a solid radiative surface is not really valid for low densities or surface temperatures. This assumption leads to an overestimate of the efficiency of adiabatic energy transport processes, which results in too low midplane temperatures. For further discussion of this issue, see Section 3.3.

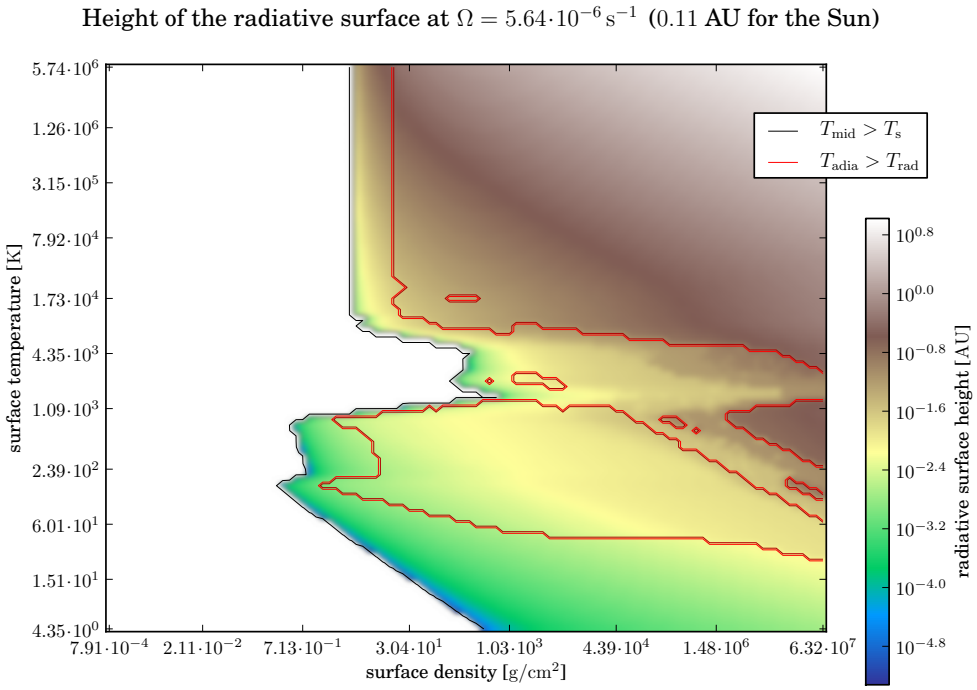

Figure 3.3 Height of the radiative surface at 0.11 AU of a solar-mass star for different surface densities and temperatures.

Another interesting feature is the adiabatic "main valley" for surface temperatures between roughly 1000 K and 5000 K. Here. the surface temperature is in a regime where the opacity gets density depended. This leads to a drop of the surface opacity for small surface densities ($\Sigma < 100\mathrm{g/cm}^2$, see Figure 3.5). Thus, the surface height drops for these low densities and the vertical temperature gradient increases and the disk turns convective. Therefore, the disc is vertical isothermal up to around a few hundred $\mathrm{g/cm}^2$, instead of less than one $\mathrm{g/cm}^2$ for lower or higher surface temperatures. For large densities, it is the increase in surface opacity which rises the radiative midplane temperature above the adiabatic one. The midplane temperature even decreases with a rising surface temperature for some large surface densities . The reason therefore is the same as above and in some cases due to a change in the mean molecular weight or adiabatic coefficient.

The last feature we discuss is the "side valley" of convective midplane temperature. This is due to the raise in midplane opacities due to the increasing midplane densities similar to the raise of the surface opacities for the "main valley". Therefore, the radiative midplane temperature raises above the adiabatic midplane temperature (see Equation (3.37)) because of the following increase in the effective optical depth. This effect is due to the midplane opacities, because there is no change in color, and therefore opacity, for the "side valley" indicating a change in surface opacities in Figure 3.5 while one sees such a change in Figure 3.4.

Both of these effects can be seen in Figure 3.6. Here we show the ratio of the differ-

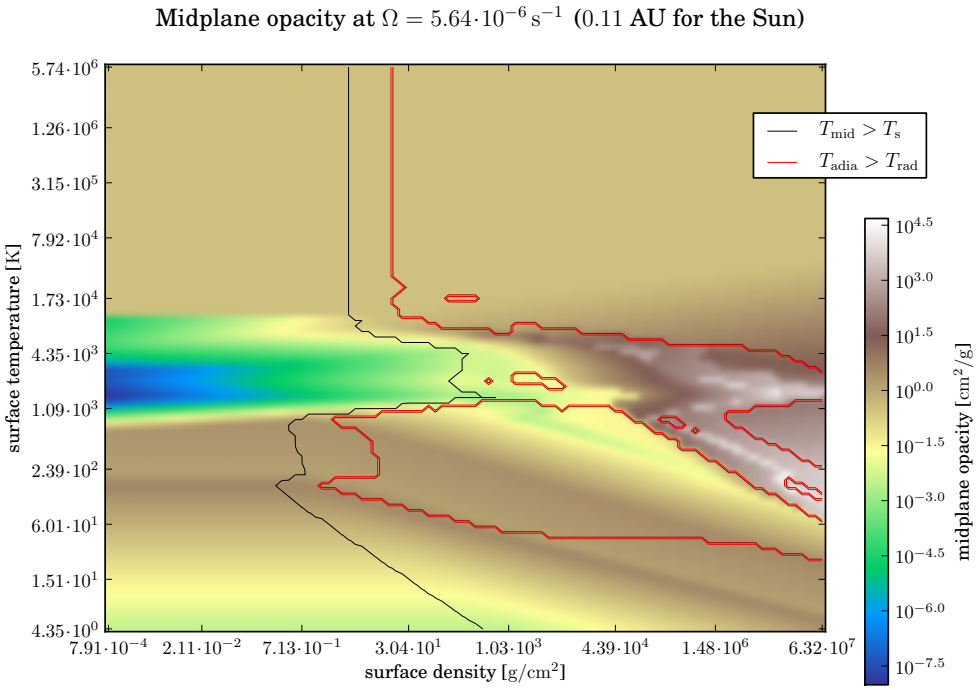

Figure 3.4 Midplane opacity at 0.11 AU of a solar-mass star for different surface densities and temperatures.

ence between the radiative and the adiabatic midplane temperature and the midplane temperature itself. In regions of negative values (blue and green color), the radiative temperature is lower than the adiabatic one; with positive values it is vice versa. One can clearly see both valleys. For a given surface temperature the midplane temperature is monotonically increasing in the surface densities (see Figure 3.2). So all "jumps" in Figure 3.6 are due to changes in the larger temperature, most of them because of changes in the mean molecular weight or adiabatic coefficient. One also notes that, except for the part of the "valleys" discussed above, the difference between adiabatic and radiative midplane temperature is only a few percent in the region where the disk turns from optically thick to thin and then to isothermal (black line in the figure, see also Section 3.3.2).

3.2.1 Density Approximation

We go back to Equation (3.15) and now use the approximation made in the last part there. Using the equation of state we can now calculate directly the gas density at the surface or photospheric density:

$$\rho_{\mathrm{s}} = \frac{\tau_{\mathrm{s}} \Omega^2 H_{\mathrm{s}}}{\frac{k_{\mathrm{B}}}{\mu} T_{\mathrm{s}} \kappa_{\mathrm{s}}} = \frac{\tau_{\mathrm{s}} H_{\mathrm{s}}}{H_{\mathrm{iso,s}}^2 \kappa_{\mathrm{s}}}. \tag{3.43}$$

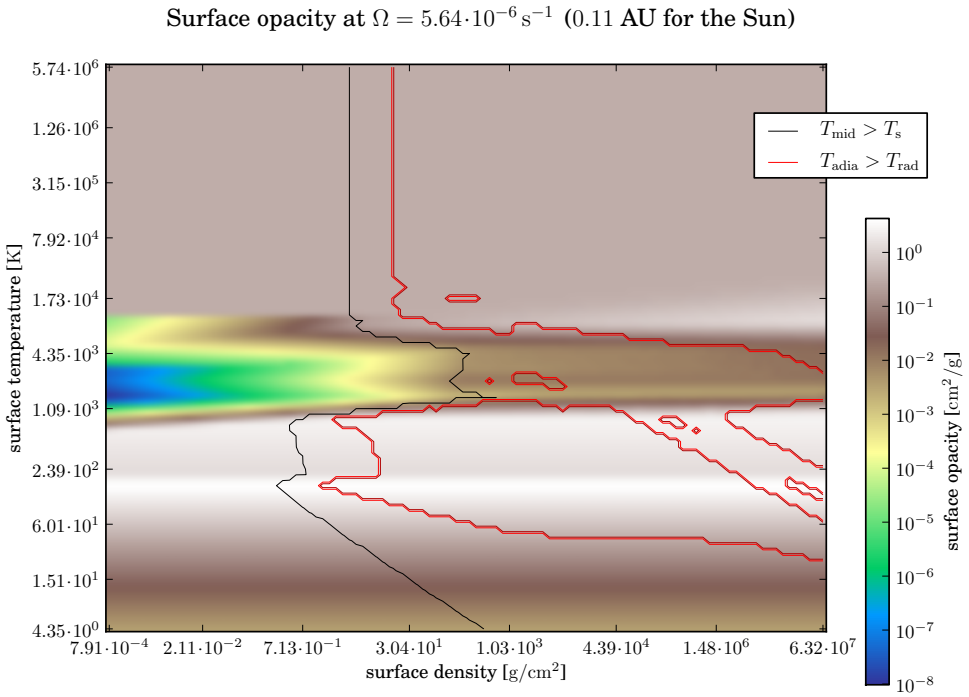

Figure 3.5 Surface opacity at 0.11 AU of a solar-mass star for different surface densities and temperatures.

This density is independent of the state of the disc below which makes the process of calculating the temperature much faster.

Yet one should be careful, because using the equation above and inserting it into Equation (3.16) yields:

$$1 = \sqrt{\frac{\pi}{2}} \frac{H_{\mathrm{s}}}{H_{\mathrm{iso}}} e^{H_{\mathrm{s}}^2/2H_{\mathrm{iso}}^2} \left(1 - \mathrm{erf}\left(\frac{H_{\mathrm{s}}}{\sqrt{2}H_{\mathrm{iso}}}\right)\right). \tag{3.44}$$

After some further arithmetic's we get

$$1 = \sqrt{\frac{\pi}{2}} x e^{x^2/2} \left(1 - \mathrm{erf}\left(\frac{1}{\sqrt{2}}x\right)\right). \tag{3.45}$$

which only solves for $x \to \infty$. So one cannot include it to get the surface height directly.

We will instead use Equation (3.33) of the surface density in the convective regime and will use it there:

$$\Sigma \frac{H_{\mathrm{iso}}^2 \kappa_{\mathrm{s}}}{2\tau_{\mathrm{s}}} = H_{\mathrm{s}} e^{H_{\mathrm{s}}^2/2H_{\mathrm{iso}}^2} I_{\Sigma,1} + H_{\mathrm{s}} \left(1 - \left(\frac{H_{\mathrm{s}}}{H_{\mathrm{A}}}\right)^2\right)^{\frac{-1}{\gamma-1}} I_{\Sigma,2}. \tag{3.46}$$

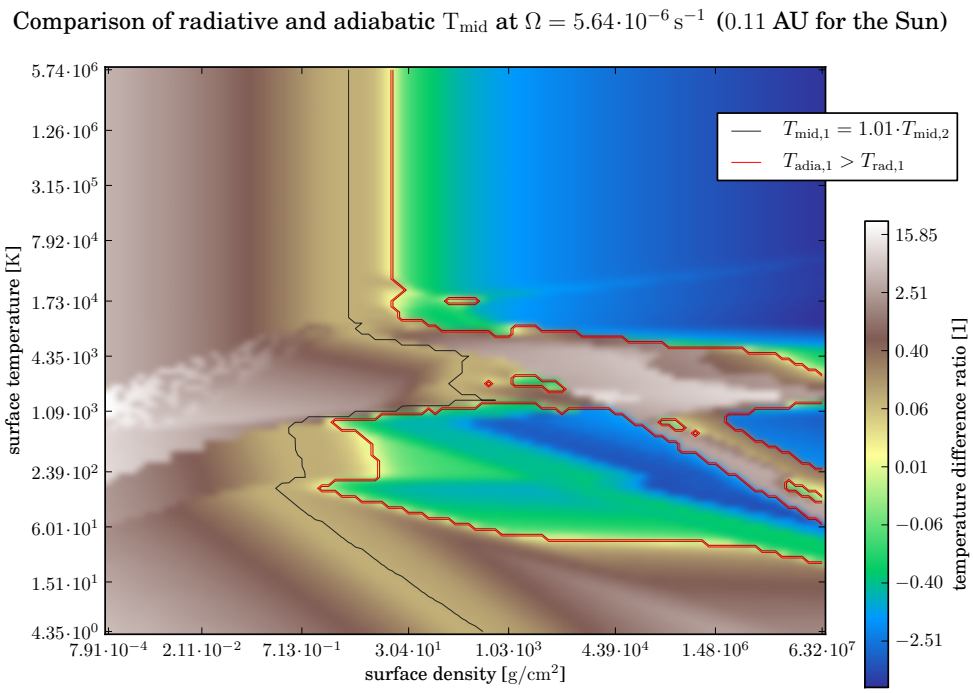

Figure 3.6 Comparison of the radiative and adiabatic midplane temperatures at 0.11 AU of a solar-mass star for different surface densities and temperatures. Colors of green and blue show regimes were the radiative transport dominates. Brown and grey colors show regions were convection is present.

Using Equation (3.28) we get

$$\Sigma \frac{H_{\rm iso}^2 \kappa_{\rm s}}{2\tau_{\rm s}} = H_{\rm s} e^{H_{\rm s}^2/2H_{\rm iso}^2} I_{\Sigma,1} + H_{\rm s} \left(1 - \frac{H_{\rm s}^2}{\frac{2\gamma}{\gamma-1} H_{\rm iso}^2 + H_{\rm s}^2}\right)^{\frac{-1}{\gamma-1}} I_{\Sigma,2}. \tag{3.47}$$

This is final equations we have to solve to get $H_{\rm s}$. In Appendix A we present the numerical steps in which we apply these sets of equations.

For the radiative part we have to assume the density profile we used in Equation (3.33). But we are only interested in the midplane density. Since we already made one strong approximation we will also use

$$\rho_{0,\rm rad} = \frac{1}{2.6} \frac{\Sigma}{\Omega} \tag{3.48}$$

as an estimation of the midplane density. If we use the Gaussian profile of the previous section and integrate it from zero to infinity, one finds a factor of $\sqrt{2\pi} \approx 2.6$, which assumes that all the gas is below the surface, which is mostly true. With Equations (3.48) and (3.36) we can also calculate a radiative midplane temperature.

3.2.2 Model version

While we use tabulated values for the FTM, the ATM allows on the fly temperature calculation for the evolution code. In general, the midplane temperature is independent of the initial temperature, yet for certain ranges of the surface density it gives different midplane temperatures depending on the previous/initial midplane temperature. For low midplane temperatures we get a lower midplane temperature than for high temperatures. This is due to strong dependencies of one or more parameters (e.g. opacity or adiabatic coefficient) on temperature. To illustrate this, we calculate the midplane temperature using the ATM for a range of different initial midplane temperatures and led the code converge to a new midplane temperature. We assume a sun like host star as the irradiating source and set the viscous $\alpha = 0.007$.

Figure 3.7 show this behavior for the full ATM model, while Figure 3.8 shows it for the ATM model with a fixed opacity. In both figures each diagonal line starts at the left at the initial midplane temperature and ends at the from that one calculated. The surface density for each converging midplane temperature does not change and is marked by the right end of the line in the figure.

Figure 3.7 shows the degeneracy of the midplane temperature at ≈ 0.084 AU. For a surface density between 28000 g/cm^2 and 34000 g/cm^2 there are two levels of temperatures to which the midplane temperature converges. A low one around 3000 K with a slightly increasing with surface density and a second one at 9000 K. One also sees a diverging temperature level that separates these to regions between 5000 K and 7000 K. These temperature values are comparable to the study from Bell and Lin (1994) of FU Orionis outbursts. Here the reason is a rapid change in opacity over a short temperature interval. A small increase in temperature increase the opacity strongly, which leads to a larger temperature that is leveling the opacity on the higher value. While the temperature values are comparable to Bell and Lin (1994), they occur at smaller

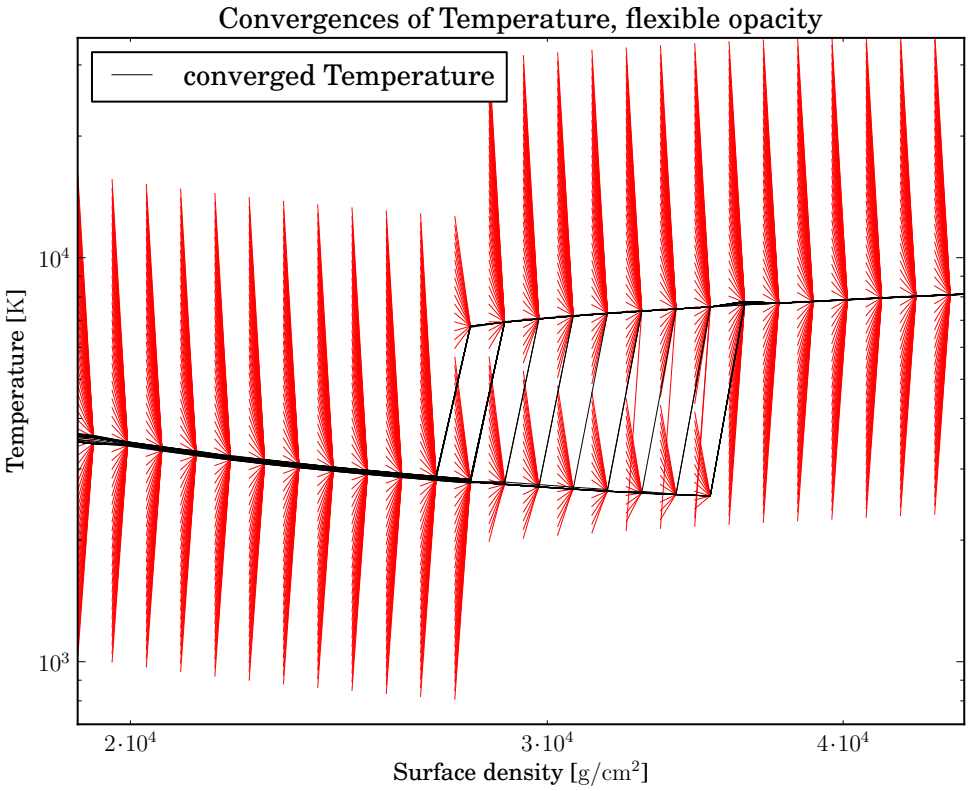

Figure 3.7 Convergence structure of midplane temperature for the ATM with flexible opacity at 0.084 AU. Red lines show the initial (left end) and final (right end) midplane temperature at different surface densities. For each line the surface density is constant and shown by the right endpoint of each line. Black line shows the converged temperature profiles.

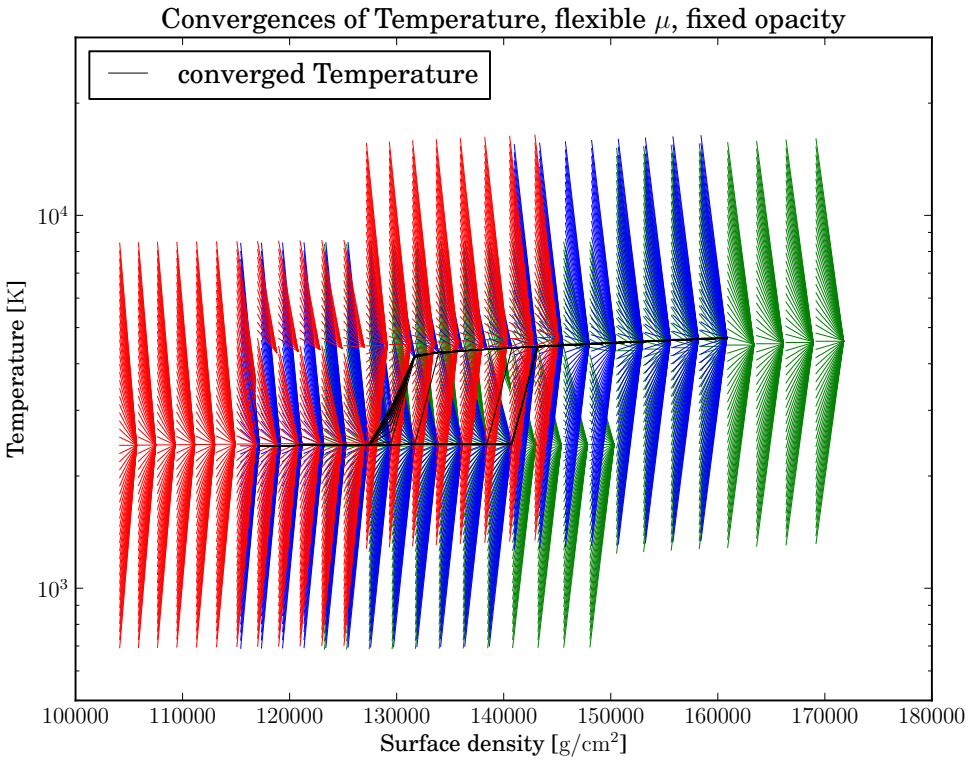

Figure 3.8 Convergence structure of midplane temperature for the ATM with fixed opacity at 3 different semimajor axis (red at 0.07 AU, blue at 0.4 AU and green at 2.2 AU) Diagonal lines show the initial (left end) and final (right end) midplane temperature at different surface densities. For each line the surface density is constant and shown by the right endpoint of each line. Black line shows the converged temperature profiles at 0.4 AU.

surface densities (viscous $\alpha = 0.007$). This difference can be explained because we have irradiation from a host star, which leads to larger temperatures for smaller surface densities than in the work of Bell and Lin (1994).

Yet not only changes in opacity can lead to a degeneracy of the midplane temperature. Figure 3.8 shows the convergence structure at 3 different semimajor axes. Here the opacity is fixed, but the mean molecular weight and the adiabatic coefficient is still flexible and calculate out of the EOS. For each semimajor axis shown, there is a range of surface density where we see a jump in midplane temperature. A "jump" in mean molecular weight, due to the ionization of the gas, leads to an rapid increase in midplane temperature. So if one starts with the lower mean molecular weight, due to an already large temperature, one gets a larger midplane temperature than for the low initial temperature and higher mean molecular weight.

Finally, to see how valid the approximation at the beginning of the section was, we show in Figure 3.9 the ratio of the approximated density of Equation (3.43) to the density calculated with the full model. Since the radiative surface height of the full model is zero for small surface densities, the approximated density is zero and

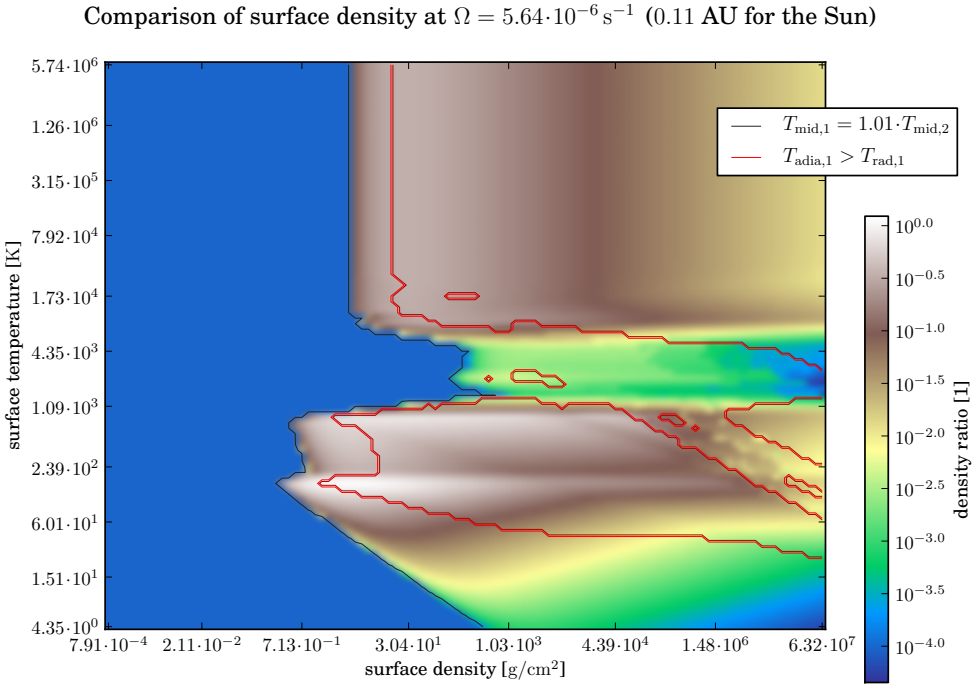

Figure 3.9 Comparison of photospheric densities at the radiative disk surface at 0.11 AU of a solar-mass star for different surface densities and temperatures. We plot the ratio of the approximated density over the FTM one.

therefore the ratio is also zero. For the rest of the covered range the approximated density is always lower than the FTM ones. Where the vertical energy transport is radiative, the estimate is closer than in regions of convection. This is due to the amount of gas above the surface being larger in the adiabatic case. The approximation itself can be seen as an assumed drop of the density to zero right at the surface. Therefore the larger amount of gas above the surface leads to larger errors in the approximation. So overall, for the radiative case and surface densities below a few $1000\,\mathrm{g/cm^2}$, the approximation is relatively accurate.

3.3 Comparison

In this section we show first the comparison of the ATM and FTM with the old temperature model for two different surface density profiles out of the disk evolution shown in Mordasini et al. (2012a) Figure B.1r. In the second part, we highlight the different versions to calculate the effective optical depth in the literature.

3.3.1 Old and new model

We took the two profiles shown in Figure 3.11 and calculated the temperature using both our models. Both of them are surface density profiles shown in Mordasini et al. (2012a) Figure B.1r.

The result is shown in the left penal of Figure 3.10. For both profiles the disk is radiative in the inner part and adiabatic in the outer part. ATM and FTM gives almost the same profile, even with the sometimes large discrepancies in photospheric density shown in the section above. They do deviate a bit only for temperatures below a few 10 K. The underestimation in photospheric density puts more mass below the surface and this increases the midplane temperature. Comparing the old temperature model with the new one, we see that the maximal difference is around a factor 2. Also the shape of the profile is similar. Yet for temperatures above 1000 K the new model temperatures are colder, while below 1000 K the new model gives larger temperatures. The reason why the temperature is different is the different optical depth. It is either too large in my model, which is the case when the opacity decreases monotone from the midplane to the surface in the old vertically integrated model when the temperature is below 1000 K. Or the optical depth in the new model is too small. This is the case when there is a sufficiently large maximum in opacity between the midplane and the surface. We estimate the optical depth using only the midplane temperature and density (see Equation (3.37)). Yet with strong variations in opacity this estimate will be more or less wrong.

The right panel compares the midplane pressure between the old and the new models for the same two surface density profiles. Here the differences are of the same order as for the temperatures, at least inside of 50 AU. The old model tables only extended out to 30 AU, further out a extrapolation was used with also resulted in the bump of temperature and pressure outside of 50 AU. Therefore, the pressure in the old model and the new one should not be compared where that bump occurs.

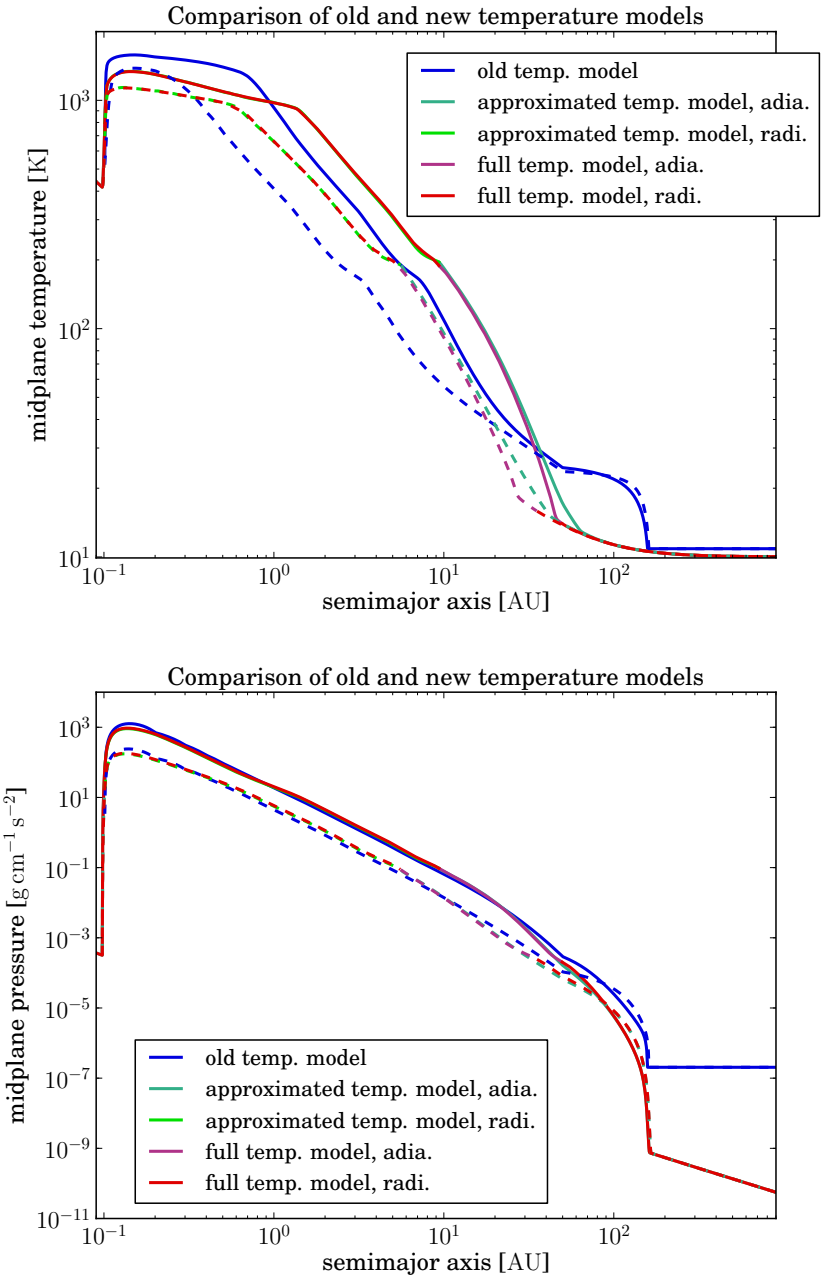

Figure 3.10 *Upper panel*: Comparison of midplane temperature for 3 different temperature models and 2 different surface density profiles. *Lower panel*: Comparison of the midplane pressure for 3 different temperature models and 2 different surface density profiles. Blue shows the old temperature model, Green colors shows the approximated temperature model and red the full temperature model. The slightly blueish green and red colors illustrate the part where the disk is adiabatic and the full red and green color the part where the disk is radiative. Solid lines show the profiles for the larger surface density profile and dashed lines for the smaller profile show in Figure 3.11.

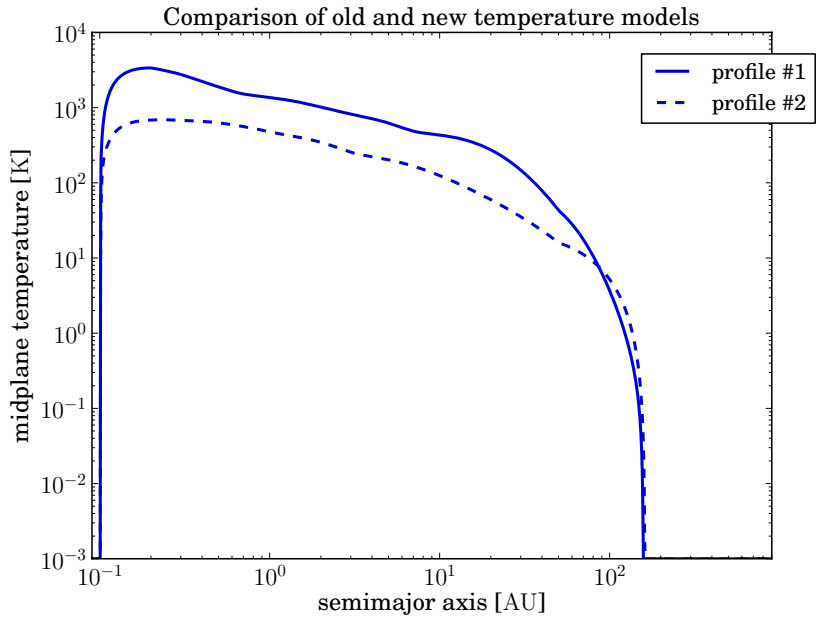

Figure 3.11 Surface density profiles used to calculate the midplane temperatures in Figure 3.10

3.3.2 Optical depth

Finally, we want to remark that there are a few sligthly different versions of Equation (3.37). While we use the version stated above, we calculated the midplane temperature also using the version of Hubeny (1990):

$$\tau_{\text{eff}} = \left(\frac{3}{8}\tau_{\text{R}} + \frac{\sqrt{3}}{4} + \frac{1}{2\tau_{\text{P}}} \right). \tag{3.49}$$

Both equations are similar except for the factor of $\sqrt{3}/4$ instead of 1. The difference in the resulting midplane temperatures are shown in Figure 3.12. For all surface temperatures and densities the FTM temperature is always warmer than the one calculated with Hubenys equation. There are only larger differences of up to 24% in the region where the disk turns vertically isothermal for small surface densities. This is the region where the changes from optically thick to optically thin occurs and therefore the optical depth becomes of the order of unity. Here the difference between between the two equations becomes the largest. This results in a drop of the radiative midplane temperature below the adiabatic one in that region. As discussed before, in the FTM the difference between radiative and adiabatic midplane temperature is small in that part. Thus a change in the effective optical depth by a factor of two can reduce the radiative temperature below the adiabatic one. Already such a minor change in the equation of the effective optical depth can hence affect whether the model predicts that the disk is adiabatic or radiative. Updated opacity tables, especially changes in the gas opacities (Malygin et al., 2014), in a future work will probably alter the temperature profile of the disk in a similar or even more severely.

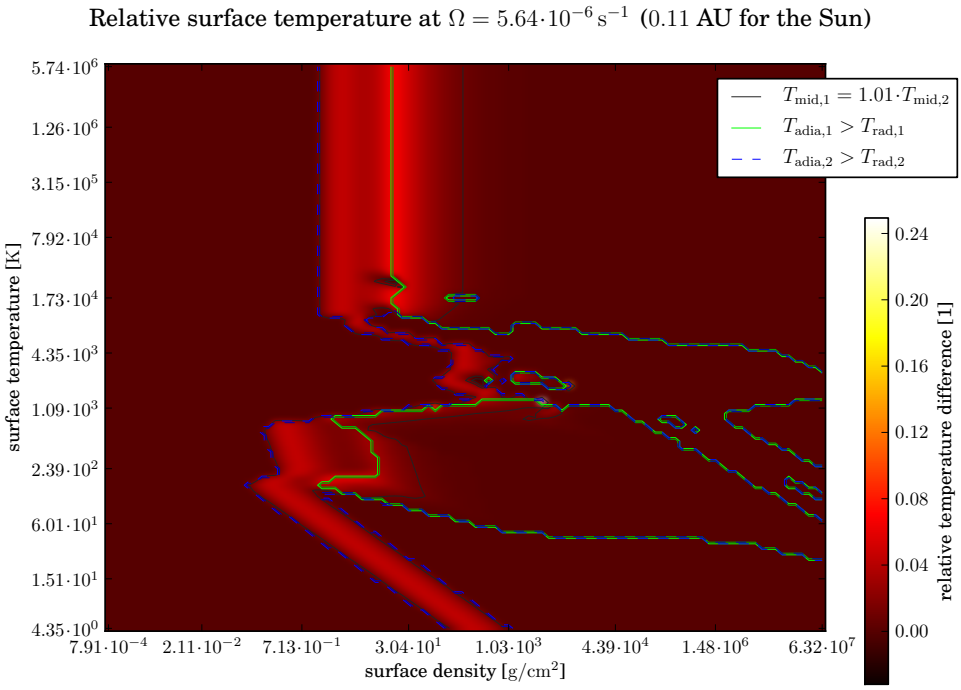

Figure 3.12 Comparison of the midplane temperature of the FTM (marked with an one as asterisk) and midplane temperatures calculated with the effective optical depth of Hubeny (1990) (marked with an two as asterisk). The fine black line marks the level where the temperatures deviate by a factor of 1.01. Green solid line illustrates the border between adiabatic and radiative regions for the FTM model. Blue dashed line marks the same border in the Hubeny case.

Chapter 4

Disc model

Presented in the first part of this chapter are the different parts of the protoplanetary disc model, before some results are shown. For parts we first discuss the solver itself, then the inner edge, the photo evaporation, the formation of the disk and initial setup. As for the results we first show two single disc simulations before talking about a small set of initial conditions and compare different infall models.

4.1 The solver

The aim of the disc model is to quickly simulate the evolution of a protoplanetary disc for many different initial conditions. Such that it can be used for planet population synthesis calculations as presented in Chapter 2. We choose a similar setup as in the old model, a vertically integrated, rotational symmetric gaseous disc. To describe the gas profile, we use the integrated gas surface density Σ. The evolution of the surface density as a function of time t and distance from the star a is obtained by solving the diffusion equation with an effective viscosity ν.

$$\frac{\partial}{\partial t}\Sigma = \frac{3}{a}\frac{\partial}{\partial a}\sqrt{a}\frac{\partial}{\partial a}\nu\Sigma\sqrt{a} - \frac{2}{a}\frac{\partial}{\partial a}\frac{\dot{h}\Sigma}{\Omega} + \dot{Q}_w = \frac{4.5}{a}\frac{\partial}{\partial a}\nu\Sigma + 3\frac{\partial^2}{\partial a^2}\nu\Sigma - \frac{2}{a}\frac{\partial}{\partial a}\frac{\dot{h}\Sigma}{\Omega} + \dot{Q}_w \quad (4.1)$$

The first part of the right hand side of that equation is the typical diffusion equation for the surface density. The middle part contains the exchange of angular momentum $\dot{h}$ with a planet immersed in the disk. While we do not include any planet in the simulations done in this work, the solver itself has the option included to study type II migration. The last quantity on the right hand side $\dot{Q}_w$ is a source or sink term. It contains photo-evaporation, accretion onto a planet and infall of the gas at the disk formation stage. In the derivation of Equation (4.1) it was already assumed that the disc is Keplerian everywhere:

$$\Omega = \sqrt{\frac{GM_{\text{star}}}{a^3}} \quad (4.2)$$

As an effective viscosity, we use the α prescription of Shakura and Sunyaev (1973).

$$\nu = \alpha \frac{c_s^2}{\Omega} \tag{4.3}$$

Normally, α will be constant but the solver also allows it to vary. We will use this to incorporate gravitational turbulent alpha prescriptions from Kratter et al. (2008) (see Section 4.4). Substituting the soundspeed c_s gives:

$$\nu = \alpha \frac{k_B T_{mid}}{\mu \Omega} \tag{4.4}$$

with T_{mid} being the midplane temperature. This temperature is given by one of the temperature models described in the previous chapter.

4.1.1 Numercial setup

We use a Crank-Nicholson scheme to solve Equation (4.1) on a logarithmic grid, which is derived in Appendix B. For each individual timestep of length dt, the solver gets invoked twice with half the timestep. In between, the new midplane temperature gets calculated. At the end of each timestep we calculate the new host star mass, radius and temperature, a new inner truncation radius and, for some simulations, a new α-parameter profile. Finally, we calculate a new timestep depending on the change of the surface density over the last timestep.
Depending on the temperature model we use, it takes $0.2 - 0.3$sec with the ATM or around $0.01 - 0.02$sec with the tabulated FTM to compute one timestep. We did a few simulations with the FTM in an "on the fly mode" but here timesteps used $2 - 3$sec of real time. Our computational domain goes from 0.003AU to 30,000AU with 2800 grid cells, which results in 400 grid cells per decade.

4.1.2 Smoothing

To speed up the computation, we can use three different smoothing routines while calculating the temperature. All routines smooth over a certain number of grid cells SL.

Routine 1:

$$X_i = \sum_{j=i-SL}^{i+SL} \frac{\hat{X}_j}{2SL+1} \tag{4.5}$$

Routine 2 (logtri):

$$X_i = \exp\left(\frac{\sum_{j=i-SL}^{i+SL} (SL+1-|j-i|) \log(\hat{X}_j)}{\sum_{j=i-SL}^{i+SL} (SL+1-|j-i|)} \right) \tag{4.6}$$

Routine 3 (tri):

$$X_i = \frac{\sum_{j=i-SL}^{i+SL} (SL+1-|j-i|) \hat{X}_j}{\sum_{j=i-SL}^{i+SL} (SL+1-|j-i|)} \tag{4.7}$$

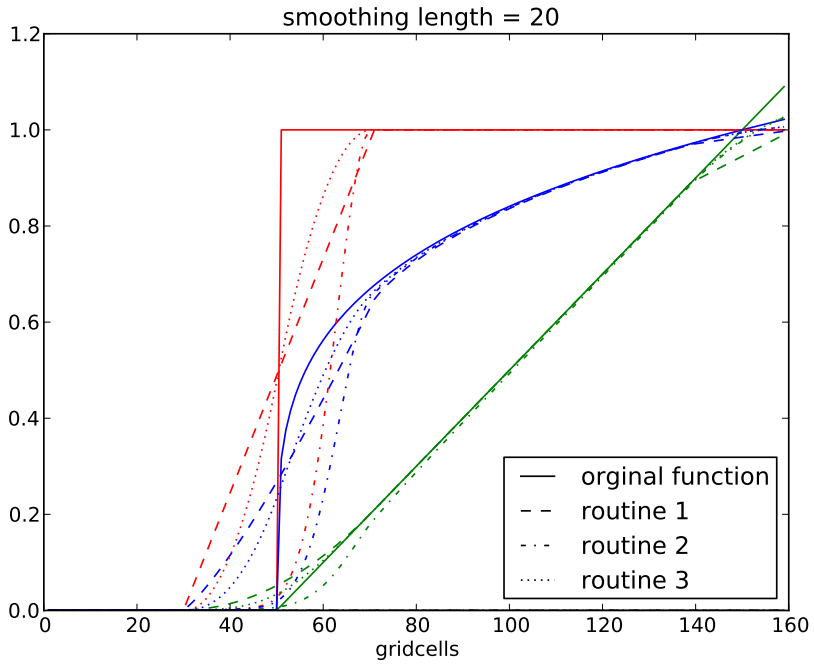

Figure 4.1 Smoothing of 3 different functions: The red functions is a simple step function. The green function is a linear slope. The blue function is a 4th order root.

All three smoothing routines are illustrated in Figure 4.1

For most of our simulations, we use routine 3 with $SL = max(5, gc(H))$ and $gc(H)$ being the number of grid cells for the isothermal disc height or pressure scale height H. We can smooth over a pressure scale height because turbulence will lead to an exchange of heat over at least that range, smoothing out the temperature peaks. The first two routine do not give as good results and speedups.

4.2 Edge

Our disks are truncated at the inner part. We force the surface density inside of the inner disk edge to be of a predefined minimal value and add the mass in that region onto the star at each timestep. To determine the position of this inner edge, we follow the simple model of Chang et al. (2010) and Starczewski et al. (2007). They consider a balance of the stellar magnetic dipole pressure and the ram accretion pressure to calculate the location of an inner truncation radius of the disc. The gas will then flow along the streamlines of the magnetic field from this radius onto the star.

$$a_{\text{trunc}} = \sqrt[7]{\frac{9(B_{\text{star}}R_{\text{star}}^3)^4}{4GM_{\text{star}}\dot{M}^2}} \tag{4.8}$$

As can be seen, it depends on the stellar radius, the accretion rate onto the star and the stellar magnetic field. Changes in the stellar radius during the evolution of the

star have the strongest effects on the position of the inner edge. Also, the accretion rate itself, which depends next to other things on the effective temperature of the star, is important. So it will depend on the choice of the stellar evolution model, which is discussed in Section 4.6. E.g., an increase in the stellar radius will push the inner edge farther away from the star. Since the accretion flow decreases during the evolution of the disk the inner radius of the disk gets pushed out. For small accretion flows of less than $10^{-10}M_{\odot}/yrs$, it can be of the order of 1AU or larger. Since this is also the radius at which the inner photoevaporation sets in (see Section 4.3), we limit the inner truncation radius to be always smaller than 1AU.

The most difficult quantity to specify is the stellar magnetic field. Generated by convection inside the rotating stars, it is not easy to estimate in our simple model. The reason is that the evolution of the rotation frequency of the star is not well understood (Pudritz and Matt, 2014). Armitage and Clarke (1996) presented a model to estimate the rotation frequency using the disk lockout model. Here, a torque from the magnetic dipole field of the star acting on the disk is slowing the star down. Yet as was pointed out the dipole field of the star is too weak in the regions of the disk where the angular momentum slowing down the star is generated (Johns-Krull et al., 1999). Furthermore, observations show that there is no correlation between the rotation rate of a star and the presence of indicators of a disk (Cieza and Baliber, 2006).

Therefore, we use a constant magnetic field of $B_{\text{star}} = 1kT$ for all our simulations and do not follow the evolution of the rotation frequency of the star.

4.3 Disk mass loss and photoevaporation

The evolution of a protoplanetary disk is not only determined by the value of the viscous α. There are a number of processes that also alter the surface density of the disk by removing gas from the system temporarily or permanently. E.g., magnetic winds seem to lift mass from the surface of the disk and let it fall down back farther out or even remove it completely from the system. Also, flybys of neighboring stars can remove mass from the outer disk regions and truncate the outer disk due to tidal interactions (Adams et al., 2006; Gutermuth et al., 2005). Yet, a recent study (Megeath et al., 2015) shows that, at least in the Orion molecular clouds, most disks are too distant from other stars that truncation could be a common mechanism for mass removal. The same study also showed that also photoevaporation due to UV irradiation from OB stars is too weak for most disk to be a significant factor.

Nevertheless, in this study we include 2 processes that remove mass permanently from the system, namely the photoevaporation due to extreme UV irradiation from the host star ($h\nu > 13.6\,\text{eV}$) and far UV irradiation ($6\,\text{eV} - 13.6\,\text{eV}$) from OB stars in the vicinity. The first process is intrinsic to being close to the host star and should be common. We use the second one as a general tool to alter the evolution time of a disk and the mass loss rate is one of our initial condition parameters. In that sense, it subsume all the different processes that will not lead to accretion of mass onto the host star. The general idea of photoevaporation is the absorption of high energy photons by hydrogen atoms which heat them up so that the sound speed becomes larger than

the escape velocity. Therefore the atom can leave the gravity well of the host star and escapes the system.

4.3.1 Internal photoevaporation

Our first source of photoevaporation is extreme UV irradiation from the host star itself. We use the version of the previous disc model (Mordasini et al., 2012a) which follows closely Clarke et al. (2001). It gives us a surface density loss rate of

$$\dot{\Sigma}_{\mathrm{w}} = \begin{cases} -c_{\mathrm{s,inph}} m_{\mathrm{H}} \left(\frac{a}{R_{\mathrm{ph,in}}}\right)^{-5/2} 11.4{\cdot}10^4 \Phi_{41}^{1/2} \left(\frac{R_{\mathrm{ph,in}}}{10^{14} cm}\right)^{-3/2} cm^{-3} & \text{if } a > R_{\mathrm{ph,in}}\,, \\ 0 & \text{otherwise} \end{cases} \tag{4.9}$$

The UV irradiation is assumed to evaporate gas only outside the gravitational bonding radius

$$R_{\mathrm{ph,in}} = 0.15 \frac{G M_{\mathrm{star}}}{c_{\mathrm{s,inph}}^2}. \tag{4.10}$$

Here $c_{\mathrm{s,inph}} = 10^6\,\mathrm{cm/s}$ is the sound speed of the photo-ionized gas which is set to , Φ_{41} the number of ionizing photons in units of $10^{41}\,s^{-1}$ (fixed to 1 in all our simulations) and m_{H} is the mass of a hydrogen atom. When the surface density gets low enough, this can open a gap in the disc. Also, in private correspondence with Christoph Mordasini, Ilaria Pascucci stated that gas will already be lost even if the sound speed only reaches a fraction of 0.15 of the escape velocity. We use this factor also for the external photoevaporation. With this factor, a typical distance for internal photoevaporation to begin is around 1 AU.

4.3.2 External photoevaporation

For the external photoevaporation of OB star irradiation we also use the version of the previous disc model described in Mordasini et al. (2012a) .

It gives a surface density loss rate as

$$\dot{\Sigma}_{\mathrm{w}} = \begin{cases} \frac{M_{\mathrm{wind}}}{\pi (R_{\mathrm{nmax}}^2 - R_{\mathrm{ph,ext}}^2)} \left(1 - \frac{1}{1+(a/R_{\mathrm{ph,ext}})^{20}}\right) & \text{if } a > R_{\mathrm{ph,ext}}\,, \\ 0 & \text{otherwise} \end{cases} \tag{4.11}$$

Here, M_{wind} is a free input parameter, one of the initial conditions, which sets the strength of the irradiation. The outer radius R_{nmax} of the computational domain is 30000 AU for all our simulations, as stated before.

Similar to Equation (4.10) above the gravitational bonding radius is

$$R_{\mathrm{ph,ext}} = 0.15 \frac{G M_{\mathrm{star}}}{c_{\mathrm{s,extph}}^2}. \tag{4.12}$$

with $c_{s,extph}$ the sound speed at 1000 K. The second factor

$$\left(1 - \frac{1}{1 + (a/R_{ph,ext})^{20}}\right) \tag{4.13}$$

in Equation (4.11) is a smoothing at the inner edge of the photoevaporation region to speed up the calculation.

With an outer radius R_{nmax} of 30000 AU, the surface density loss rate depends only very weakly on the host star mass through $R_{ph,ext}$. So one can directly translate a given M_{wind} into $\dot{\Sigma}_w$ by

$$\dot{\Sigma}_w[\mathrm{g\,cm^{-2}\,s^{-1}}] \approx 3.11{\cdot}10^{-10}\mathrm{M}_{wind}[\mathrm{M}_\odot/\mathrm{yr}]. \tag{4.14}$$

While we said before, that M_{wind} to alternate the lifetime of a disk, it also has a strong influence on the size of our disk. The mass loss from the outer disk will be balanced by the outspreading mass flow from the disk which is mostly determined by the viscous α. These two processes determine where the outer radius of a disk is. Finally, during the infall phase we reduce M_{wind} by the square of the ratio of the already collapsed mass to the total cloud mass. The idea is that the infalling cloud shield the disk from the irradiation at first but with vanishing mass some already hits the disk.

4.4 Gravoturbulent viscous alpha

For some combination of initial conditions the disk will be massive enough the become grava-turbulent in the outer regions. To calculate the viscous *alpha* in these regions we use the model of Kratter et al. (2008) . They divide α_{GI} into two components a short ranged one and a long ranged one covering different ranges of the Toomre parameter

$$Q = \frac{c_s \Omega}{\pi G \Sigma}, \tag{4.15}$$

where c_s is the soundspeed and Σ the surface density of the disk, Ω the Keplerian frequency and G the gravitational constant. And like them, we limit Q to never be lower than 1 in the calculations of α_{GI}. So

$$\alpha_{GI} = \left(\alpha^2_{short} + \alpha^2_{long}\right) \tag{4.16}$$

where

$$\alpha^2_{short} = \max\left[0.14\left(\frac{1.3^2}{Q^2} - 1\right)(1 - \mu_{GI})^{1.15}, 0\right] \tag{4.17}$$

and

$$\alpha^2_{long} = \max\left[\frac{0.14{\cdot}10^{-3}(2 - Q)}{\mu^{5/4}_{GI} Q^{1/2}}, 0\right]. \tag{4.18}$$

In both equations $\mu_{GI} = M_{disk}/(M_{star} + M_{disk})$ is the mass fraction of the disk. Finally, we use

$$\alpha = \max(\alpha_{GI}, \alpha_{min}) \tag{4.19}$$

with α_{min} being a free input parameter.

4.5 Disc Formation

We will use 2 different infall models to simulate the formation of the star-disk system. Both assume a spherical cloud of isothermal gas that is undergoing gravitational collapse. In the first model, called a singular isothermal sphere or Shu model, the cloud has a r^{-2} density profile, giving each mass-shell the same mass. The second model has a more realistic density profile of a Bonnor-Ebert sphere.

4.5.1 Infall of Singular Isothermal Sphere

Shu (1977) presented the calculations on the infall of an isothermal sphere with an r^{-2} density profile. While this profile has an infinite density in the center and is therefore called singular isothermal sphere (SIS), it leads to a simple infall model: each shell at radius $R_s = f_{sis} c_s t/2$ has a constant mass, which collapses onto the star-disc system, which is formed by the gas that already collapsed from inside ofR_s, after free fall time $t = t_{ff}$. This leads to an inside out collapse. Since the free fall time is proportional to the radius R_s, the infall rate

$$\dot{M} = f_{sis} c_s^3 / G \tag{4.20}$$

of a singular isothermal sphere is constant over time (Shu, 1977). The scaling factor $f_{sis} = 0.975$ and the maximal semimajor axis a_c (also called centrifugal radius) at which mass from shell at R_s hits the midplane of the star-disc system is

$$a_c(t) = \frac{\Omega_{cl}^2 R_s(t)^4}{G(M_{disk} + M_{star})} = 1/16 f_{sis}^3 c_s \Omega_{cl}^2 t^3 \tag{4.21}$$

With these equations we can now calculate the source term profile for the infall (Birnstiel et al., 2010). To compute the position where one infalling gas blob land on the disk, we assume angular momentum conservation on the way from the cloud to the disk. This leads to

$$Q_w(a,t) = \frac{\dot{M}}{4\pi a \sqrt{a_c(t)(a_c(t) - a)}} \tag{4.22}$$

This equation in not only valid for the SIS infall but for all spherically symmetric infalling density structures if on assumes a razor thin disk. In reality, the infalling gas will hit the disk at a certain height and farther out than is assumed in the derivation of the equation above. At that point the angular momentum of the infalling gas and the gas of the disk are not the same. The infalling gas will gain some angular momentum from the disk and end up further out than predicted by the equation above. The same exchange of angular momentum will increase the mass flow of the disk gas inward (see Visser et al., 2009). We will neglect these effects in this study and simply add gas according to the Equation (4.22). The set of equations depends on the initial state of the infalling cloud, which is defined by the three quantities cloud mass M_{cl}, the cloud temperature T_{cl} and could solid rotation frequency Ω_{cl}. Specifying these, the minimal α, and the photoevaporation rate through M_{wind} defines the star-disc system. The set of initial conditions we will study in detail in Chapter 5.

4.5.2 Infall of Bonner-Ebert-Sphere

Myers (2005) presented a way to calculate the infall rate of a spherical density structure with a Bonnor-Ebert-Sphere (BES, hereafter) density profle. This profile has no infinite density at the center. It also follows an inside out collapse, which the gas close to the center collapsing before the gas further out. To calculate the source term (Equation (4.22)), we need to specify the infall rate $\dot{M}(t)$ and the centrifugal radius $a_c(t)$. We use an analytic function of the density profile of a BES to get an analytic expression of the infall factor $f_{\mathrm{BES}}(t)$. We assume, that the density profile can be expressed by

$$\rho = \rho_c \left(1 + \left(\frac{\xi}{f_a}\right)^2\right)^{-f_b} \tag{4.23}$$

with

$$\xi = R/R_0 = R\sqrt{4\pi G\rho_c}/c_s \tag{4.24}$$

Here R_0 is the scale length, f_a and f_b fitting parameters specific for the BES. The mass between ξ and $\xi + d\xi$ can be expressed as

$$dm = 4\pi\rho(\xi)R_0^3\xi^2 d\xi \tag{4.25}$$

We can further calculate the time when that shell collapses

$$t = t_{\mathrm{ff,BES}}\sqrt{\xi/(x\phi')} \tag{4.26}$$

with

$$\phi \equiv -ln(\rho/\rho_c) = f_b \log\left(1 + \left(\frac{\xi}{f_a}\right)^2\right) \tag{4.27}$$

and

$$\phi' \equiv \frac{d\phi}{d\xi} = \frac{2f_b}{f_a^2}\frac{\xi}{1 + \left(\frac{\xi}{f_a}\right)^2}. \tag{4.28}$$

This leads to

$$t = t_{\mathrm{ff,BES}}\sqrt{\frac{f_a^2}{6f_b}\left(1 + \left(\frac{\xi}{f_a}\right)^2\right)} \tag{4.29}$$

with

$$t_{\mathrm{ff,BES}} = \sqrt{\frac{3\pi}{32G\rho_c}} \tag{4.30}$$

Equivalently, this gives the radius of the shell which collapses at time t:

$$\xi = R_s(t)/R_0 = f_a\sqrt{\frac{t^2}{t_{\mathrm{ff,BES}}^2}\frac{6f_b}{f_a^2} - 1} \tag{4.31}$$

Taking the derivative of Equation (4.29)

$$\frac{dt}{d\xi} = t_{\mathrm{ff,BES}}\frac{\xi}{f_a\sqrt{6f_b\left(1 + \left(\frac{\xi}{f_a}\right)^2\right)}} \tag{4.32}$$

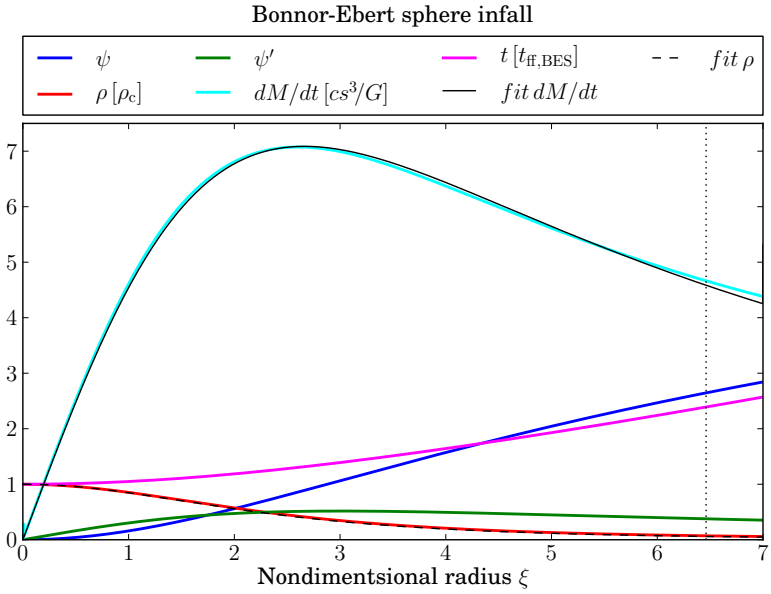

Figure 4.2 Density profile, infall rate, time for the collapse of a Bonnor-Ebert sphere

Finally, we can divide $dm/d\xi$ by Equation (4.32) to get the infall factor

$$f_{\mathrm{BES}}(t) = \frac{dm}{dt}\frac{G}{c_s^3} = f_a\sqrt{\frac{16f_b}{\pi^2}}\xi\left(1+\left(\frac{\xi}{f_a}\right)^2\right)^{0.5-f_b}. \tag{4.33}$$

We use the last equation to fit the numeric infall rate to obtain $f_a = 3.09624$ and $f_b = 1.6758$. The resulting fit is shown in Figure 4.2. It follows the numerically obtained rate nicely: the maximal deviation is 3% at 7ξ.

The centrifugal radius, or maximal radius at which mass falls onto the disc, as a function of time is

$$a_c(t) = \frac{\Omega_{cl}^2 R_s(t)^4}{G(M_{\mathrm{disk}}+M_{\mathrm{star}})} = \frac{c_s^4\Omega_{cl}^2}{G^3(M_{\mathrm{star}}+M_{\mathrm{disk}})\rho_c^2}\frac{f_a^4}{16\pi^2}\left(\frac{t^2}{t_{\mathrm{ff,BES}}^2}\frac{6f_b}{f_a^2}-1\right)^2. \tag{4.34}$$

With this we have the two equations to again calculate the source term profile Q_w. Yet to use the same set on initial conditions as for the Shu model, M_{cl}, T_{cl}, and Oc we have to calculate the central density ρ_c. So from the EOS we know that the external density

$$\rho_{\mathrm{ext}} = \frac{P_{\mathrm{ext}}}{c_{s,cl}^2}. \tag{4.35}$$

Stability analysis shows that a Bonnor-Ebert sphere will be become unstable when the external pressure reaches

$$P_{\mathrm{ext}} = P_{\mathrm{crit}} = 1.40\frac{c_{s,cl}^8}{G^3M_{cl}^2} \tag{4.36}$$

and the ratio of internal to external density becomes

$$\frac{\rho_c}{\rho_{\mathrm{ext}}} = 14.1. \tag{4.37}$$

Combining the three equations above leads to:

$$\rho_c = 1.40 \cdot 14.1 \frac{c_{s,cl}^6}{G^3 M_{cl}^2} \tag{4.38}$$

4.5.3 Initial set up

To set up the initial state of our simulation we need at least a small disk that can be evolved by the solver described above. So to get this initial disk and the star mass we consider the mass falling from the cloud onto the disk-star system without viscously evolving the "proto"disk. At this first stages gas will only fall onto the central star and later on gas will either fall onto the star or the disk if the centrifugal radius a_c is larger than the stellar radius R_{star}.

$$\dot{M}_{star} = \begin{cases} \dot{M}(t) & \text{if } R_{star} > a_c \text{ ,} \\ \dot{M}(t)(1 - \sqrt{1 - R_{star}/a_c}) & \text{otherwise} \end{cases} \tag{4.39}$$

and

$$\dot{M}_{disk} = \dot{M}(t) - \dot{M}_{star} \tag{4.40}$$

To finally get the mass of star and disk and while we not viscously evolve the disk itself we also consider mass accretion from the disk through the star disk interface (SDI) during this initial phase. We assume the interface is right at the star radius.

$$\dot{M}_{SDI} = -6\pi\sqrt{R_{star}} \frac{\partial}{\partial a} \nu \Sigma \sqrt{a} \tag{4.41}$$

We neglect viscous heating so the temperature at the star-disc interface is simply the effective stellar temperature T_{star} and the temperature slope $\beta_T = -3/4$. Therefore we can estimate the viscosity as

$$\nu = \frac{\alpha c_s^2}{\Omega} = \alpha \frac{k_B}{\mu_{gas} G M_{star}} T_{star} R_{star}^{3/4} a^{3/4}. \tag{4.42}$$

Finally we assume a fixed initial surface density slope $\beta_\Sigma = -1.3$. This gave us the fastest speed up of the simulation at the start. Also we put all the disk mass between the stellar radius and the centrifugal radius so with this we get

$$\Sigma_{SDI} = \frac{(2 + \beta_\Sigma) M_{disk} R_{star}^{\beta_\Sigma}}{2\pi (a_c^{\beta_\Sigma + 2} - R_{star}^{\beta_\Sigma + 2})} \tag{4.43}$$

Thus

$$\dot{M}_{SDI} = -6\pi R_{star}^{1.25 - \beta_\Sigma} \frac{\partial}{\partial a} \alpha \frac{k_B}{\mu_{gas} G M_{star}} T_{star} \Sigma_{SDI} a^{1.25 + \beta_\Sigma} \tag{4.44}$$

And placing the interface at the stellar surface gives

$$\dot{M}_{SDI} = -6\pi (1.25 + \beta_\Sigma) \alpha \frac{k_B}{\mu_{gas} G M_{star}} T_{star} \Sigma_{SDI} R_{star}^{1.5}. \tag{4.45}$$

Overall the lifetime and evolution did not depend on the initial value of β_Σ since the disk develops rapidly (a few 10 years) into a first stable state (See Section 4.7). Also m_{gas} is the mean molecular weight of the gas, which is also fixed in all our simulations (we use 26% helium and 74% hydrogen). We do not consider the temperature of the gas at this point to calculate changes in ν_{gas} for this initial phase.

So with these equation we sum up star mass and disk mass until none of the following conditions are fulfilled:

- $a_{\text{c}} < 6R_{\text{star}}$
- $M_{\text{disk}} < 10^{-3}\text{M}_\odot$
- $M_{\text{star}} < 0.025\text{M}_\odot$
- $M_{\text{star}} < \min(0.6M_{\text{cl}}, \text{M}_\odot)$ and $M_{\text{disk}} < 0.2M_{\text{star}}$

With these masses we finally set up out initial surface density profile:

$$\Sigma(a) = \frac{(2+\beta_\Sigma)M_{\text{disk}}R_{\text{star}}^{\beta_\Sigma}}{2\pi(a_{\text{c}}^{\beta_\Sigma+2} - R_{\text{star}}^{\beta_\Sigma+2})}\left(\frac{a}{R_{\text{star}}}\right)^{\beta_\Sigma} \tag{4.46}$$

All criteria above are set to get a stable initial state from which we can start to evolve the disk.

4.6 Stellar Evolution

Because we are using an infall model as described above we have a changing star mass. It increases by the gas falling onto the host star either through disk accretion or directly during the infall phase from the collapsing cloud. Furthermore, even a young pre-main-sequence star changes its temperature and radius during its evolution to the main sequence. Since stellar mass, temperature and radius are critical for the disc evolution and shape of the disk, we have to include stellar evolution into our model. Too keep it simple we will use the public pre-main-sequence star evolution tracks of Siess et al. (2000) to get for a given mass and age the effective temperature and radius of the star. The temperature will determine the thermal irradiation onto the disk and the radius will influence evolution of the inner edge of the disk (see Equation (4.8)). For some of our simulations we use a much smaller table of the evolution of only three different star masses found in Stahler and Palla (2005) (Table 16.2). Due to the small number of data points there will be kinks in the evolution of some quantities like the inner edge or stellar temperature. The most significant difference are larger effective star temperatures for stars more massive than one solar mass since the small table does not cover the change in the dependence of effective temperature and stellar mass above one solar mass. A comparison between both models will be shown at the end of this chapter. We note that Yorke and Bodenheimer (2008) showed that accretion will alter the evolution track of a star compared to the constant mass calculations in the used stellar models above, but use the tabulated evolution tracks for simplicity and computation time.

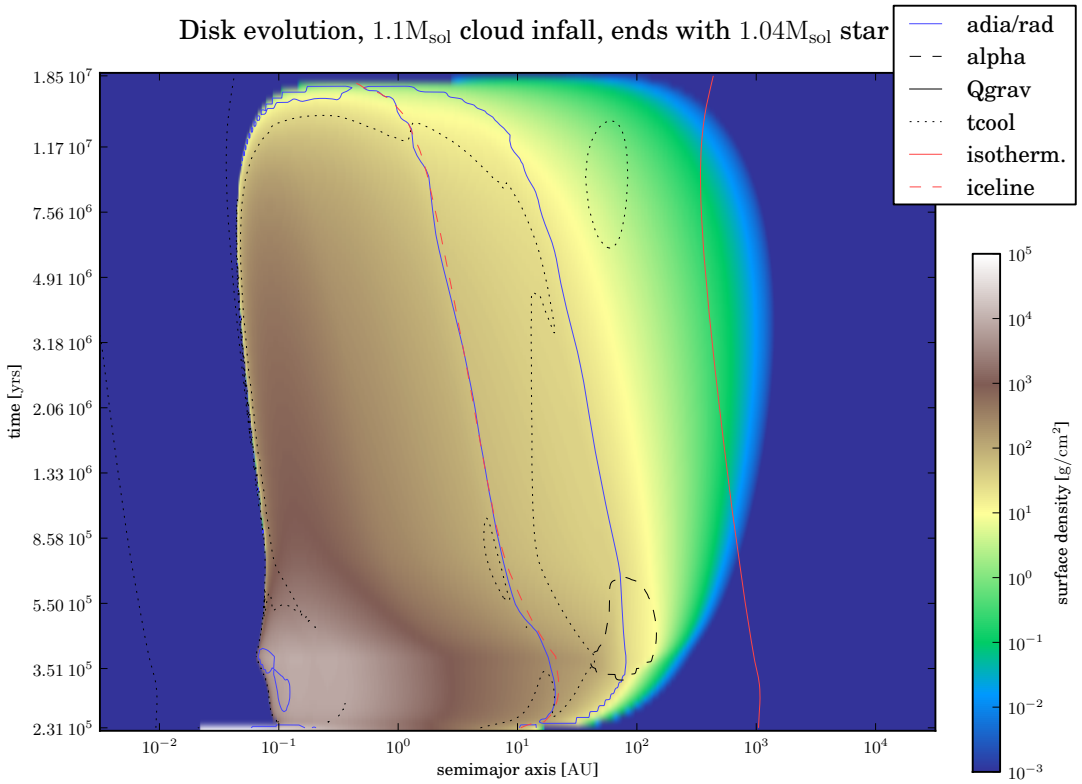

Figure 4.3 surface density evolution with initial conditions are $\alpha = 0.008$, $M_{\text{wind}} = 10^{-6}\,\mathrm{M}_\odot/\mathrm{yr}$, and a SIS cloud with $M_{\text{disk}} = 1.1\,\mathrm{M}_\odot$, $T_{\text{cl}} = 15\,\mathrm{K}$ and $\Omega_{\text{cl}} = 10^{-14}\,s^{-1}$. All contour lines are explained in the text at the beginning of Section 4.7

4.7 Single disk evolution

After describing or model we will now discuss the evolution of two different star-disk systems evolving out of two sets of initial conditions, one for each infall model.

4.7.1 Small SIS cloud

The first systems set of initial conditions are $\alpha = 0.008$, $M_{\text{wind}} = 10^{-6}\,\mathrm{M}_\odot/\mathrm{yr}$, and an singular isothermal sphere with $M_{\text{disk}} = 1.1\,\mathrm{M}_\odot$, $T_{\text{cl}} = 15\,\mathrm{K}$ and $\Omega_{\text{cl}} = 10^{-14}\,s^{-1}$. For this disk the initial set up phase ends at $\approx 2{\cdot}10^4$yr after the start of infall with a disk of $0.01\,\mathrm{M}_\odot$ around a $0.66\,\mathrm{M}_\odot$ protostar and the simulation starts. Infall and buildup phase ends after $3.76{\cdot}10^5$yr at which point we have $0.23\,\mathrm{M}_\odot$ disk around a $0.82\,\mathrm{M}_\odot$ star. At this point the centrifugal radius $a_c \approx 60\,\mathrm{AU}$. Yet the disk already spread to almost 300 AU at this point. It will spread for the next few million years until at roughly 5 Myr the external photoevaporation finally balances with the mass outflow and the disk begins to shrink. The gas will be finally gone after 18.5 Myr. Over the whole accretion the star grows to $1.04\,\mathrm{M}_\odot$.

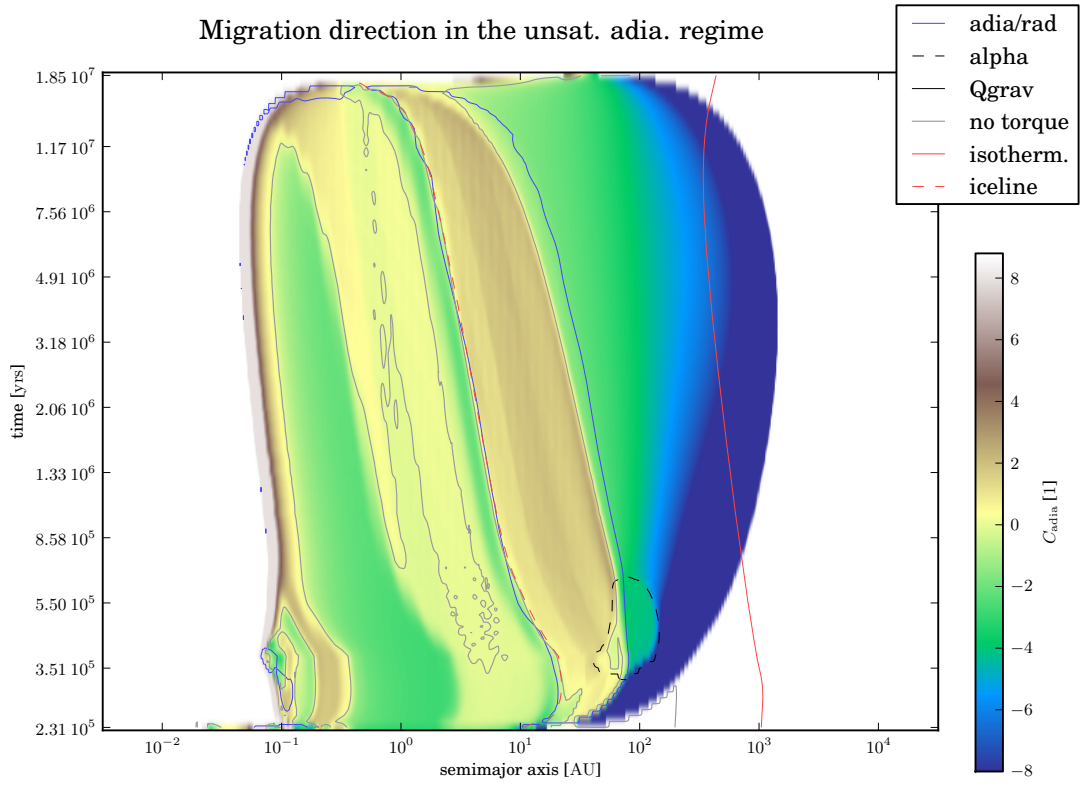

Figure 4.4 Direction of migration in the unsaturated adiabatic migration regim. All contour lines are the same as in Figure 4.3 except the grey line, this marks the points of zero torque.

This can be seen in Figure 4.3, which shows the evolution of the surface density of said system color coded over semimajor axis and time. Also shown are the positions of the iceline(red dashed line), the transition from radially isothermal to vertically isothermal (red solid line), the transition between vertically convective and radiative energy transport in the temperature model (blue line). Black dotted line marks the position where vertical cooling time is equal to the orbital time and the region surrounded by the black dashed line is gravo-turbulent ($\alpha > \alpha_{\min}$). A solid black line would mark a region with a Toomre parameter $Q < 1$ which does not exist in this disk.

The first blue line from the right also marks the transition from irradiation dominated to viscous heating dominated. As discussed in Chapter 3, for conditions between optically thick and thin the temperature model gives slightly smaller midplane temperature for the convective case, therefore the disk is assumed to be convective for a region just inside the transition from irradiation dominated to viscously dominated up to the iceline. Outside of this most distant blue line the disk is totally optically thin in vertical direction, the height of the radiative surface H_s is zero and midplane and surface temperature the same.

Also close to the inner edge a small part of the disk is convective for a short time at the beginning. Otherwise the disk is radiative for the complete evolution. The inner edge itself stays relatively constant slightly inside of 0.1 AU. The small changes are due to changes in the stellar radius. Only at the end does it with the drop in accretion rate due to the vanishing disk move relatively fast further out. Outside of 1 AU it is the internal photoevaporation which pushes it even further.

We also show, as we did in Section 2.4.3, the direction of migration in the unsaturated adiabatic migration regime in Figure 4.4. Color coded is the strength of migration in the unsaturated adiabatic regime C_{adia} with greenish blue color showing inward and yellow-brown-grey colors showing outward migration. White are regions without any gas. For most of the evolution of the disk there are again the typical two convergence zones. Only at the beginning at the part of the disk where it is convective we have a bit more complex migration behavior with a few alternation inward-outward regions. Here changes in the adiabatic coefficient γ and the mean moleculare weight lead to changes in the temperature slope which changes the migration behaviour. One also sees that the inner edge of the disk has really large values of C_{adia} due the the strong drop of the surface density. This drop of Σ will also introduce strong torques. These torques will stop all type I migrating planets. The outer converging zone is close to the transition between stellar irradiation and viscous heating. The inner one is at the iceline. Inside the outward migration region of that convergence zones one sees a weak inward migration region vanishing over time. The reason for this one is the iceline at the radiative surface which leads to a smaller bump in midplane temperature than the midplane iceline. Yet it is strong enough turn the movement of the migrating planets inward.

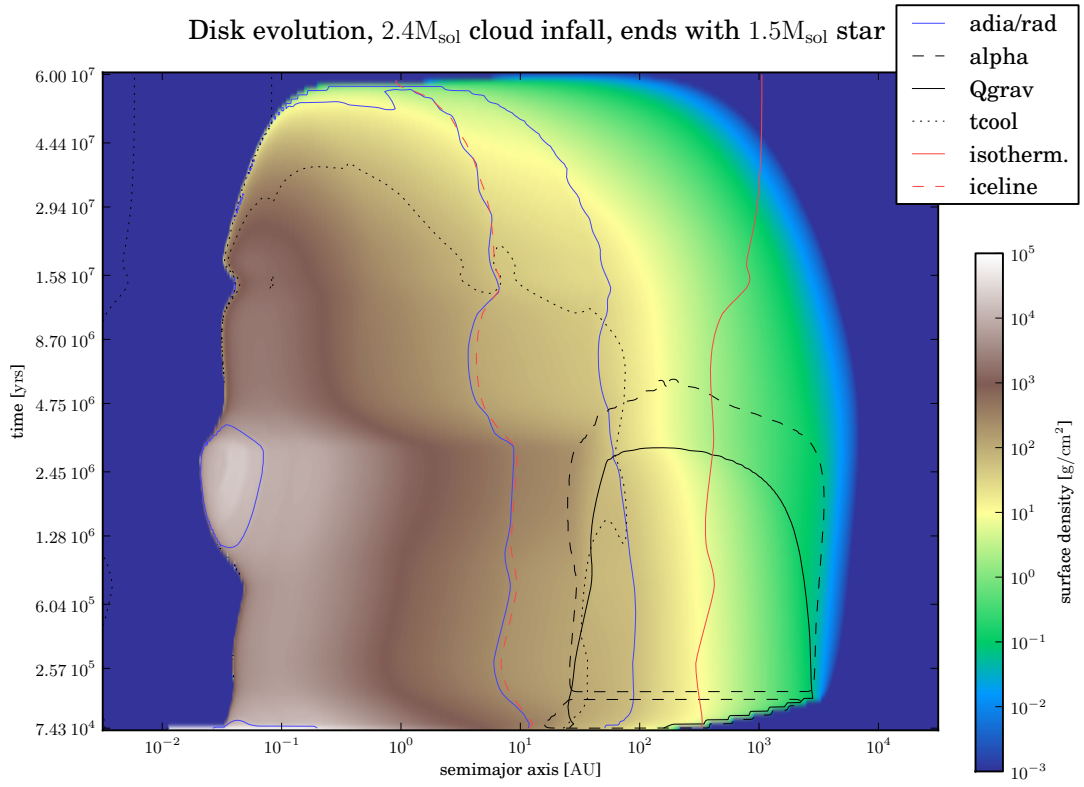

Figure 4.5 surface density evolution with initial conditions are $\alpha = 0.005$, $M_{\rm wind} = 10^{-6}\,{\rm M}_\odot/{\rm yr}$, and a BES cloud with $M_{\rm disk} = 2.4\,{\rm M}_\odot$, $T_{\rm cl} = 20\,{\rm K}$ and $\Omega_{\rm cl} = 10^{-13}\,s^{-1}$. All contour lines are explained in the text at the beginning of Section 4.7

.

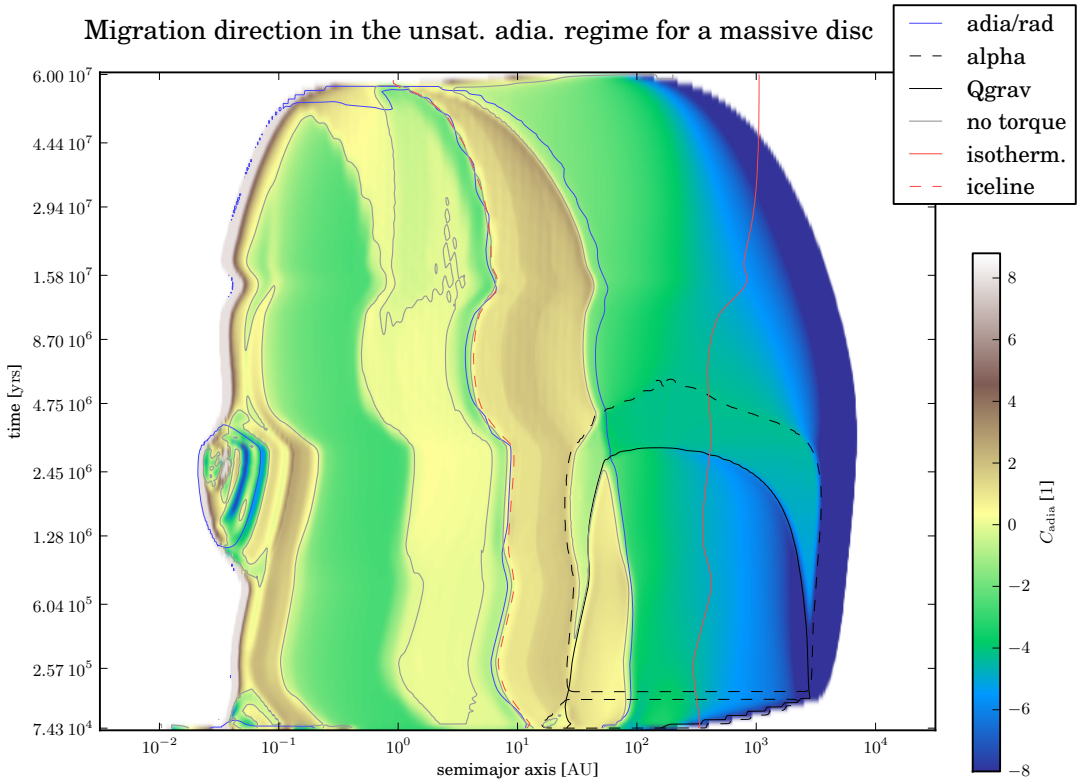

Figure 4.6 Direction and strength of migration in the unsaturated adiabatic migration regime for a disk with the initial conditions as $\alpha = 0.005$, $M_{\text{wind}} = 10^{-6}\,\text{M}_\odot/\text{yr}$, and a BES cloud with $M_{\text{disk}} = 2.4\,\text{M}_\odot$, $T_{\text{cl}} = 20\,\text{K}$ and $\Omega_{\text{cl}} = 10^{-13}\,s^{-1}$. All contour lines are the same as in Figure 4.3 except the grey line, this marks the points of zero torque.

4.7.2 Large BES cloud

The second set of initial conditions are $\alpha = 0.005$, $M_{\rm wind} = 10^{-6}\,{\rm M}_\odot/{\rm yr}$, and a BES cloud with $M_{\rm disk} = 2.4\,{\rm M}_\odot$, $T_{\rm cl} = 20\,{\rm K}$ and $\Omega_{\rm cl} = 10^{-13}\,s^{-1}$. This setup leads to a bit more interesting disk evolution, as can be seen in Figure 4.5. It is similar to Figure 4.3 and shows color coded the evolution of surface density. Also all contour lines are similar. Since BES infall rates are much larger than those of SIS, and even tho the first gas only accumulates after one infall time, the initial setup phase ends much earlier than in the SIS case. The simulation starts at $7.5{\cdot}10^4$yr with a $0.1\,{\rm M}_\odot$ protostar and a $0.2\,{\rm M}_\odot$ disk. At the end of the infall phase at only 150 kyr the disk has grown to $2.2\,{\rm M}_\odot$, the star has only gained $0.06\,{\rm M}_\odot$. The disk vanish after almost $60 Myr$, with a $1.5\,{\rm M}_\odot$ left behind. The interesting thing is that with the BES the outer radius of the disk during the infall phase is set by the fast spreading centrifugal radius $a_{\rm c}$. For this disk it will be at 3000 AU, from there on the disk spreads further to a maximum size of 6350 AU.

Overall the evolution can be separated into 2 phases. First is marked by the presents of gravo-turbulence in the outer disk, the second with the absence of it. The large centrifugal radius $a_{\rm c}$ leads to a lot of mass deposited in the outer regions which will create a massive outer disk which is gravitational unstable. As can be seen in Figure 4.5 the inner desk increases in mass (grey area getting larger) as long as $Q < 1$ at some point in the disk. Since we cab Q at 1 $\alpha_{\rm GI}$ depends only on $/mu_{\rm GI}$. This large alpha will leads to a large mass flow from the outer disk into the inner disk. This flow is sustained by the mass in the outer disk and will set the surface density profile in the inner disk. Since the disk mass is falling, $\alpha_{\rm GI}$ will raise slowly which leads to an even larger surface density in the inner disk. This process goes on until the outer part is depleted of enough mass to turn gravitationally stable. After that point the mass flow from the outer disk will drop fast and with this also the surface density in the inner disk. For the disk here, this happens a roughly $3.5\,Myrs$. At this point the surface density in the inner disk is so large that the disk is convective close to the inner edge. Also changes in the stellar radius and the increase in the accretion rate pushes the inner edge close to 0.02 AU. Otherwise for most of the simulation the inner edge is between $0.03 - 0.04$ AU. As can also be seen by the position of the dotted line, the vertical cooling time is smaller than an orbital time in the outer disk, especially also where $Q < 1$. Therefore, if the disk is gravo-turbulent, it should also fragment and probably form through direct collapse some massive planets between a few 10 AUs and at least a few hundred AUs from the star. Yet we do not include this here by the removal of gas into those planets. It could be one ways to decrease the disk mass fast. The second phase of the evolution is after the disk become stable. The mass further decrease, the surface density drops at all distances, the disk shrinks and finally vanishes.

We also show in Figure 4.6 the direction and strength of type I migration in the unsaturated adiabatic migration regime. For these massive disk the outer convergence zone is for the first part of evolution between 30 and 100 AU, which is much further away than before. From there it is slowly moving inward to hit ≈ 3 AU at the end of the evolution. One can also see that the inner edge of the gravo-turbulent region influences the outer convergence zone. Since α is no more constant we have to consider

its slope β_α when calculating the mass flow. To get a radially constant mass flow

$$\beta_T + \beta_\Sigma + \beta_\alpha = -1.5. \tag{4.47}$$

So the change in α changes the slopes of temperature and surface density which results in the visible cut into the outward migration region. This leads to an almost constant position of the convergence zone for some million years. An other cut into the outward migration region of the inner convergence zone at the later phase of the disk evolution is again due to the iceline at the surface. Also this position close to 1 AU does not change much since the star at this point does not change much anymore.

4.8 Small set of initial conditions.

Before we discuss the Initial conditions in more general terms we will show here a small sample of different disks. Initial conditions for infall models are temperature T_{cl} or sound speed $c_{s,cl}$, solid rotation frequency Ω_{cl} and cloud mass M_{cl} for the infalling cloud and α and M_{wind} for the evolution of the disk. We run seven different sets of T_{cl} and Ω_{cl} for both SIS and BES cloud infall in the first part of the section and for both stellar evolution models in the second part.

4.8.1 Comparison of SIS and BES disk evolution

We compare the evolution of the disc mass for this small set of initial conditions in Figure 4.7. In all simulations cloud mass $M_{cl} = 1.1\,M_\odot$. Also $\alpha = 0.008$ and $M_{wind} = 10^{-6}\,M_\odot/\mathrm{yr}$ are the same for this set of simulations. We use the combinations of Ω_{cl} and Tc that are stated in the legend of Figure 4.7. The first of these simulations (red dashed line) is the first disk discussed in more detail the previous chapter. The end of the infall phase is marked by the maximum of the disk mass in this figure. For the BES case (as for SIS) with constant Ω_{cl} one finds larger disks and longer infall phases for cooler clouds. One also sees that for the same temperature different rotational frequencies only lead to different disk masses but the same duration of the infall phase. Comparing now BES and SIS simulations for the same initial conditions one sees the BES clouds collapse roughly four times faster than the SIS clouds due to the much higher infall rates. Also for larger rotation frequencies Ω_{cl} the disk are more massive for the BES clouds (peak between dashed and solid line for the red, green, blue, and grey line), with the difference larger for colder clouds. The centrifugal radius increase more strongly at the end of the infall of a BES cloud. Therefore, especially for faster rotating and slower collapsing clouds, more mass is deposited further out, increasing disk mass and prolonging the lifetime. Overall the disks in this sample of initial conditions "live" for 5 to 20 Myr, although the overall systems all had the same mass and evolution parameters. As we don't change α or photoevaporation rate the lines do not cross, all disk evolve in the same manner and only disk mass and size at the end of the infall phase determine the age of the system. The age spread is also similar for SIS and BES simulations. At last also shown in Figure 4.7 are disk masses obtained for 16 different systems at different ages in Ophiuchus by Andrews et al. (2010). The simulations cover the same range of disk masses.

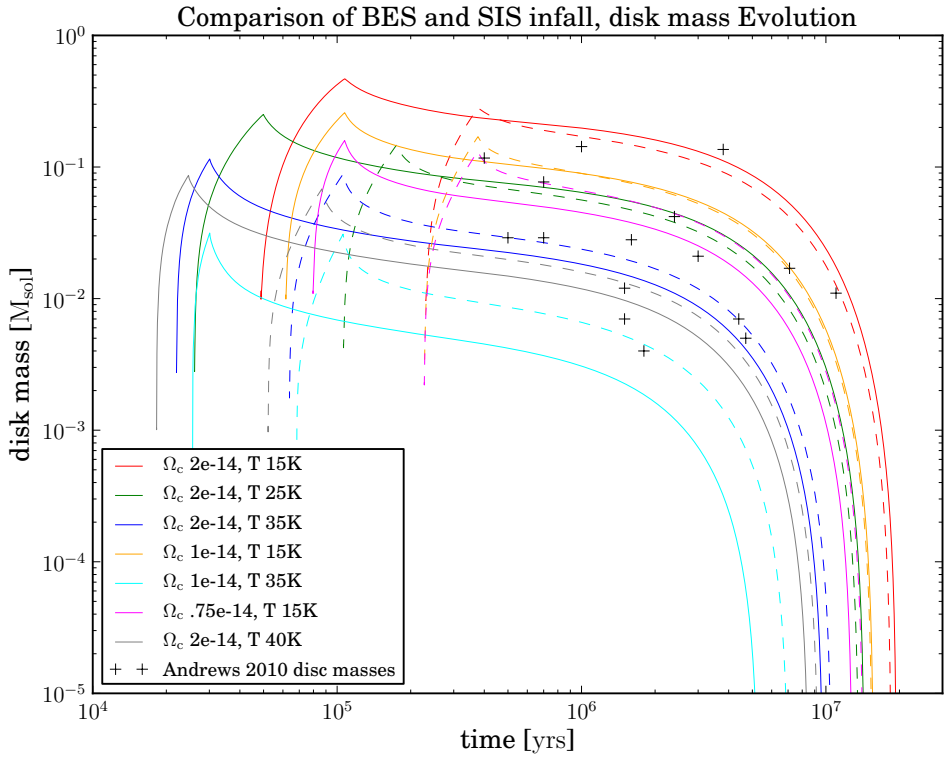

Figure 4.7 Disk mass evolution for 7 different initial conditions for the Bonnor-Ebert-Sphere infall (solid) and SIS infall (dashed). Black stars are disk masses obtained by Andrews et al. (2010).

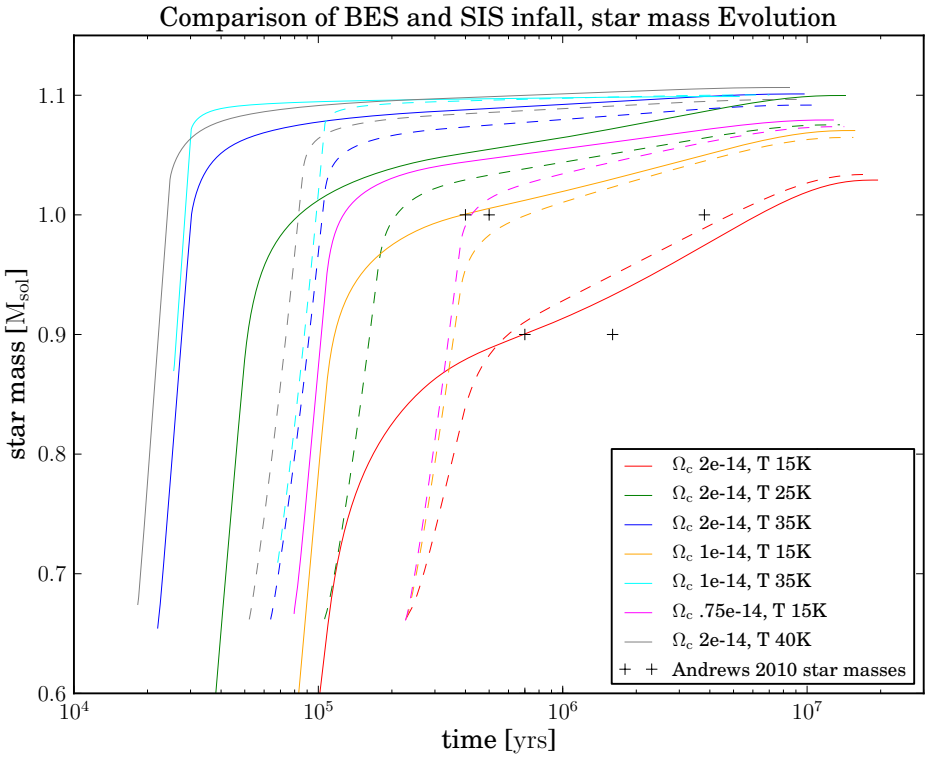

Figure 4.8 Star mass evolution for 7 different initial conditions for the Bonnor-Ebert-Sphere infall (solid) and SIS infall (dashed). Black stars are star masses obtained by Andrews et al. (2010).

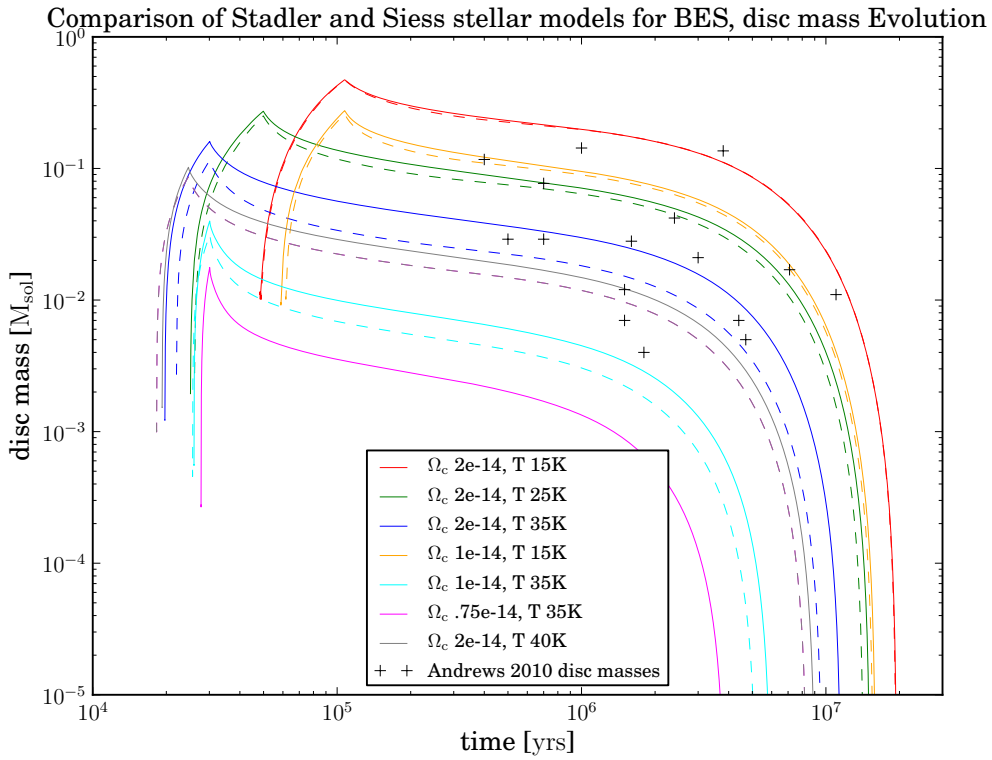

Figure 4.9 Disk mass evolution for 7 different initial conditions for the Bonnor-Ebert-Sphere infall with stellar evolution table of Siess et al. (2000) (solid) and Stahler and Palla (2005) (dashed). Black stars are disk masses obtained by Andrews et al. (2010).

Next we show for the same simulations also the evolution of the host (proto-) star in Figure 4.8. Here on can see that both BES and SIS clouds lead for identical initial conditions to similar stellar masses at the end of the evolution. Since we have almost no photo evaporation we end for all simulations with stars between 1 and 1.1 $M_\odot$. Marked are again the star masses of Andrews et al. (2010). There are only 5 crosses since all the other 11 systems have star masses outside of the range shown in Figure 4.8. So while we hit the range for the disk masses with varying only rotational frequency and temperature, we need to change the other parameters too if we want to hit the star masses.

4.8.2 Comparison of both stellar evolution models

In Figure 4.9 we finally compare the difference of the 2 stellar models described in Section 4.6. We use the same seven BES clouds as in the previous sub section. The difference in disk mass evolution is larger for those simulations in which we already have a larger star mass initially, while for those simulations with large disks and small star at the beginning we almost see no differences (red lines). The lifetimes vary in the end by a factor of 10% at most. Yet there is one exception. The slowest and hottest

rotating system (magenta) did not produce a disk during the initial set up phase at all, collapsing directly onto the star.

Chapter 5

Initial conditions

In this chapter we present the distribution of Initial conditions we can use to derive a list of initial conditions for planet population synthesis calculations. We calculated the evolution of infalling BES and SIS clouds on a grid of different initial conditions. The grid contained 51744 sets of initial conditions of SIS clouds and a smaller subset of 4704 initial conditions of BES clouds. We discuss the properties of these simulations in the first part of this chapter. The second part contains the calculation of the likelihood of initial conditions and the discussion of the obtained distributions of them.

As in the last part of the previous chapter we use five initial conditions, namely the viscous α parameter, the scaling factor of external photoevaporation $M_{\rm wind}$ for the evolution of the disk and solid rotation frequency $\Omega_{\rm cl}$, temperature $T_{\rm cl}$, and mass $M_{\rm cl}$ of the collapsing clouds.

5.1 Lifetimes and Star masses

5.1.1 SIS clouds

For the SIS cloud grid we use all combinations of

- $\alpha = \{0.001, 0.003, 0.005, 0.007, 0.01, 0.014\}$
- $M_{\rm wind} = \{1{\cdot}10^{-6}, 3{\cdot}10^{-6}, 1{\cdot}10^{-5}, 3{\cdot}10^{-5}, 1{\cdot}10^{-4}, 3{\cdot}10^{-4}, 1!\cdot10^{-3}\}{\rm M}_\odot{\rm yr}^{-1}$
  which corresponds to
  $\dot{\Sigma}_{\rm w} \approx \{3{\cdot}10^{-16}, 1{\cdot}10^{-15}, 3{\cdot}10^{-15}, 1{\cdot}10^{-14}, 3{\cdot}10^{-14}, 1{\cdot}10^{-13}, 3{\cdot}10^{-13}\}{\rm g\,s^{-1}\,cm^{-2}}$
- $\Omega_{\rm cl} = \{0.2, 0.4, 0.8, 1.6, 3.2, 6.4, 12.8\}10^{-14}{\rm s}^{-1}$
- $T_{\rm cl} = \{10, 15, 20, 25, 30, 35, 40, 45\}{\rm K}$
- $M_{\rm cl} = 0.1 - 2.4{\rm M}_\odot$ in $0.1{\rm M}_\odot$ increments

This gives us a total of 51744 simulations. The range realistic of α values is suggested by MRI (Flock et al., 2011) or 3D hydro turbulence simulation (Blabla, 20xx). It

also includes the value of 0.007 used in the previous model (Chapter 2). The spread of $M_{\rm wind}$ if set to provide somewhat reasonable lifetimes and mass loss rates at the same time. The observed range for $\Omega_{\rm cl}$ is $0.1 - 13 \cdot 10^{-14} {\rm s}^{-1}$ (Goodman et al., 1993; Caselli et al., 2002) and for $T_{\rm cl}$ is 5-40 K (Jijina et al., 1999). For the cloud mass we adopt a similar range as Jin and Li (2014) cutting only the more massive clouds, because we will use the data to fit observations of Andrews et al. (2010) and their most massive star is $2\,{\rm M}_\odot$.

Figure 5.1 shows the maximal disk mass (at the end of the infall phase) for a subset of the combinations above. It shows that larger cloud masses give larger disks, higher cloud temperatures smaller disks since there are higher infall rates and thus more mass is deposited directly onto the star. In addition. faster rotating clouds produce larger disks because less mass is falling onto the star. In general, also stronger photoevaporation and higher α lead to larger disks. There is one exception to the above. Massive 10 K clouds of faster rotation and stronger viscosity (top row of the lower right corner of the subplots in Figure 5.1) have smaller maximal disk masses than warmer clouds where the other four parameters are the same. The reason here is that we ramp up photoevaporation during the end of the infall phase (scaling $M_{\rm wind}$ with the ratio of already collapsed mass to cloud mass) already removing mass from the disk before all the cloud has collapsed. Since the infall rate depends strongly on the temperature it takes roughly twice as long for 10 K clouds to collapse as for 15 K clouds. This longer infall time allows the photoevaporation to remove more mass. This is especially true when α is larger and the disk is spreading faster. Therefore, in that case more area is exposed to the photoevaporating irradiation removing more mass.

Figure 5.2 shows the lifetime of the same subset as in Figure 5.1. Again, the general trend is as expected. Larger cloud mass and faster rotation increases lifetime, stronger photo evaporation and viscous transport reduces the lifetime. A bit more interesting is the dependence on the cloud temperature. Here one can find both effects depending on the other initial conditions: an increase can lead to longer or shorter lifetimes. In most cases an increase in temperature will lead to a short lifetime. Yet, similar to the maximal disk masses, large photo evaporation rates together with faster rotation and larger disk masses and smaller α values lead to a drop in lifetime with a drop in temperature. This can change the lifetime up to a factor of two in the most extreme cases. The disk lifetime ranges from a few hundred thousand years for light clouds to a hundred million years for the most massive clouds in the grid. Most smaller disks have lifetimes of a few million years which is consistent with observations (Haisch et al., 2001; Mamajek, 2009).

Figure 5.3 shows the time averaged (over the lifetime of the disk) photoevaporation rate of the same subset as in Figure 5.1. Large photo evaporation scaling factors $M_{\rm wind}$ give larger averaged rates, yet they scale not linearly with each other. A change of 3 orders of magnitude in $M_{\rm wind}$ changes the averaged rate only by a factor of a few for small disks to an order of magnitude for the largest disks. This is due to the balance between outer disk radius and photo evaporation. A larger evaporation rate results in smaller outer radius, which gives less disk area to be photoevaporated and therefore a comparable smaller increase in the amount of evaporated mass. We acknowledge that especially those disks with $M_{\rm wind} = 10^{-3} {\rm M}_\odot {\rm yr}^{-1}$ show too large rate. Review by

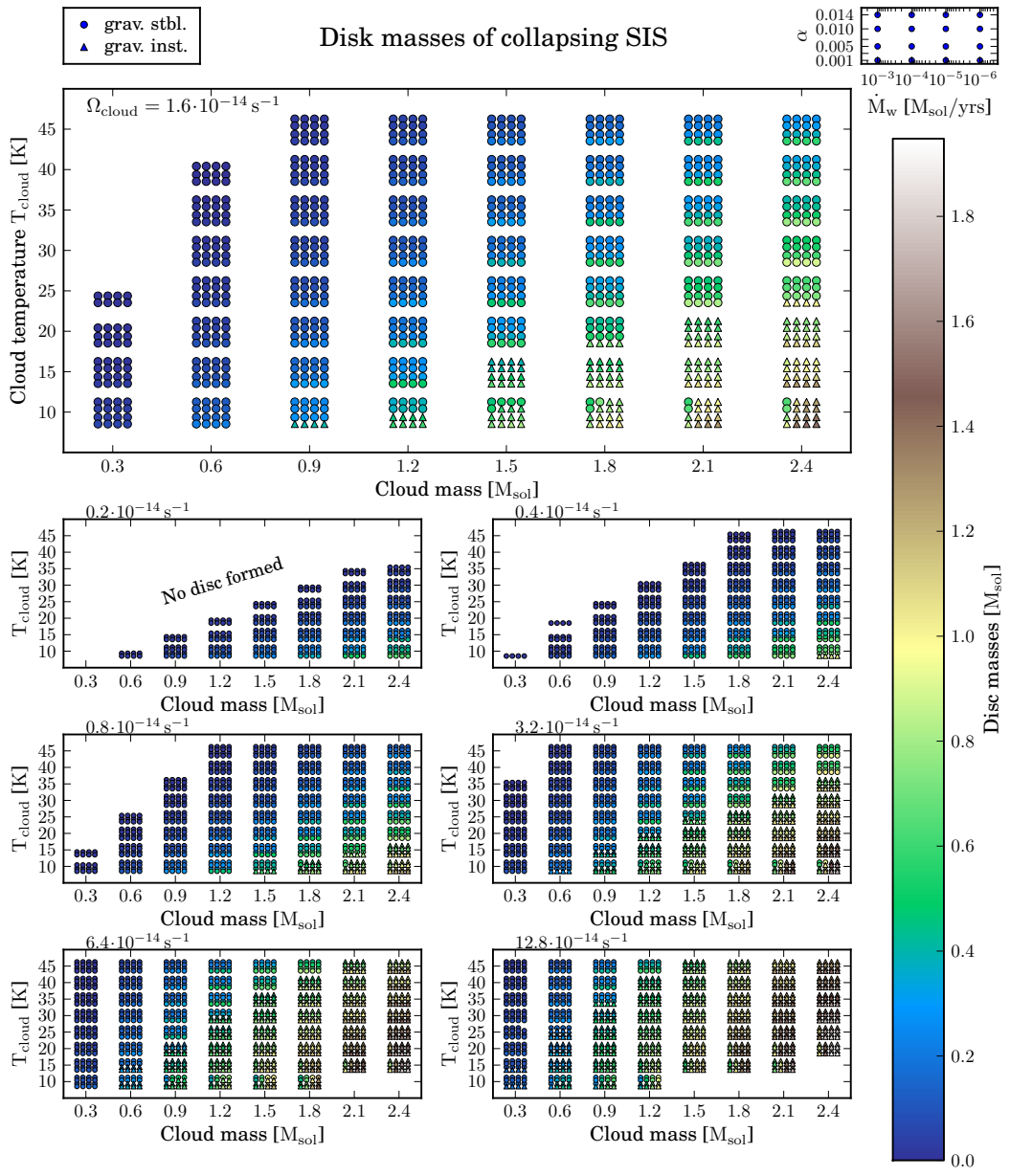

Figure 5.1 shows maximal disk masses from collapsing SIS. Each subplot shows color coded the maximal disk mass for one Ω_{cl} over cloud temperature T_{cl} and mass M_{cl}. For each point of these three initial conditions a cluster of data is shown for different viscous α parameters and photo evaporation scaling factors M_{wind}. The corresponding meaning is shown in the small top right subplot. Furthermore, triangles mark those simulations in which at some semimajor axis at some point during the evolution a Toomre parameter $Q < 1$ was found. Circles mark those in which this is not the case. Missing dots are a sign of either the cloud collapsed completely onto the star (Initial setup found no disk; top left corner of each of the seven subplots), the disk got larger than the computational domain during infall phase (lower right corner), or an error occurred (24 simulations).

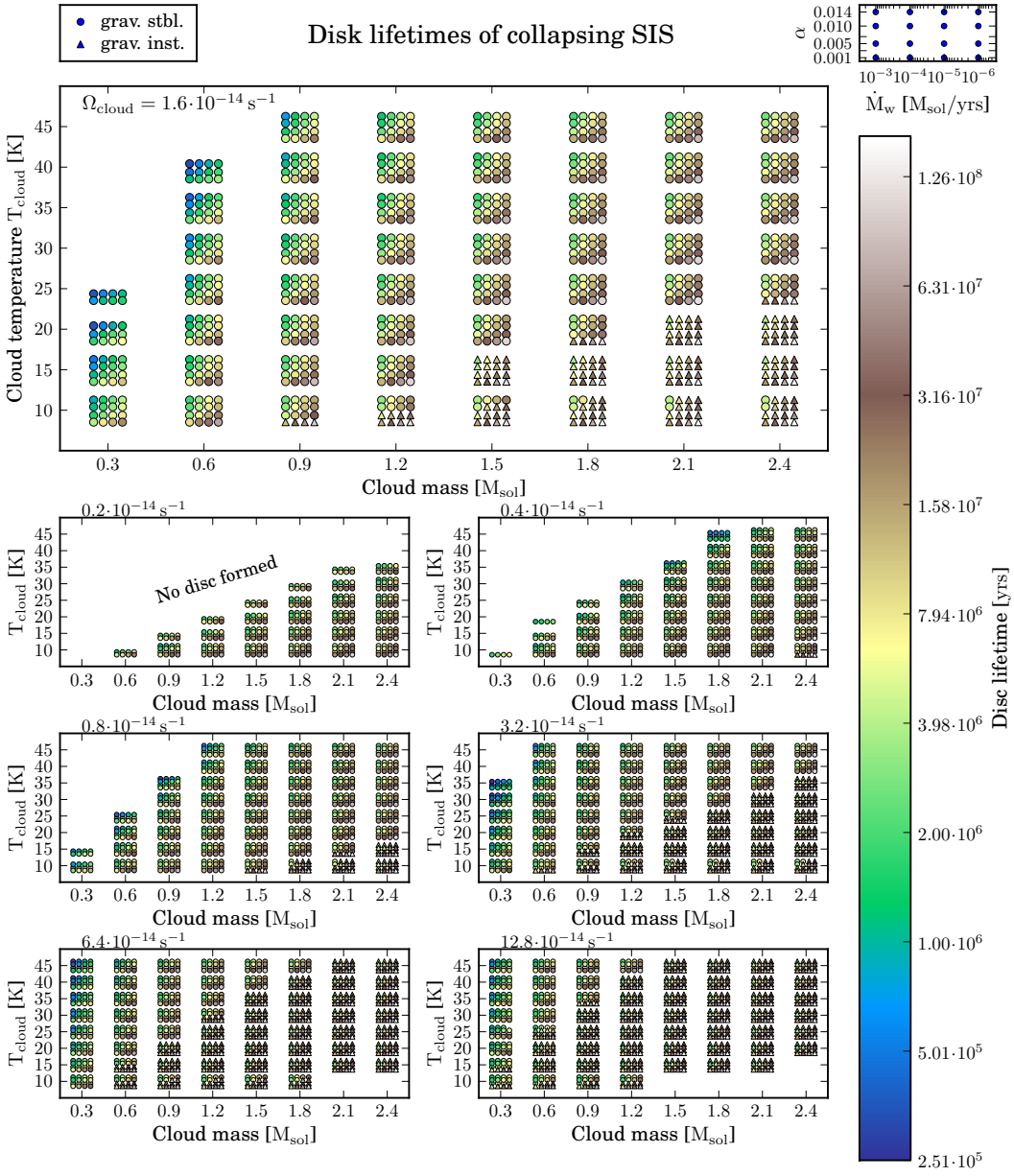

Figure 5.2 shows disk lifetime from collapsing SIS. Each subplot shows color coded the lifetime of disks for one Ω_{cl} over cloud temperature T_{cl} and mass M_{cl}. For each point of these three initial conditions a cluster of data is shown for different viscous α parameters and photo evaporation scaling factors M_{wind}. The corresponding meaning is shown in the small top right subplot. Furthermore, triangles mark those simulations in which at some semimajor axis at some point during the evolution a Toomre parameter $Q < 1$ was found. Circles mark those in which this is not the case. Missing dots are a sign of either the cloud collapsed completely onto the star (Initial setup found no disk; top left corner of each of the seven subplots), the disk got larger than the computational domain during infall phase (lower right corner), or an error occurred (24 simulations).

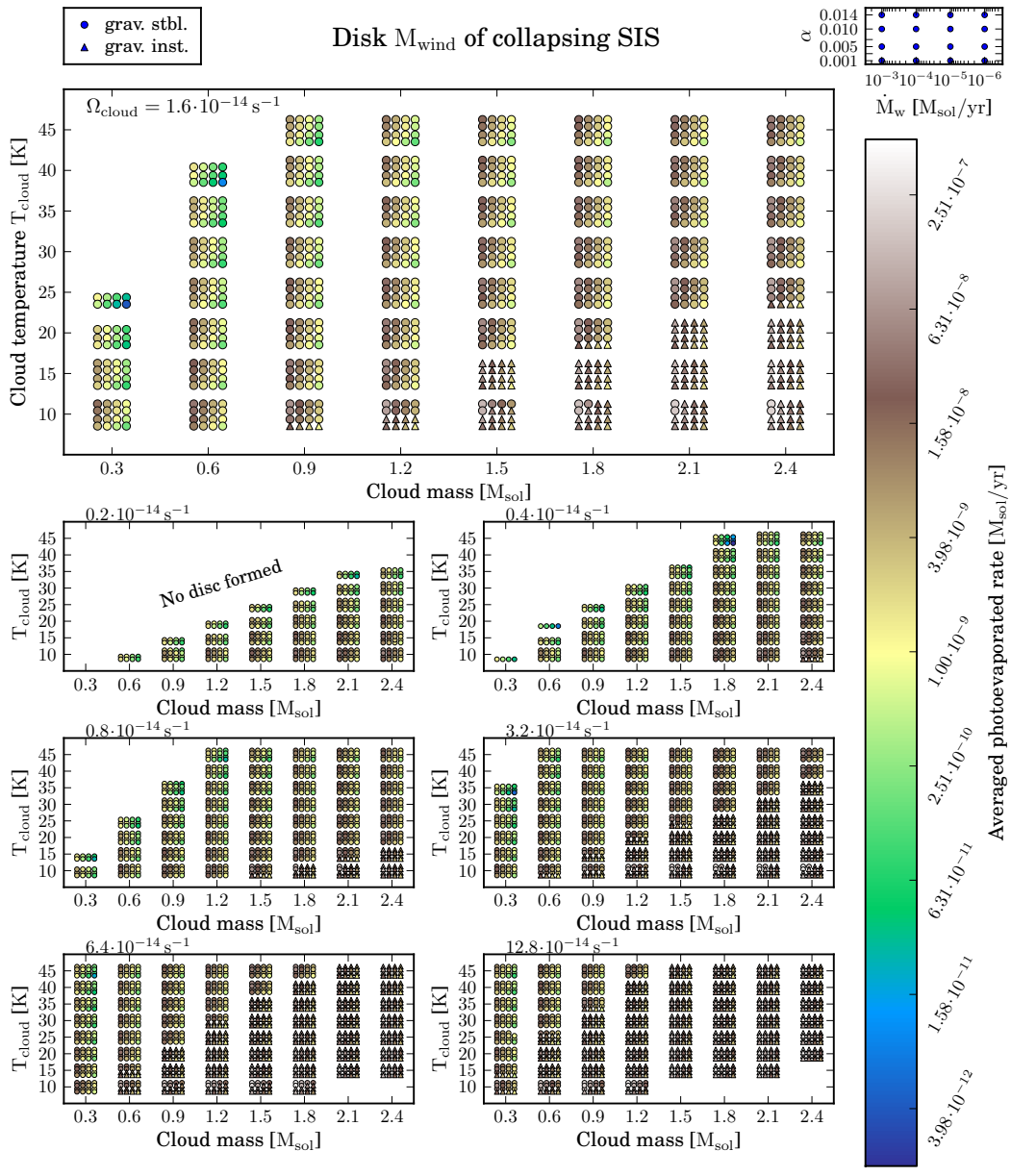

Figure 5.3 Time averaged photoevaporation rates of disks from collapsing SIS. Each subplot shows color coded the time averaged photoevaporation for one Ω_{cl} over cloud temperature T_{cl} and mass M_{cl}. For each point of these three initial conditions a cluster of data is shown for different viscous α parameters and photo evaporation scaling factors M_{wind}. The corresponding meaning is shown in the small top right subplot. Furthermore, triangles mark those simulations in which at some semimajor axis at some point during the evolution a Toomre parameter $Q < 1$ was found. Circles mark those in which this is not the case. Missing dots are a sign that either the cloud collapsed completely onto the star (Initial setup found no disk; top left corner of each of the seven subplots), the disk got larger than the computational domain during infall phase (lower right corner), or an error occurred (24 simulations).

(Alexander, 2014) on disk dispersal states photoevaporation rates between $\dot{M}_{\rm wind} = 10^{-10} - 10^{-8} {\rm M}_\odot {\rm yr}^{-1}$.

As can be seen in all three figures, there are combinations of cloud temperature, mass and rotation frequency that produce really compact objects with too small mass spread to be simulated by the model. The line separating these no disk models from those with disk changes its slope with increasing rotation frequency. It also depends on the α value as can be seen by the number of rows of each point cluster.

Finally in all three plots discussed above we have marked those disks which are gravitational unstable ($Q < 1$ at some point somewhere in the disk) by triangles and those that are not by circles. With increasing $\Omega_{\rm cl}$ we find more disks to become unstable as they become larger. We receive the same results with increasing cloud mass and decreasing temperature. Jin and Li (2014), study the collapse of SIS clouds, also found that the gravitational stability of disks from infalling clouds depends on those three quantities. We do not find the same but similar relations in this work here. Yet, as can be seen in the data for $T_{\rm cl} = 10$K photoevaporation also plays a role in determining if a disk becomes unstable or not. If one ignores this effect, the separating between stable and unstable can be fitted by a line similar to those found by Jin and Li (2014). As for the separation between disk and no disk, this lines slope changes with rotation frequency. However, we find a dependence on α while Jin and Li (2014) found no or only a weak dependence on the strength of viscosity.

5.1.2 BES clouds

For the BES cloud grid we use all combinations of

- $\alpha = \{0.003, 0.008, 0.014\}$
- $M_{\rm wind} = \{1{\cdot}10^{-6}, 1{\cdot}10^{-5}, 1{\cdot}10^{-4}, 1{\cdot}10^{-3}\} {\rm M}_\odot / {\rm yr}^{-1}$
  which corresponds to
  $\dot{\Sigma}_{\rm w} \approx \{3{\cdot}10^{-16}, 3{\cdot}10^{-15}, 3{\cdot}10^{-14}, 3{\cdot}10^{-13}\} {\rm g\,s^{-1}\,cm^{-2}}$
- $\Omega_{\rm cl} = \{0.2, 0.4, 0.8, 1.6, 3.2, 6.4, 12.8\} 10^{-14} {\rm s}^{-1}$
- $T_{\rm cl} = \{10, 15, 20, 25, 30, 35, 40\}$K
- $M_{\rm cl} = 0.1 - 2.4 {\rm M}_\odot$ in $0.3 {\rm M}_\odot$ increments

This gives us a total of 4704 simulations.

As for SIS clouds we show maximal disk mass in Figure 5.4, disk lifetimes in Figure 5.5, and time averaged photoevaporation rate in Figure 5.6. As we have used a much smaller grid for the BES we can show all simulations in these plots. The trend in all plots is the same as for SIS. However, there are some differences. The maximal disk masses are larger up to $\approx 25\%$. For the same photoevaporation scale factor and α the lifetimes are similar even though the disk masses are larger. Yet since BES disks are also larger the same photoevaporation rate will remove more mass from the disks formed out of BES, compensating for the larger disk masses. This is also seen in

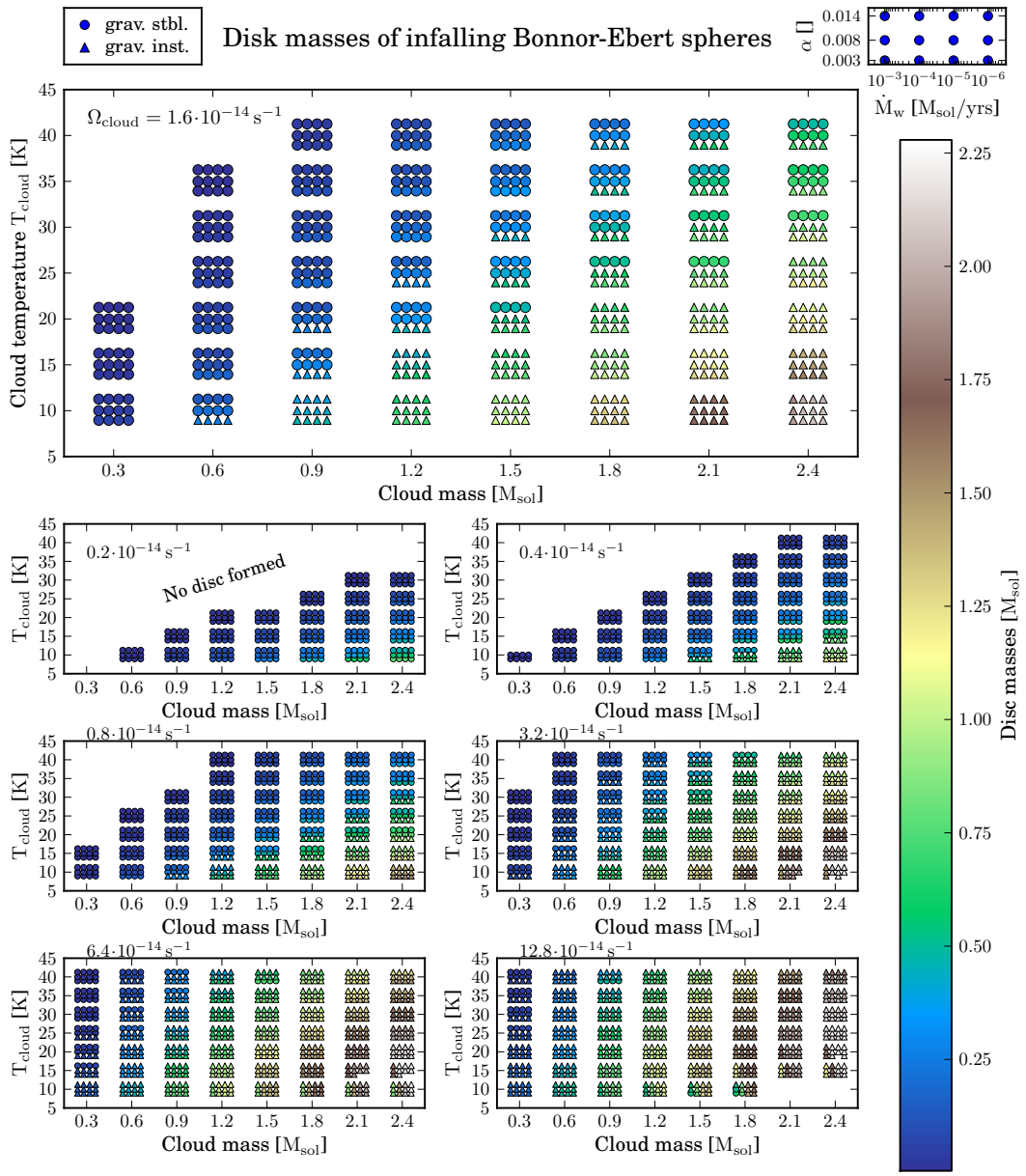

Figure 5.4 shows maximal disk masses from collapsing BES. Each subplot shows color coded the maximal disk mass for one Ω_{cl} over cloud temperature T_{cl} and mass M_{cl}. For each point of these three initial conditions a cluster of data is shown for different viscous α parameters and photo evaporation scaling factors M_{wind}. The corresponding meaning is shown in the small top right subplot. Furthermore, triangles mark those simulations in which at some semimajor axis at some point during the evolution a Toomre parameter $Q < 1$ was found. Circles mark those in which this is not the case. Missing dots are a sign that either the cloud collapsed completely onto the star (Initial setup found no disk; top left corner of each of the seven subplots), the disk got larger than the computational domain during infall phase (lower right corner), or an error occurred (8 simulations).

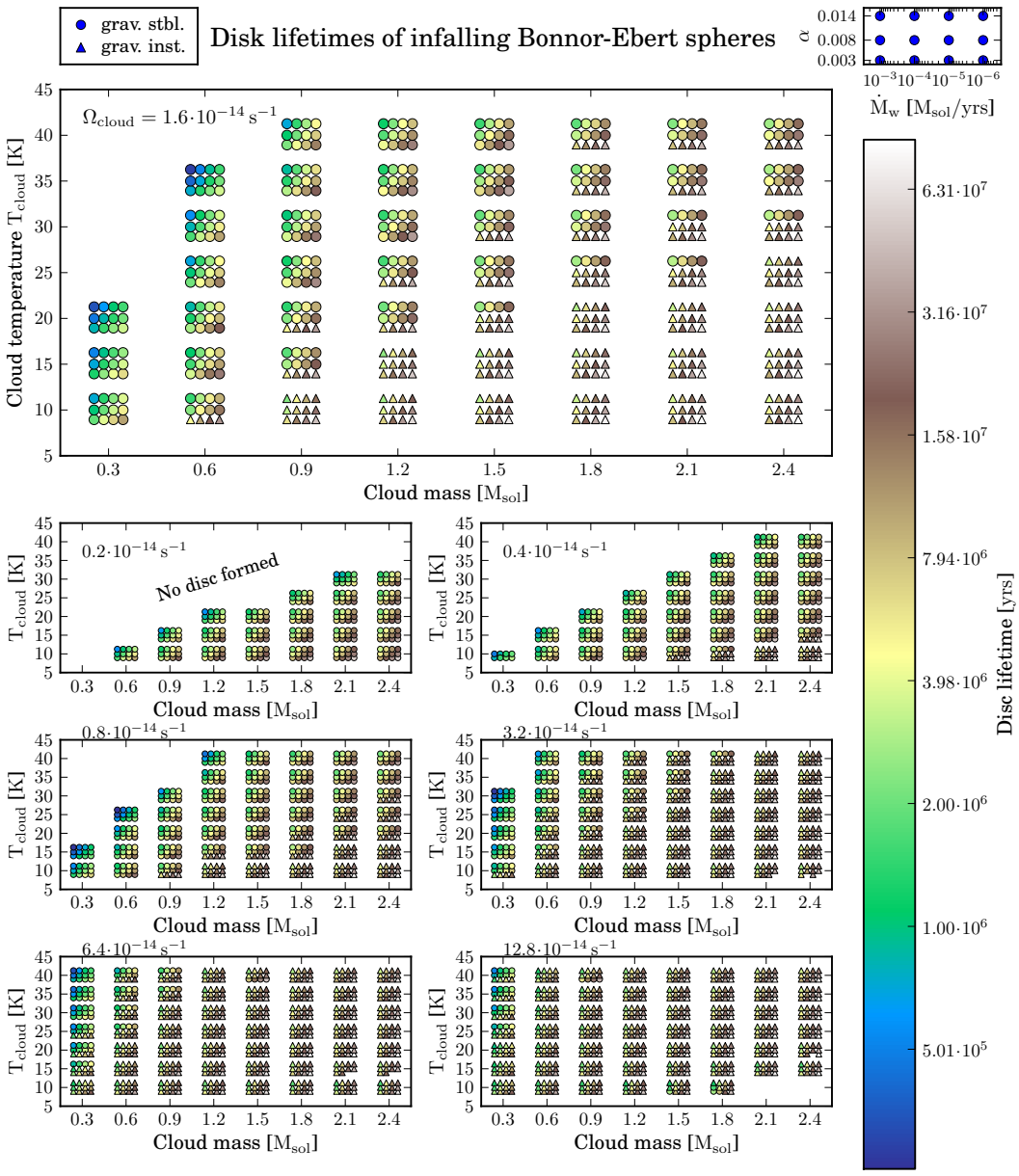

Figure 5.5 shows disk lifetime from collapsing BES. Each subplot shows color coded the lifetime of disks for one $\Omega_{\rm cl}$ over cloud temperature $T_{\rm cl}$ and mass $M_{\rm cl}$. For each point of these three initial conditions a cluster of data is shown for different viscous α parameters and photo evaporation scaling factors $M_{\rm wind}$. The corresponding meaning is shown in the small top right subplot. Furthermore, triangles mark those simulations in which at some semimajor axis at some point during the evolution a Toomre parameter $Q < 1$ was found. Circles mark those in which this is not the case. Missing dots are a sign that either the cloud collapsed completely onto the star (Initial setup found no disk; top left corner of each of the seven subplots), the disk got larger than the computational domain during infall phase (lower right corner), or an error occurred (8 simulations).

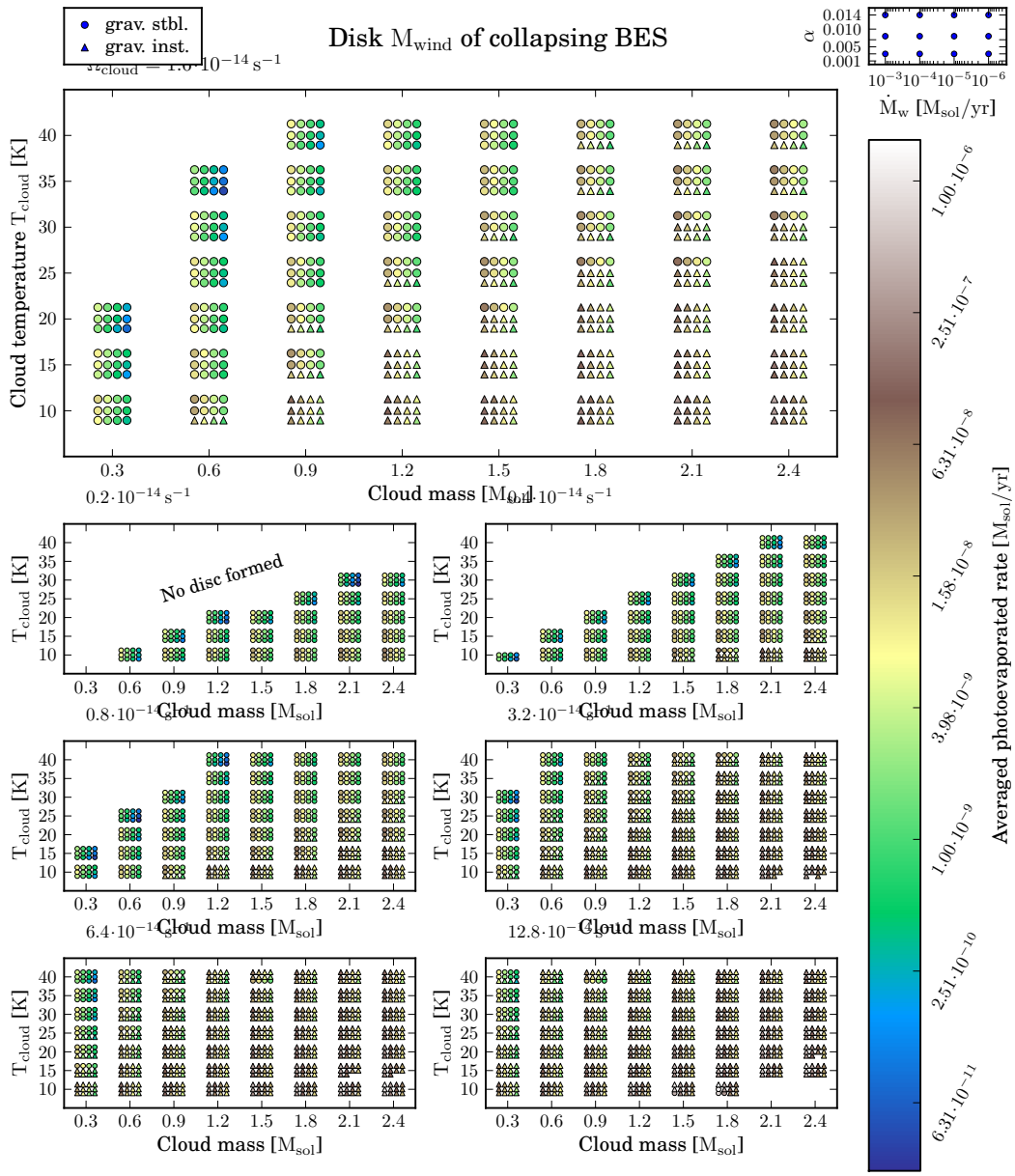

Figure 5.6 Time averaged photoevaporation rates of disks from collapsing BES. Each subplot shows color coded the time averaged photoevaporation for one Ω_{cl} over cloud temperature T_{cl} and mass M_{cl}. For each point of those three initial conditions a cluster of data is shown for different viscous α parameters and photo evaporation scaling factors M_{wind}. The corresponding meaning is shown in the small top right subplot. Furthermore, triangles mark those simulations in which at some semimajor axis at some point during the evolution a Toomre parameter $Q < 1$ was found. Circles mark those in which this is not the case. Missing dots are a sign that either the cloud collapsed completely onto the star (Initial setup found no disk; top left corner of each of the seven subplots), the disk got larger than the computational domain during infall phase (lower right corner), or an error occurred (8 simulations).

the larger averaged photoevaporation rates for BES. The larger size of the disks also lead to more disks becoming gravitationally unstable with half of time simulations for $\Omega_{\rm cl} = 1.6{\cdot}10^{-14}{\rm s}^{-1}$ being unstable in the BES case and only quarter in the SIS case. The region in initial condition of simulations where no disk formed are almost the same for both cases.

5.2 Distribution of initial conditions

To use our model for planet population synthesis calculations we need to know the distribution of the initial conditions so we can use a realistic list of initial condition sets.

5.2.1 Andrews disks

To obtain the distribution we compare our simulations with disks characterized by Andrews et al. (2010) by analysis of the irradiation from small dust grains in those disks. They state next to other parameters the age t, star mass $M_{\rm star}$, disk mass $Mdisk$, accretion rate onto the star $\dot{M}_{\rm acc}$ and outer radius $R_{\rm cutoff}$ of 16 disks in Ophiuchus. After some discussion with Till Birnstiel we double the values for disk mass and cutoff radius. The reason is that outside of the observable dust there has to be a reservoir of even smaller dust grains which replenishes the former by growth and drift. Accounting for this reservoir leads to a double in disk mass and size. Also the cutoff radius $R_{\rm cutoff}$ of the density profile in Andrews et al. (2010) is at a third of the distance from the star compared to the real outer radius of the disk. Therefore, we multiply it by a factor of six to obtain $R_{\rm out}$. We extract from our simulation for each age t given by Andrews et al. (2010) the disk mass $Mdisk$, accretion rate onto the star $\dot{M}_{\rm acc}$ and the outer radius of the disk $R_{\rm out}$. This we compare to their values and calculate a likelihood that they represent the same disk.

We assume that each measurement of Andrews et al. (2010) follows a Gaussian distribution. This means we have a pdf

$$p_{i,j,k} = \frac{1}{\sqrt{2\pi\sigma_{j,k}^2}} \exp\left(-\frac{\Delta x_{i,j,k}^2}{2\sigma_{j,k}^2}\right) \tag{5.1}$$

for each of the 4 quantities with the measurement $x_{0,j,k}$, the error $\sigma_{j,k}$ of the measurement and $x_{i,j,k}$ the value obtained from a simulation. The index k represents each of the 4 quantities, j each of the 16 disks, and i the simulation. Andrews et al. (2010) showed in their Figure 10 the uncertainty in their measurement of disk mass (0.1 dex) and cut off radius (0.2 dex). In private conversation he also stated an uncertainty of star mass (30%) and accretion rate (factor of 3, or 0.5 dex). $\Delta x_{i,j,k}$ is the difference between measurement and simulation. For star mass $M_{\rm star}$ ($k = 1$) we do

$$\Delta x_{i,j,k=1} = |x_{0,j,k=1} - x_{i,j,k=1}| \tag{5.2}$$

and $\sigma_{j,k=1} = 0.3 * x_{0,j,k=1}$. For the other three quantities $Mdisk$ ($k = 2$), $\dot{M}_{\rm acc}$ ($k = 3$), $R_{\rm out}$ ($k = 4$).

$$\Delta x_{i,j,k=2,3,4} = |\log_{10}(x_{0,j,k=2,3,4}) - \log_{10}(x_{i,j,k=2,3,4})| \tag{5.3}$$

and $\sigma_{j,k=2} = 0.2$, $\sigma_{j,k=3} = 0.5$, and $\sigma_{j,k=4} = 1.2$.

To transform this pdf into the likelihood of model value x fitting measurement x_0 one has to calculate:

$$L_{i,j,k} = 1 - \int_{-\Delta x_{i,j,k}}^{\Delta x_{i,j,k}} p_{i,j,k} dx. \tag{5.4}$$

which leads to

$$L_{i,j,k} = \text{erfc}\left(\frac{\Delta x_{i,j,k}}{\sqrt{2}\sigma_{j,k}}\right) \tag{5.5}$$

The integral in Equation (5.4) estimates the likelihood to find the "true" value of the measurement inside the range of Δx. Since Δx itself is not inside this range the likelihood for Δx itself is than written as in Equation (5.4). In truth this covers also all values larger than Δx yet the pdf itself is vanishing so fast that the value of Equation (5.4) is dominated by the pdf value at Δx.

After calculating $L_{i,j,k}$ for each of the 4 properties of one disk, we compute the likelihood $L_{i,j}$ for simulation i to fit disk j

$$L_{i,j} = \prod_{k=1}^{4} L_{i,j,k} \tag{5.6}$$

We show the simulation with the largest $L_{\rm tot} = L_{i,j}$ for each infall model and observed disk in Table 5.2.1 and Table 5.2.1. We did not try to maximize $L_{\rm tot}$ to find the best fitting initial conditions for each model but state the best values found in the grid. If a disk has already vanished at the time of observation j we assign a likelihood of 0.

While some disks are fitted quite well, a few others, especially SR 4, are not. For most disks, both SIS and BES case, the smallest likelihood is from the comparison of the accretion rates. Eq., in the case of SR 4, in both infall model grids, at a time of 3.8 Myrs, we find for disk mass in the range of $0.009\,{\rm M}_\odot$ a maximum accretion rate of around $10^{-8}{\rm M}_\odot/{\rm yr}$ which is a factor of 6 smaller than the one given for SR 4 by Andrews et al. (2010). According to Natta et al. (2006), the accretion rate is even $1.73{\cdot}10^{-8}{\rm M}_\odot/{\rm yr}$. We find those large accretion rates only for disks larger than $0.1\,{\rm M}_\odot$. Since we do not simulate any strong oscillation, like FU-Orionis burst, because of the short time steps involved in doing so, our accretion rates can be understood as long time averaged accretion rates. Keeping the model the same we would need to increase *alpha* above reasonable values to get such accretion rates. The opposite to SR 4 is disk WSB 60. Here the given accretion rate is smaller than what is found for any simulation in the grid at the given disk mass. The best α value is the smallest used in the grid. So using an even smaller α than 0.001 could provide a better model. In conclusion we can find IC inside the ranges we use to explain most disks in Andrews et al. (2010).

Disk name /sim. type	Age [Myr]	M_{star} [$M_\odot$]	M_{disk} [$M_\odot$]	$\dot{M}_{\text{acc}}$ [$M_\odot$/yr]	R_{out} [AU]	$L_{M_{\text{star}}}$ -	$L_{M_{\text{disk}}}$ -	$L_{\dot{M}_{\text{acc}}}$ -	$L_{R_{\text{out}}}$ -	L_{tot} -	α [1]	M_{wind} [$M_\odot$/yr]	Ω_{cl} [10^{-14}s^{-1}]	T_{cl} [K]	M_{cl} [$M_\odot$]
Elias 24	0.4	1.0	0.234	$2{\cdot}10^{-7}$	762	-	-	-	-	-	-	-	-	-	-
SIS	0.4	0.96	0.222	$1.6{\cdot}10^{-7}$	659	0.90	0.95	0.85	0.96	0.71	0.007	$1{\cdot}10^{-6}$	6.4	30	1.2
BES	0.4	0.98	0.235	$2.1{\cdot}10^{-7}$	702	0.95	0.99	0.98	0.98	0.90	0.014	$1{\cdot}10^{-5}$	0.8	10	1.2
AS 205	0.5	1.0	0.058	$8{\cdot}10^{-8}$	276	-	-	-	-	-	-	-	-	-	-
SIS	0.5	0.93	0.059	$7.1{\cdot}10^{-8}$	230	0.83	0.97	0.92	0.95	0.70	0.014	$1{\cdot}10^{-4}$	0.8	15	1.0
BES	0.5	1.12	0.070	$6.1{\cdot}10^{-8}$	265	0.69	0.70	0.81	0.99	0.38	0.014	$1{\cdot}10^{-3}$	0.4	10	1.2
WaOph 6	0.7	0.9	0.154	$1{\cdot}10^{-7}$	918	-	-	-	-	-	-	-	-	-	-
SIS	0.7	0.95	0.155	$7.9{\cdot}10^{-8}$	802	0.87	0.99	0.84	0.96	0.69	0.010	$1{\cdot}10^{-6}$	1.6	15	1.1
BES	0.7	0.87	0.151	$7.2{\cdot}10^{-8}$	418	0.92	0.96	0.78	0.78	0.53	0.014	$1{\cdot}10^{-3}$	12.8	30	1.2
VSSG 1	0.7	0.6	0.058	$1{\cdot}10^{-7}$	198	-	-	-	-	-	-	-	-	-	-
SIS	0.7	0.63	0.059	$4.2{\cdot}10^{-8}$	61	0.86	0.98	0.45	0.99	0.38	0.007	$1{\cdot}10^{-3}$	0.8	10	0.7
BES	0.7	0.46	0.058	$4.6{\cdot}10^{-8}$	300	0.42	0.98	0.50	0.88	0.18	0.014	$1{\cdot}10^{-3}$	3.2	10	0.6
GSS 39	1.0	0.6	0.286	$7{\cdot}10^{-8}$	1188	-	-	-	-	-	-	-	-	-	-
SIS	1.0	0.59	0.291	$6.0{\cdot}10^{-8}$	1293	0.94	0.97	0.89	0.98	0.80	0.010	$3{\cdot}10^{-5}$	3.2	10	0.9
BES	1.0	0.59	0.287	$6.2{\cdot}10^{-8}$	1999	0.96	1.00	0.92	0.85	0.74	0.014	$1{\cdot}10^{-5}$	12.8	20	0.9
SR 13	1.5	0.3	0.024	$3{\cdot}10^{-9}$	156	-	-	-	-	-	-	-	-	-	-
SIS	1.5	0.27	0.024	$3.1{\cdot}10^{-9}$	126	0.74	0.96	0.97	0.94	0.65	0.001	$3{\cdot}10^{-4}$	12.8	25	0.3
BES	1.5	0.28	0.023	$5.2{\cdot}10^{-9}$	250	0.85	0.90	0.64	0.86	0.42	0.003	$1{\cdot}10^{-4}$	6.4	15	0.3
WSB 52	1.5	0.5	0.014	$4{\cdot}10^{-9}$	156	-	-	-	-	-	-	-	-	-	-
SIS	1.5	0.48	0.014	$3.7{\cdot}10^{-9}$	153	0.88	0.99	0.95	0.99	0.81	0.003	$3{\cdot}10^{-4}$	3.2	20	0.5
BES	1.5	0.60	0.015	$4.6{\cdot}10^{-9}$	116	0.52	0.89	0.90	0.92	0.38	0.003	$1{\cdot}10^{-3}$	1.6	15	0.6
AS 209	1.6	0.9	0.056	$9{\cdot}10^{-8}$	756	-	-	-	-	-	-	-	-	-	-
SIS	1.6	0.92	0.058	$3.7{\cdot}10^{-8}$	279	0.99	0.94	0.43	0.72	0.29	0.014	$1{\cdot}10^{-3}$	12.8	25	1.8
BES	1.6	0.96	0.068	$4.1{\cdot}10^{-8}$	293	0.83	0.67	0.49	0.73	0.20	0.014	$1{\cdot}10^{-3}$	1.6	10	1.5

Table 5.1 shows the best sets of initial conditions for SIS and BES infall in comparison to each of first eight of the 16 disk of Andrews et al. (2010). It row states first name and age of the system. Then the four physical quantities used in the comparison: mass of the star, mass of the disk, accretion rate onto the star and outer radius. For SIS and BES simulations it continues with the likelihood of the latter 4 quantities and then the total likelihood of that set of initial conditions. The last 5 columns finally show the initial condition.

Disk name /sim. type	Age [Myr]	$M_{\rm star}$ [$M_\odot$]	$M_{\rm disk}$ [$M_\odot$]	$\dot{M}_{\rm acc}$ [$M_\odot$/yr]	$R_{\rm out}$ [AU]	$L_{M_{\rm star}}$ -	$L_{M_{\rm disk}}$ -	$L_{\dot{M}_{\rm acc}}$ -	$L_{R_{\rm out}}$ -	$L_{\rm tot}$ -	α [1]	$M_{\rm wind}$ [$M_\odot$/yr]	$\Omega_{\rm cl}$ [10^{-14}s^{-1}]	$T_{\rm cl}$ [K]	$M_{\rm cl}$ [$M_\odot$]
SR 4	1.8	0.7	0.008	$6{\cdot}10^{-8}$	120	-	-	-	-	-	-	-	-	-	-
SIS	1.8	0.63	0.009	$1.1{\cdot}10^{-8}$	147	0.75	0.77	0.14	0.94	0.08	0.014	$1{\cdot}10^{-3}$	12.8	20.	1.1
BES	1.8	0.58	0.007	$9.1{\cdot}10^{-9}$	133	0.57	0.72	0.10	0.97	0.04	0.014	$1{\cdot}10^{-3}$	3.2	10	0.9
SR 24S	2.4	2.0	0.084	$3{\cdot}10^{-8}$	240	-	-	-	-	-	-	-	-	-	-
SIS	2.4	2.00	0.089	$3.3{\cdot}10^{-8}$	292	0.99	0.91	0.94	0.94	0.76	0.010	$1{\cdot}10^{-3}$	0.8	15	2.4
BES	2.4	1.93	0.082	$2.6{\cdot}10^{-8}$	270	0.90	0.96	0.90	0.97	0.75	0.008	$1{\cdot}10^{-3}$	0.4	10	2.4
WSB 60	3.0	0.3	0.042	$1{\cdot}10^{-9}$	186	-	-	-	-	-	-	-	-	-	-
SIS	3.0	0.32	0.040	$2.8{\cdot}10^{-9}$	170	0.82	0.90	0.37	0.97	0.26	0.001	$3{\cdot}10^{-4}$	12.8	20	0.4
BES	3.0	0.25	0.041	$5.4{\cdot}10^{-9}$	369	0.61	0.95	0.14	0.80	0.07	0.003	$1{\cdot}10^{-4}$	12.8	10	1.8
DoAr 25	3.8	1.0	0.272	$3{\cdot}10^{-9}$	480	-	-	-	-	-	-	-	-	-	-
SIS	3.8	1.03	0.280	$1.1{\cdot}10^{-8}$	774	0.93	0.94	0.25	0.86	0.19	0.001	$1{\cdot}10^{-5}$	12.8	40	1.3
BES	3.8	1.01	0.246	$1.2{\cdot}10^{-8}$	1725	0.98	0.82	0.23	0.64	0.12	0.003	$1{\cdot}10^{-6}$	12.8	35	1.2
DoAr 33	4.4	1.3	0.014	$3{\cdot}10^{-10}$	228	-	-	-	-	-	-	-	-	-	-
SIS	4.4	1.29	0.014	$7.9{\cdot}10^{-10}$	230	0.97	0.95	0.40	1.00	0.37	0.001	$1{\cdot}10^{-5}$	0.8	35	1.3
BES	4.4	1.25	0.013	$1.3{\cdot}10^{-9}$	384	0.89	0.82	0.20	0.85	0.13	0.003	$1{\cdot}10^{-5}$	1.6	40	1.2
SR 21	4.7	2.0	0.010	$2{\cdot}10^{-9}$	102	-	-	-	-	-	-	-	-	-	-
SIS	4.7	1.91	0.010	$2.4{\cdot}10^{-9}$	135	0.88	0.92	0.89	0.92	0.66	0.003	$3{\cdot}10^{-4}$	1.6	40	1.9
BES	4.7	1.89	0.010	$1.7{\cdot}10^{-9}$	192	0.85	0.93	0.90	0.82	0.58	0.003	$1{\cdot}10^{-4}$	0.8	35	1.8
DoAr 44	7.1	1.4	0.034	$9{\cdot}10^{-9}$	480	-	-	-	-	-	-	-	-	-	-
SIS	7.1	1.41	0.034	$1.0{\cdot}10^{-8}$	629	0.98	1.0	0.92	0.92	0.82	0.014	$3{\cdot}10^{-5}$	3.2	15	1.9
BES	7.1	1.32	0.033	$8.4{\cdot}10^{-9}$	358	0.85	0.95	0.95	0.92	0.70	0.008	$1{\cdot}10^{-4}$	3.2	15	2.1
WL 18	11.0	0.8	0.022	$9{\cdot}10^{-9}$	84	-	-	-	-	-	-	-	-	-	-
SIS	11.0	0.82	0.022	$3.1{\cdot}10^{-9}$	223	0.94	0.97	0.36	0.72	0.24	0.003	$1{\cdot}10^{-4}$	3.2	10	2.0
BES	11.0	0.82	0.023	$3.2{\cdot}10^{-9}$	223	0.95	0.96	0.36	0.72	0.24	0.003	$1{\cdot}10^{-4}$	6.4	15	1.8

Table 5.2 shows the best sets of initial conditions for SIS and BES infall in comparison to each of second eight of the 16 disk of Andrews et al. (2010). It row states first name and age of the system. Then the four physical quantities used in the comparison: mass of the star, mass of the disk, accretion rate onto the star and outer radius. For SIS and BES simulations it continues with the likelihood of the latter 4 quantities and then the total likelihood of that set of initial conditions. The last 5 columns finally show the initial condition.

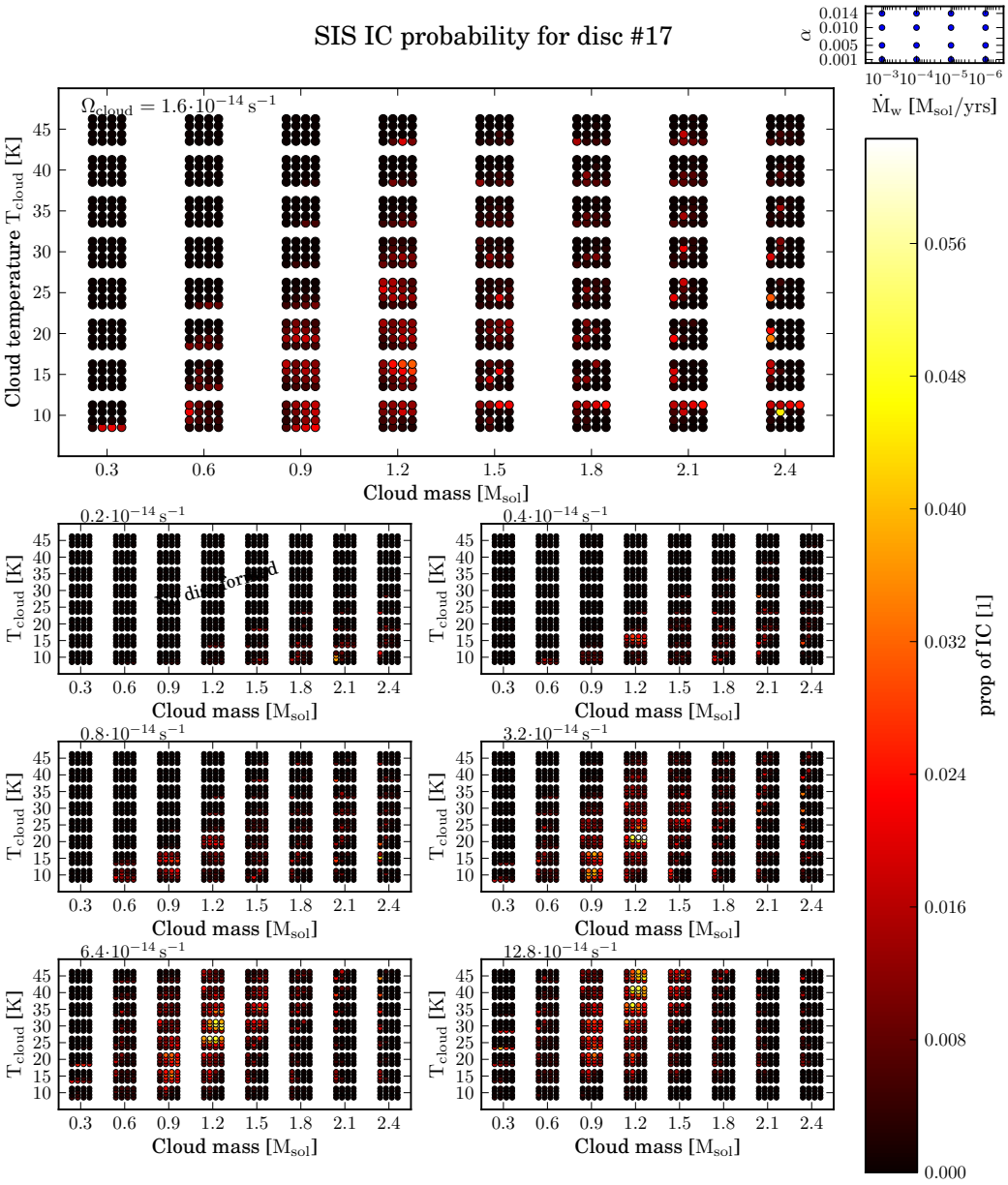

Figure 5.7 Likelihood L of disks from collapsing SIS. Each subplot shows color coded the time averaged photoevaporation for one Ω_{cl} over cloud temperature T_{cl} and mass M_{cl}. For each point of those three initial conditions a cluster of data is shown for different viscous α parameters and photo evaporation scaling factors M_{wind}. The corresponding meaning is shown in the small top right subplot. Missing dots are a sign that either the cloud collapsed completely onto the star (Initial setup found no disk; top left corner of each of the seven subplots), the disk got larger than the computational domain during infall phase (lower right corner), or an error occurred (24 simulations).

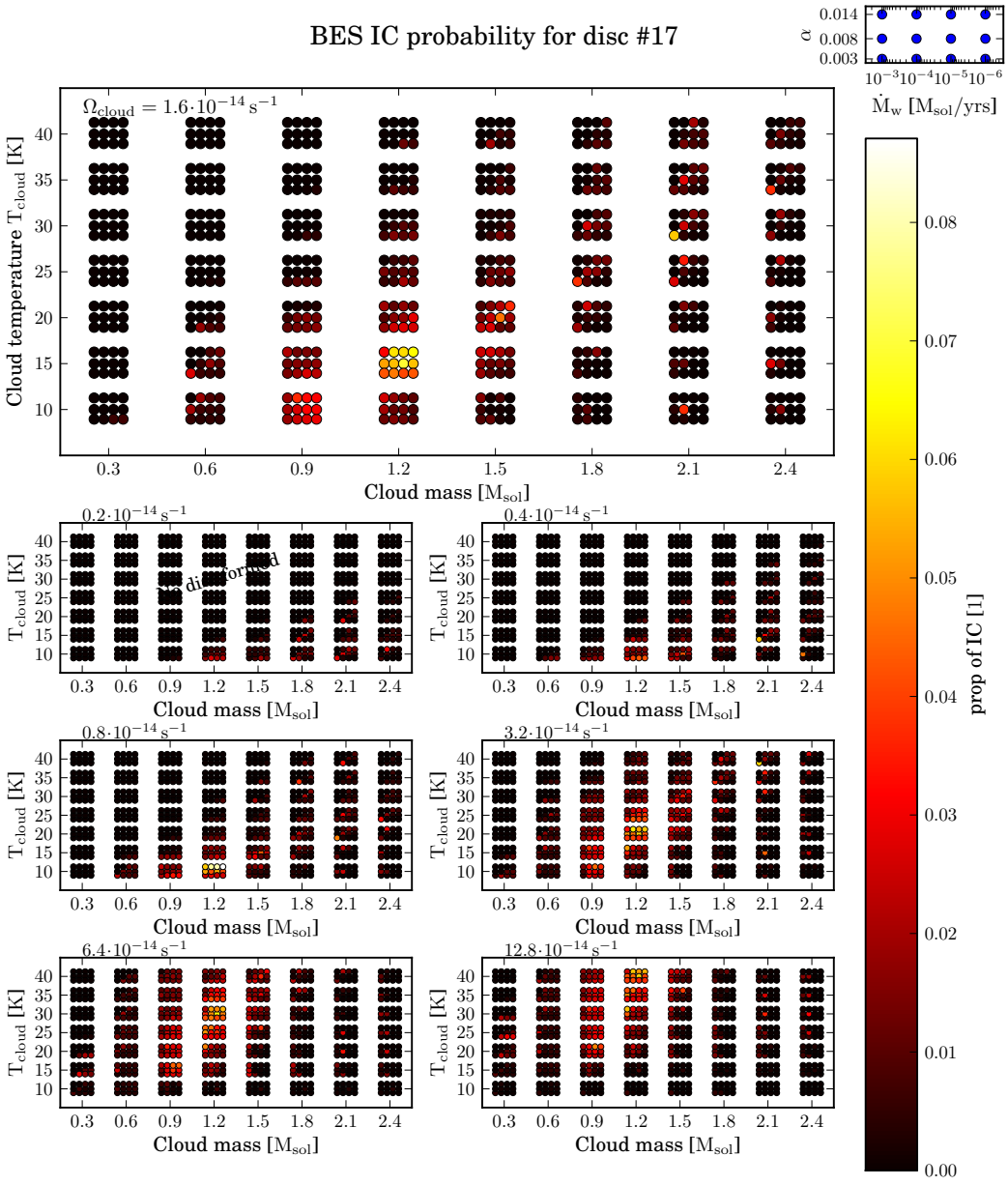

Figure 5.8 Likelihood L of disks from collapsing SIS. Each subplot shows color coded the time averaged photoevaporation for one Ω_{cl} over cloud temperature T_{cl} and mass M_{cl}. For each point of those three initial conditions a cluster of data is shown for different viscous α parameters and photo evaporation scaling factors M_{wind}. The corresponding meaning is shown in the small top right subplot. Missing dots are a sign that either the cloud collapsed completely onto the star (Initial setup found no disk; top left corner of each of the seven subplots), the disk got larger than the computational domain during infall phase (lower right corner), or an error occurred (24 simulations).

5.2.2 Likelihood of initial conditions

For the final likelihood L_i of set i of initial conditions we assume all disks described by Andrews et al. (2010) are equally common and representative of all possible disks. With this assumption we calculate

$$L_i = \sum_{j=1}^{16} \frac{L_{i,j}}{16}. \tag{5.7}$$

This likelihood of sets of initial conditions are shown for the SIS model in Figure 5.7 and for the BES model in Figure 5.8. The likelihood of a set of ICs to fit one disk perfectly and all other not at all is 1/16 or 0.0625. The maximum of the complete grid of SIS models is 0.0631, while it is 0.0623 of the shown sub grid. The maximum of the BES grid is 0.0871. This means that one set of initial conditions is fitting more than one disk of Andrews et al. (2010) on average. Using some kind of optimization scene to find the best IC should lead in both cases to even larger likelihood. Both plots show a clear peak for the likelihood and a few outliers. The peak in both cases is at $M_{\rm cl} = 1.2 M_\odot$ and for larger cloud temperatures at larger rotation frequencies, while the largest values are found for the fastest rotations. Comparing both plots, the BES model disks fit the observations in general better given the larger likelihoods. Also, comparing the likelihoods of BES or SIS models and the disk mass, the life time and the evaporation rates one sees that the most extreme cases have in general really low likelihoods.

The correlation of cloud temperature and rotation can also be seen in Figure 5.9. Here we show all possible correlations between the 5 initial conditions for the SIS model (same can be seen in Figure 5.10 for the BES simulations). The color of each dot shows the averaged likelihood of the 2 corresponding ICs. We added all likelihoods with a combination of 2 initial conditions and divided by the number of simulations of this combination with likelihood larger than zero. The reasoning for this restriction is that we do not have any information on the likelihood of e.g. sets of initial conditions that collapsed completely onto the central star without forming a disk even though we assigned them the likelihood 0. In reality at least some of those sets will exist and form stars without planets. We find strong peaks of correlations with cloud mass and rotation with at least a factor of 8 between smallest and largest value. Yet the plot of α and photoevaporation rate is almost flat with less than a factor of two between minimum and maximum. An interesting result is that faster rotating disks are hotter and hotter disks are slightly more massive ($1\,M_\odot$ at 15 K to $1.2\,M_\odot$ at 45 K). In the same figure we also show histograms of all 5 initial conditions. There is a clear peak for cloud mass at $1.1\,M_\odot$ at 0.012. Yet there is also a non zero level at 0.003. Further not flat histograms are found for the photoevaporation scaling factor $M_{\rm wind}$ (peak between 1 and $3{\cdot}10^{-}4\,M_\odot {\rm yr}^{-1}$) and rotation frequency $\Omega_{\rm cl}$ with the peak at the edge of the chosen range. A slight peak for temperature is at 20 K and α is flat except the smallest value which is less likely. Observational constraints on those quantities are a mean value of approximately $1\,M_\odot$ for clouds found by Motte et al. (1998), mean cloud temperature of 15K Jijina et al. (1999) and mean rotation frequency of $2.8{\cdot}10^{-14}{\rm s}^{-1}$ (Caselli et al., 2002). The first two mean values match the peaks found by us, yet our frequency is higher.

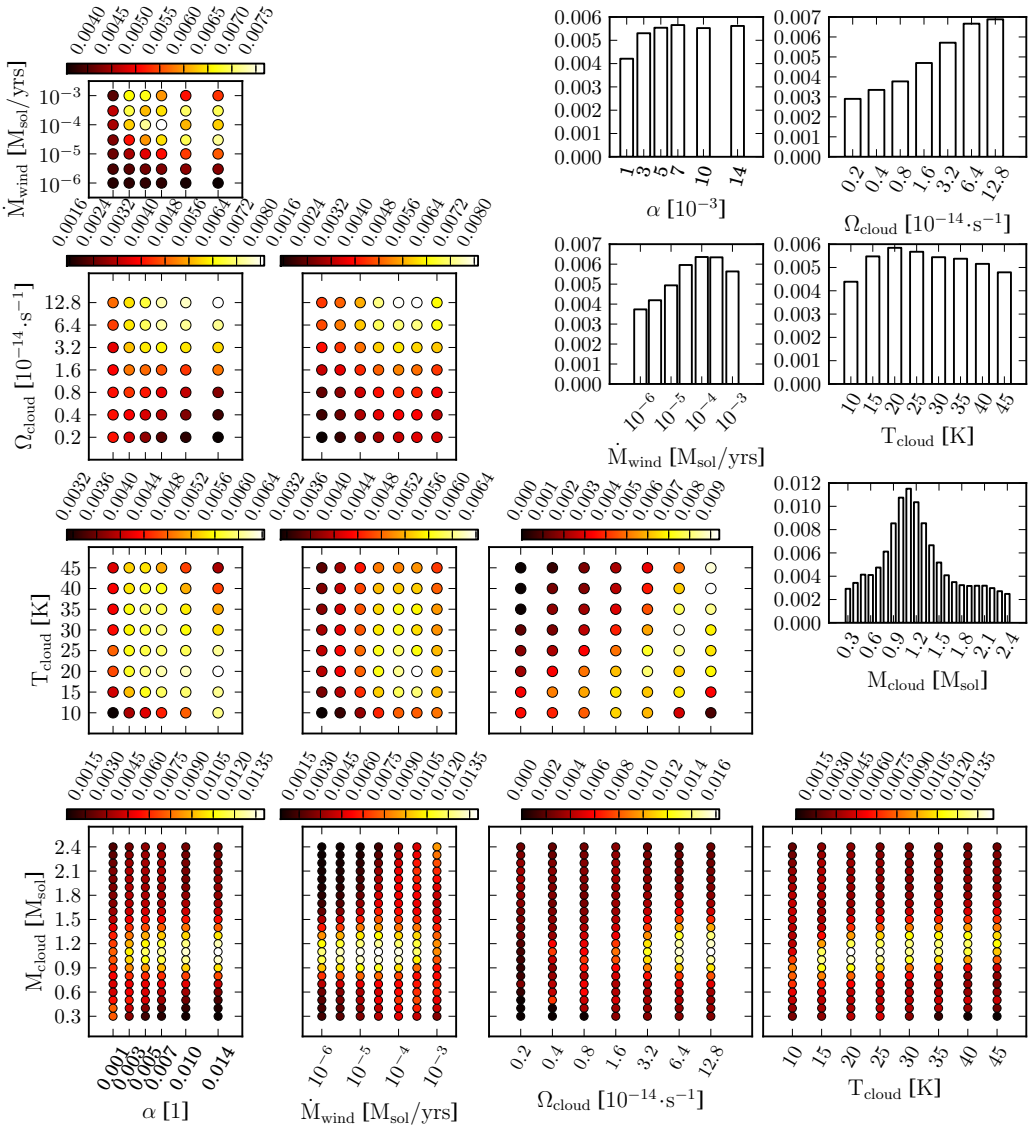

Figure 5.9 The lower left triangle shows 2D correlations of all 5 initial conditions of the SIS models. Color coded is the averaged likelihood of all sets of initial conditions with the given values on the axes of the sub plots. The top right shows 1D histograms of the 5 initial conditions.

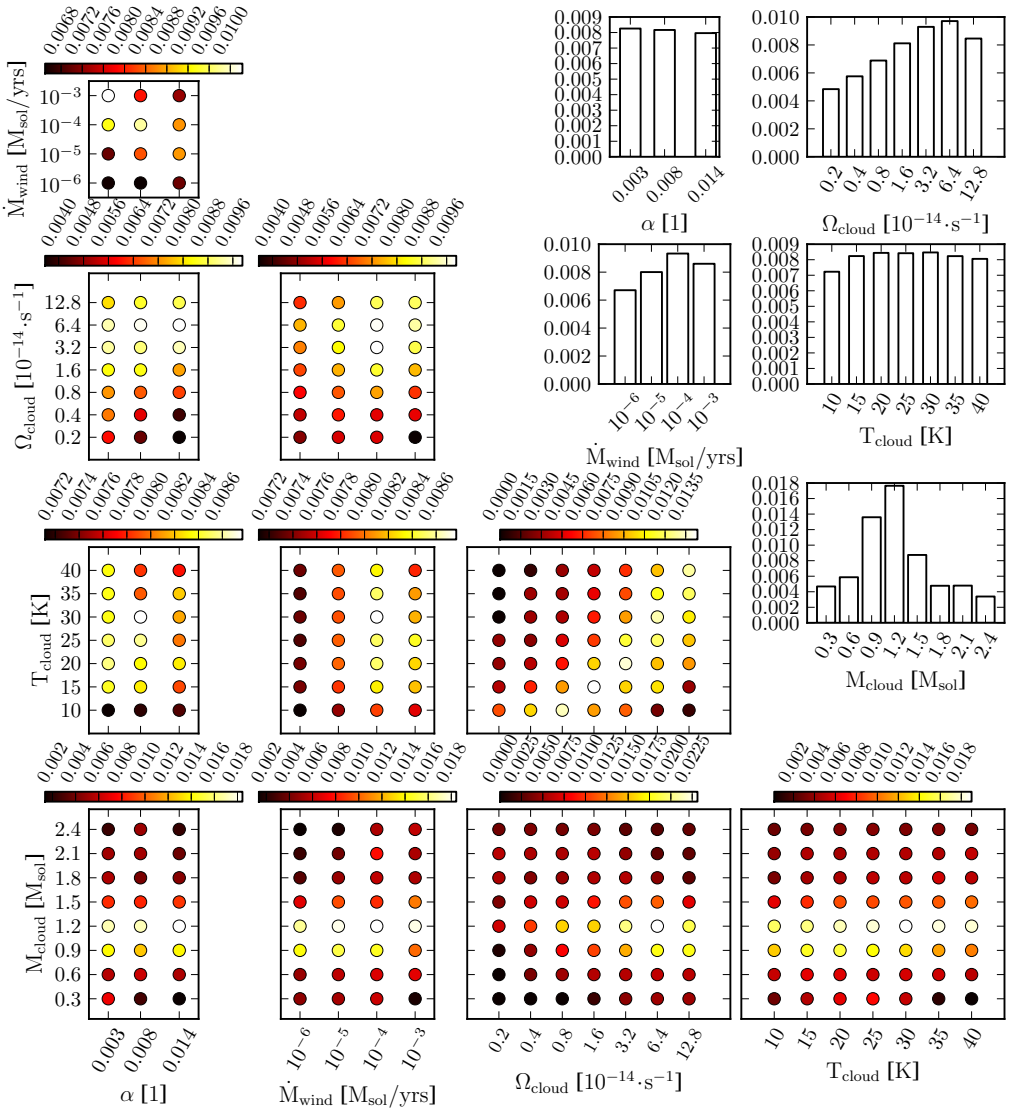

Figure 5.10 The lower left triangle shows 2D correlations of all 5 Initial conditions of the BES models. Color coded is the averaged likelihood of all sets of initial conditions with the given values on the axes of the sub plots. The top right shows 1D histograms of the 5 initial conditions.

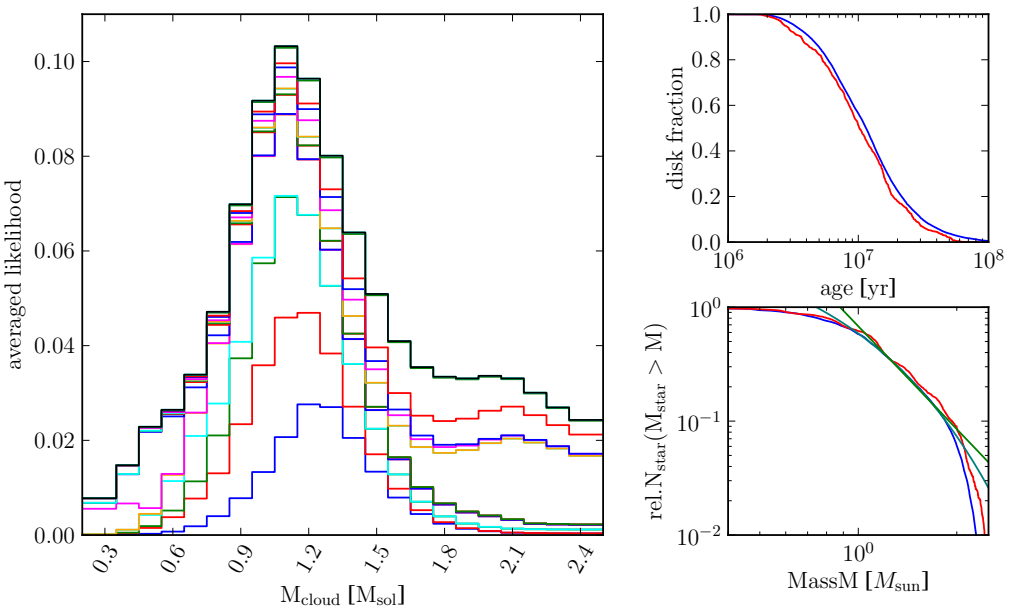

Figure 5.11 Left panel shows the cloud mass histogram of the SIS model. Colored lines are the contributions of the likelihoods for the 16 different disks. Top right panel shows the disk fraction of both SIS and BES model. Lower right panel shows relative number of stars larger than a certain star mass over star mass for both models.

Our grid for the BES case is much smaller than the one for SIS. Therefore, the correlations in Figure 5.10 are not as clear as in Figure 5.9. Nevertheless, most are similar as described above while the averaged likelihoods are overall larger. The histogram of α is completely flat showing not clear preference for one of the 3 values. Also comparing different correlations show diverging information on some quantities. Photoevaporation - α correlation suggests an α of 0.003 while the cloud mass - α correlation has the maximum at the largest α. Similar can be said for e.g. temperature. The whole information is only found using the complete not reduced grid. This will be used in the future when we create the initial condition lists for planet population synthesis calculations.

The most distinguished histogram is cloud mass in the SIS model. The left panel of Figure 5.11 shows this histogram again. Yet each value is split up for the different 16 disks illustrating the different parts each disk contributes to. The central peak is not dominated by one single really well fit disk but made by 4 to 5 different. Also the flat part at the larger masses is made up by 3 disks. Also some disks do not contribute much anywhere. The top right panel of Figure 5.11 shows the disk fractions over age of a system for both models. After $\approx$ 10Myr in both cases half the disks are gone. This is much longer than observed disk fractions (Mamajek, 2009; Haisch et al., 2001). The bottom right panel shows the relative number of stars larger than a certain star mass over that star mass for both models. There is a linear part in the double logarithmic plot between 1 and $2M_\odot$, which is fitted by hand with two functions:

$$n_1(m) = 4.7 \exp(-2.08m) \tag{5.8}$$

and

$$n_2(m) = 0.68m^{-3}. \tag{5.9}$$

This is different from predictions by the IMF which suggests an exponent of ≈ -1.3 in the second function.

Chapter 6

Discussion, Summary and Outlook

In this chapter, we will first give a discussion and brief summary of the previous chapters before we give an outlook what else can be done now.

6.1 Discussion and Summary

In Chapter 2 we presented a description of a migration model for one planet in a proto planetary disk. It connected new results on type I migration, namely outward migration for some ranges of planet mass and semimajor axis, to an older description of type II migration. The type I migration model divided the regime into four different modes, combinations of saturated and unsaturated corotation torques and locally isothermal and adiabatic migration. The last combination, unsaturated adiabatic corotation torques lead to outward migration of planets while the other three induce inward movement of the planet for normal disk parameters. Which mode describes type I migration best at a given point in planet mass and semimajor axis depends on ratios of timescales, while the direction depends on the slopes of temperature and surface density.

One feature of the introduction of that outward migration was the occurrence of convergence zones (CZ) between inward and outward migration regions. While thus are only present when the planet migration is in the unsaturated adiabatic mode. We could show by the increase in the number of cold planets by More than a factor that this new migration model overcame the problem of only fast inward migration of small planets x. The latter made the introduction of an artificial fudge factor necessary, which reduced the old type I migration rate by a factor of 1000 (Mordasini et al., 2009a). We presented planet population synthesis calculations using the new migration model and stated the distributions between cold and hot and small and massive planets. Yet one problem with this populations was the absence of large planets outside of 5 AU. Nevertheless, the CZ could explain the clustering found in the semimajor axis - mass diagram of the observed population.

At the same time all those simulations where done with in principle the same one disk around a one solar mass star. Different starting values of Σ only determine, after

the initial settling phase, the point at which the simulation entered this disk evolution.This resulted in the same position of the CZ for a given disk mass. Also the fixed inner boundary at 0.1 AU prevented any conclusions on the real number of hot planets. To overcome this we needed a new disk evolution model which extends to the real inner boundary and is more flexible than the old one. This new model is presented in Chapter 3 and Chapter 4. Chapter 3 introduced the temperature model used to calculate the midplane temperature. It is more crude than the fully vertically integrated model used in the disk model of chapter 2, yet more flexible. We used our temperature model to create a lookup table for all important quantities like midplane temperature or pressure scale height that only depends on surface density, temperature at the radiative surface and Keplerian frequency. Comparison with the old model show an acceptable match for the 2 surface density profiles chosen. One potential improvement would be a better calculation of τ_{eff} with more than two temperatures. Nevertheless, the model gives temperatures for a wide range of parameters and is therefore usable in our disk model.

Chapter 4 is about the disc model itself and its different parts. We incorporated an infall model to build up the disk and do not start with an arbitrary intial state. We included a stellar evolution model to account for the changing star mass and therefore the changing properties like effective temperature. Our model consists at the moment of public available pre main sequence star evolution tracks from Siess et al. (2000).

Yet Yorke and Bodenheimer (2008) show that evolution tracks of accreting stars differ from those calculated with constant mass. We also included a flexible inner edge depending on stellar radius, magnetic field, which is fixed, and accretion rate onto the star. And as in the previous model we included photoevaporation as an external mass tool to remove mass from the disk without accreting it onto the star. In the second part of Chapter 4 we discussed in detail the evolution of two disks and showed the evolution of a small set of disks. For both disks we also showed the migration profile for unsaturated adiabatic migration. We found 2 long living convergence zones in the new model as we did in the old. They will stop planet migration for some time as we have shown in Chapter 2.

Furthermore, also the inner edge functions as an convergence zone. Yet the gradients are so step that it will not only stop unsaturated type I migration but probably all types of type I migration if the formalism of Chapter 2 or Paardekooper et al. (2011) is also valid there. Also type II migraton planets could be stop by the inner edge as shown by Benítez-Llambay et al. (2011). In our model the inner edge is between 0.01 and 0.1 AU for the largest part of the disk evolution. Yet at the end before the disk vanishes it moves outward, at that point it could take planets with it depending on planet mass and speed of retreat of the inner edge.

In Chapter 5 we study a grid of sets of initial conditions. We shot the range of disk masses and lifetimes for the observationally constrained rangesof initial conditions of the infalling clouds. We also compare the disks obtained with the sets of initial conditions with disks characterized by Andrews et al. (2010) to determine likelihood of those sets. We find for the infall of SIS clear peaks in the distribution of cloud mass and temperature which agree with the mean values found in observations. The maximum in the distribution of the cloud rotation frequency lies at the upper border

of our range. For SIS we see a slight drop for the largest frequency while in the BES case larger frequencies could be even more likely. The large frequency leads to a large amount of gas being deposited onto the disk far from the star. This results in longer lifetimes, higher photoevaporation rates and more dust placed farther away. Studies on the evolution and growth of dust grains suggests that one need a large depot of material in the outer regions to explain the amount of small grains observed (Testi et al., 2014). Yet as the disk fraction in both models show, the lifetimes of the disk are too long, although we have relatively large photo evaporation rates and viscous α is also large. Reaching short disk lifetimes and still large disks is not possible with both chosen infall models, with BES model being the better of the two (larger radii at the end of infall phase, better fits to Andrews et al. (2010) disks). Our distribution of star masses does not fit the IMF at all. This is expected because we ignore all those clouds that formed no disk. Also the observed population of the 16 stars do not represent the IMF, so by matching thus disks we can not obtain the IMF.

Nevertheless we did obtain likelihoods for the whole range of initial conditions we studied, which can be used to create a list of sets of initial conditions to be used by planet population synthesis calculations.

6.2 Outlook

Further analysis of the data will include distribution of the position of the centrifugal radius at the end of infalling phase. This will give further confirmation that the BES models deposit more gas further out than the SIS models. Future work on this new disk model will include the implementation of the accretion luminosity of the matter falling onto the star from the cloud (Visser et al., 2009) and from the disk. This should give larger surface temperatures and therefore larger midplane temperatures in the disk, which will result in higher accretion rates and lower disk lifetimes. Also the implementation of cylindrical infall models as a third infall model can be done to see if this will give more realistic life times (Myers, 2005, 2008). Before we can use the disk model for planet population synthesis calculations model we have to combine it with a model that simulates the growth of the planetesimal disk like Birnstiel et al. (2010).

Appendix A

Numercial strategy for approximated temperature model

We will present here the numerical strategy used to calculate the midplane temperature on the fly for the approximated temperature model.

We start with $\hat{T}_0$,$\hat{P}_0$ and $\hat{H}_s$,$\hat{P}_s$ from the previous step (marked with a ˆ):

1. Calculate the irradiation luminosity L_{irr} for the whole grid. (Eq. 3.6, use $H = \hat{H}_s$), smooth it with 4.7.
2. Calculate γ for the whole grid out of $\hat{T}_0$,$\hat{P}_0$, smooth it with 4.5. (currently we use $\gamma = 1.4$)
3. Use Equation 3.7 to get T_s.
4. Use Equation 3.11 and $T = T_s$ to get isothermal surface pressure scale height $H_{iso,s}$.
5. Calculate an initial surface density $\rho_s = \frac{\hat{P}_s}{k_B/mT_s}$.
6. We calculate an initial surface opacity κ_s out of ρ_s and T_s.
7. With this we calculate a new ρ_s out of the old $\hat{H}_s$ and the ρ_s from 2 steps before (modified Equation 3.43):

$$\rho_s = 0.5\rho_s + 0.5\tau_s \frac{H_s}{H_{iso}^2 \kappa_s} \tag{A.1}$$

   and use this new density to get a new opacity.
8. We iterate step 6 and 7 a few times.
9. This we now use to iterate Equation 3.47 and steps 6 and 7. If the change between the new and the old H_s is small enough we stop the iteration.
10. Use Approximation 3.15 to get P_s.

11. Use Equation 3.28 to get H_A.
12. Use Equation 3.21 to get T_A and similarily Equation 3.20 and 3.22 to get P_A and ρ_A.
13. With H_s we can also get isothermal midplane values $\rho_{0,iso}$ (Equation 3.9) and calculate $P_{0,iso} = \frac{k_B}{\mu} T_s \rho_{0,iso}$.
14. Now we also calculate the radiative midplane values. We use Equation 3.36 and iterate until the temperature we use to calculate the midplane opacity and the radiative midplane temperature are the same.
15. At a last step we compare T_{rad} and T_A and use the smaller one as T_0 and update P_0 ackordingly.
16. Finally we smooth the new T_0,P_0 and H_s (With 4.7), calculate a new H_{iso} (Equation 3.11).

Appendix B

Derivation of the Solver

In this appendix we derive the implicit equations used in the solver for the evolution equation of the disc surface density.

B.1 Evolution equation

We want to calculate numerically the evolution of a protostellar disc. The equation describing the radial evolution of the surface density Σ of a axis symmetric flat disc is (Equation (4.1)):

$$f(\Sigma) = \frac{\partial}{\partial t}\Sigma = \frac{3}{a}\frac{\partial}{\partial a}\sqrt{a}\frac{\partial}{\partial a}\nu\Sigma\sqrt{a} - \frac{2}{a}\frac{\partial}{\partial a}\frac{\dot{h}\Sigma}{\Omega} + \dot{Q}_w = \frac{4.5}{a}\frac{\partial}{\partial a}\nu\Sigma + 3\frac{\partial^2}{\partial a^2}\nu\Sigma - \frac{2}{a}\frac{\partial}{\partial a}\frac{\dot{h}\Sigma}{\Omega} + \dot{Q}_w \tag{B.1}$$

This equation already assumes $\Omega = \sqrt{\frac{GM_{\text{star}}}{a^3}}$ which is not completely valid close to the star. Also if the disc contains considerable mass effects of self gravity can lead to derivations of this. We neglected all thus effects.

Some notation conventions:
X_i will be quantity X at the grid cell i and X^n at time t_n Spacial derivatives are transformed by

$$\frac{\partial}{\partial x}X_i = (X_{i+1} - X_{i-1})/(2\Delta x) \tag{B.2}$$

and

$$\frac{\partial^2}{\partial x^2}X_i = (X_{i+1} - 2X_i + X_{i-1})/(\Delta X^2). \tag{B.3}$$

and time derivatives by setting X_i in the middle of the old and new timestep

$$X_i = 0.5(X_i^n + X_i^{n+1}) \tag{B.4}$$

$$\frac{\partial}{\partial t}X_i = (X_i^{n+1} - X_i^n)/\Delta t \tag{B.5}$$

to transform differential equations into linear equations.Here Δx is the distance between 2 gridcells and Δt the difference between two timesteps.

Our grid is uniform in log so we make a base transition: $x = ln(a) <=> a = e^x$ and $\frac{\partial}{\partial x} a = e^x = a$

This transforms the equation we want to solve as follows:

$$\frac{\partial}{\partial t}\Sigma = \frac{3}{e^{2x}}\frac{\partial}{\partial x}e^{-x/2}\frac{\partial}{\partial x}\alpha C_s^2\frac{\Sigma}{\Omega}e^{x/2} - \frac{2}{e^{2x}}\frac{\partial}{\partial x}\dot{h}\frac{\Sigma}{\Omega} + \dot{Q}_w \tag{B.6}$$

$$= \frac{3}{2e^{2x}}\frac{\partial}{\partial x}\alpha C_s^2\frac{\Sigma}{\Omega} + \frac{3}{e^{2x}}\frac{\partial^2}{\partial x^2}\alpha C_s^2\frac{\Sigma}{\Omega} - \frac{2}{e^{2x}}\frac{\partial}{\partial x}\dot{h}\frac{\Sigma}{\Omega} + \dot{Q}_w \tag{B.7}$$

B.2 Solver: Crank - Nicholson

We use the new variable

$$\hat{\Sigma} = \Sigma/\Omega \tag{B.8}$$

since it appears on all terms with the surface density on the right hand side.

$$\Omega\frac{\partial}{\partial t}\hat{\Sigma} = \frac{3}{2e^{2x}}\frac{\partial}{\partial x}\alpha C_s^2\hat{\Sigma} + \frac{3}{e^{2x}}\frac{\partial^2}{\partial x^2}\alpha C_s^2\hat{\Sigma} - \frac{2}{e^{x}}\frac{\partial}{\partial x}\dot{h}\hat{\Sigma} + \dot{Q}_w \tag{B.9}$$

Now we can split the partial derivatives

$$\begin{aligned}\Omega\frac{\partial}{\partial t}\hat{\Sigma} = \frac{3}{2e^{2x}}&(\hat{\Sigma}\frac{\partial}{\partial x}\alpha C_s^2 + \alpha C_s^2\frac{\partial}{\partial x}\hat{\Sigma}) \\ &+ \frac{3}{e^{2x}}(\hat{\Sigma}\frac{\partial^2}{\partial x^2}\alpha C_s^2 + 2(\frac{\partial}{\partial x}\alpha C_s^2)(\frac{\partial}{\partial x}\hat{\Sigma}) + \alpha C_s^2\frac{\partial^2}{\partial x^2}\hat{\Sigma}) \\ &- \frac{2}{e^{2x}}(\hat{\Sigma}\frac{\partial}{\partial x}\dot{h} + \dot{h}\frac{\partial}{\partial x}\hat{\Sigma}) + \dot{Q}_w\end{aligned} \tag{B.10}$$

and collect the different derivatives of $\hat{\Sigma}$

$$\begin{aligned}= \dot{Q}_w + (&\frac{3}{2e^{2x}}\frac{\partial}{\partial x}\alpha C_s^2 + \frac{3}{e^{2x}}\frac{\partial^2}{\partial x^2}\alpha C_s^2 - \frac{2}{e^{2x}}\frac{\partial}{\partial x}\dot{h})\hat{\Sigma} \\ &+ (\frac{3}{2e^{2x}}\alpha C_s^2 + \frac{6}{e^{2x}}(\frac{\partial}{\partial x}\alpha C_s^2) + \frac{2}{e^{2x}}\dot{h})\frac{\partial}{\partial x}\hat{\Sigma} + \frac{3}{e^{2x}}\alpha C_s^2\frac{\partial^2}{\partial x^2}\hat{\Sigma}.\end{aligned} \tag{B.11}$$

The equation we what to solve is of the kind of

$$\frac{\partial}{\partial t}X = a_0 + a_1 X + a_2\frac{\partial}{\partial x}X + a_3\frac{\partial^2}{\partial x^2}X \tag{B.12}$$

with $X = \hat{\Sigma}$,$a_0 = \dot{Q}_w\Omega^{-1}$, $a_1 = (\frac{3}{2e^{2x}}\frac{\partial}{\partial x}\alpha C_s^2 + \frac{3}{e^{2x}}\frac{\partial^2}{\partial x^2}\alpha C_s^2 - \frac{2}{e^{2x}}\frac{\partial}{\partial x}\dot{h})\Omega^{-1}$, $a_2 = (\frac{3}{2e^{2x}}\alpha C_s^2 + \frac{6}{e^{2x}}(\frac{\partial}{\partial x}\alpha C_s^2) + \frac{2}{e^{2x}}\dot{h})\Omega^{-1}$, and $a_4 = \frac{3}{e^{2x}}\alpha C_s^2\Omega^{-1}$

We will now use Equation (B.2) and Equation (B.3) to get rid of the spacial derivatives

$$\frac{\partial}{\partial t}X = a_0 + a_1 X_i + a_2(X_{i+1} - X_{i-1})/(2\Delta x) + a_3(X_{i+1} - 2X_i + X_{i-1})/(\Delta x^2) \quad \text{(B.13)}$$

In this equation we will not sort X by gridcells:

$$\frac{\partial}{\partial t}X = a_0 + X_{i-1}(-a_2/(2\Delta x) + a_3/\Delta x^2) + X_i(a_1 - 2a_3/\Delta x^2) + X_{i+1}(a_2/(2\Delta x) + a_3/\Delta x^2) \quad \text{(B.14)}$$

And finally use Equation (B.4) and Equation (B.5) to remove the time derivatives:

$$\begin{aligned}(X_i^{n+1} - X_i^n)/\Delta t = a_0 &+ (X_{i-1}^n + X_{i-1}^{n+1})(-a_2/(4\Delta x) + a_3/(2\Delta x^2)) + \\ &(X_i^n + X_i^{n+1})(a_1/2 - a_3/\Delta x^2) + (X_{i+1}^n + X_{i+1}^{n+1})(a_2/(4\Delta x) + a_3/(2\Delta x^2)) \quad \text{(B.15)}\end{aligned}$$

We multiply by Δt and bring old timestep terms on one side and new timestep terms on the other:

$$\begin{aligned}&X_{i-1}^{n+1}(a_2\Delta t/(4\Delta x) - a_3\Delta t/(2\Delta x^2)) + X_i^{n+1}(1 - a_1\Delta t/2 + a_3\Delta t/\Delta x^2) \\ &+ X_{i+1}^{n+1}(-a_2\Delta t/(4\Delta x) - a_3\Delta t/(2\Delta x^2)) = a_0\Delta t + X_{i-1}^n(-a_2\Delta t/(4\Delta x) + a_3\Delta t/(2\Delta x^2)) \\ &+ X_i^n(1 + a_1\Delta t/2 - a_3\Delta t/\Delta x^2) + X_{i+1}^n(a_2\Delta t/(4\Delta x) + a_3\Delta t/(2\Delta x^2)) \quad \text{(B.16)}\end{aligned}$$

We identify the three terms

$$\begin{aligned}D_1 &= a_2\Delta t/(4\Delta x) - a_3\Delta t/(2\Delta x^2) \\ D_2 &= 1 - a_1\Delta t/2 + a_3\Delta t/\Delta x^2 \\ D_3 &= -a_2\Delta t/(4\Delta x) - a_3\Delta t/(2\Delta x^2) \quad \text{(B.17)}\end{aligned}$$

to get.

$$D_1\hat{\Sigma}_{i-1}^{n+1} + \hat{\Sigma}_i^{n+1}(D_2) + D_3\hat{\Sigma}_{i+1}^{n+1} = a_0\Delta t - D_1\hat{\Sigma}_{i-1}^n + \hat{\Sigma}_i^n(2 - D_2) - D_3\hat{\Sigma}_{i+1}^n \quad \text{(B.18)}$$

This equation is of the form

$$M\hat{\vec{\Sigma}}^{n+1} = \vec{b} \quad \text{(B.19)}$$

with M being a tridiagonal matrix and b a vector of only old quantities. The fastest way to solve this equation is *forward elimination/backward substitution* which we use. As a remark, this solver is not mass conserving by constructions, yet it is conserved in most cases.

B.2.1 Inner Boundary without planetary torque

Yet this equation has $n + 2$ unknowns for n equations. Thus, to close the n equations above we have to specify boundary conditions. We do this as following:

Mass flux at position a is

$$\dot{M} = -6\pi\sqrt{a}\frac{\partial}{\partial a}\nu\Sigma\sqrt{a} \quad \text{(B.20)}$$

We assume that mass flux is constant in time during a timestep at the inner boundary

$$\dot{M}_1^{n+1} = \dot{M}_1^n \tag{B.21}$$

$$\frac{\partial}{\partial a}\alpha C_s^2 \hat{\Sigma}_1^n \sqrt{a} = \frac{\partial}{\partial a}\alpha C_s^2 \hat{\Sigma}_1^{n+1} \sqrt{a} \tag{B.22}$$

Again transforming onto the logarithmic grid

$$\frac{\partial}{\partial x}\alpha C_s^2 \hat{\Sigma}_1^n e^{x/2} = \frac{\partial}{\partial x}\alpha C_s^2 \hat{\Sigma}_1^{n+1} e^{x/2}, \tag{B.23}$$

spliting the derivatives

$$\hat{\Sigma}_1^n \frac{\partial}{\partial x}\alpha C_s^2 e^{x/2} + \alpha C_s^2 e^{x/2} \frac{\partial}{\partial x}\hat{\Sigma}_1^n = \hat{\Sigma}_1^{n+1} \frac{\partial}{\partial x}\alpha C_s^2 e^{x/2} + \alpha C_s^2 e^{x/2} \frac{\partial}{\partial x}\hat{\Sigma}_1^{n+1} \tag{B.24}$$

and substituting the important derivatives by Equation (B.2).

$$= \hat{\Sigma}_1^{n+1} \frac{\partial}{\partial x}\alpha C_s^2 e^{x/2} + \alpha C_s^2 e^{x/2} (\hat{\Sigma}_2^{n+1} - \hat{\Sigma}_0^{n+1}) / (2\Delta x) \tag{B.25}$$

Finally we separate the unknown $\hat{\Sigma}_0^{n+1}$

$$\hat{\Sigma}_0^{n+1} = -2\Delta x \hat{\Sigma}_1^n \frac{1}{\alpha C_s^2 e^{x/2}} \frac{\partial}{\partial x}\alpha C_s^2 e^{x/2} - \hat{\Sigma}_2^n + \hat{\Sigma}_0^n + 2\Delta x \hat{\Sigma}_1^{n+1} \frac{1}{\alpha C_s^2 e^{x/2}} \frac{\partial}{\partial x}\alpha C_s^2 e^{x/2} + \hat{\Sigma}_2^{n+1} \tag{B.26}$$

Reintroducing Equation (B.18) for the first grid cell $i = 1$, substituting $\hat{\Sigma}_0^{n+1}$ and sorting all $\hat{\Sigma}$ we get:

$$\begin{aligned}
&(D_2 + D_1 \frac{\alpha C_{s,2}^2 e^{x_2/2} - \alpha C_{s,0}^2 e^{x_0/2}}{\alpha C_{s,1}^2 e^{x_1/2}}) \hat{\Sigma}_1^{n+1} + (D_1 + D_3) \hat{\Sigma}_2^{n+1} \\
&= a_0 \Delta t - 2D_1 \hat{\Sigma}_0^n + \hat{\Sigma}_1^n (2 - D_2 + D_1 \frac{\alpha C_{s,2}^2 e^{x_2/2} - \alpha C_{s,0}^2 e^{x_0/2}}{\alpha C_{s,1}^2 e^{x_1/2}}) + (D_1 - D_3) \hat{\Sigma}_2^n
\end{aligned} \tag{B.27}$$

This gives us a new first line for matrix M and vector $\vec{b}$.

B.2.2 Inner and Outer Boundary with Planetary Torque

Since we also included a interaction term between a planet and the disk we will now do the same as above with the planet disk interaction $\dot{h}$ included into the equation of the mass flux.

$$\dot{M} = -6\pi\sqrt{a} \frac{\partial}{\partial a} \nu \Sigma \sqrt{a} + 4\pi \frac{\dot{h}\Sigma}{\Omega} \tag{B.28}$$

we follow the steps above to derive:

$$\begin{aligned}
&\left(D_2 + D_1 \left(\frac{\alpha C_{s,2}^2 e^{x_2/2} - \alpha C_{s,0}^2 e^{x_0/2}}{\alpha C_{s,1}^2 e^{x/2}} - \frac{4\Delta x}{3\alpha C_{s,1}^2} \dot{h} \right) \right) \hat{\Sigma}_1^{n+1} + (D_1 + D_3) \hat{\Sigma}_2^{n+1} \\
&= a_0 \Delta t - 2D_1 \hat{\Sigma}_0^n + \hat{\Sigma}_1^n \left(2 - D_2 + D_1 \left(\frac{\alpha C_{s,2}^2 e^{x_2/2} - \alpha C_{s,0}^2 e^{x_0/2}}{\alpha C_{s,1}^2 e^{x/2}} - \frac{4\Delta x}{3\alpha C_{s,1}^2} \dot{h} \right) \right) + (D_1 - D_3) \hat{\Sigma}_2^n
\end{aligned} \tag{B.29}$$

Similarly for the outer boundary we get:

$$\left(D_2 - D_3\left(\frac{\alpha C_{s,n+1}^2 e^{x_{n+1}/2} - \alpha C_{s,n-1}^2 e^{x_{n-1}/2}}{\alpha C_{s,n}^2 e^{x_n/2}} - \frac{4\Delta x}{3\alpha C_{s,n}^2}\dot{h}_n\right)\right)\hat{\Sigma}_n^{n+1} + (D_1 + D_3)\,\hat{\Sigma}_{n-1}^{n+1}$$
$$= a_0\Delta t - (D_1 - D_3)\hat{\Sigma}_{n-1}^{n}$$
$$+ \hat{\Sigma}_n^n\left(2 - D_2 - D_3\left(\frac{\alpha C_{s,n+1}^2 e^{x_{n+1}/2} - \alpha C_{s,n-1}^2 e^{x_{n-1}/2}}{\alpha C_{s,n}^2 e^{x_n/2}} - \frac{4\Delta x}{3\alpha C_{s,n}^2}\dot{h}_n\right)\right) - 2D_3\hat{\Sigma}_{n+1}^n \tag{B.30}$$

Bibliography

Adams, F. C., Proszkow, E. M., Fatuzzo, M., and Myers, P. C. (2006). Early Evolution of Stellar Groups and Clusters: Environmental Effects on Forming Planetary Systems. *ApJ*, 641:504–525.

Alexander, R. (2014). Planet formation in evolving protoplanetary discs. In Booth, M., Matthews, B. C., and Graham, J. R., editors, *IAU Symposium*, volume 299 of *IAU Symposium*, pages 179–189.

Alexander, R. D. and Armitage, P. J. (2009). Giant Planet Migration, Disk Evolution, and the Origin of Transitional Disks. *ApJ*, 704:989–1001.

Alibert, Y., Carron, F., Fortier, A., Pfyffer, S., Benz, W., Mordasini, C., and Swoboda, D. (2013). Theoretical models of planetary system formation: mass vs. semi-major axis. *A&A*, 558:A109.

Alibert, Y., Mordasini, C., and Benz, W. (2004). Migration and giant planet formation. *A&A*, 417:L25.

Alibert, Y., Mordasini, C., and Benz, W. (2011). Extrasolar planet population synthesis. III. Formation of planets around stars of different masses. *A&A*, 526:A63.

Alibert, Y., Mordasini, C., Benz, W., and Winisdoerffer, C. (2005). Models of giant planet formation with migration and disc evolution. *A&A*, 434:343.

Andrews, S. M., Wilner, D. J., Hughes, A. M., Qi, C., and Dullemond, C. P. (2010). Protoplanetary Disk Structures in Ophiuchus. II. Extension to Fainter Sources. *ApJ*, 723:1241–1254.

Armitage, P. J. (2007). Massive planet migration: Theoretical predictions and comparison with observations. *The Astrophysical Journal*, 665:1381.

Armitage, P. J. and Clarke, C. J. (1996). Magnetic braking of T Tauri stars. *MNRAS*, 280:458–468.

Armitage, P. J. and Rice, W. K. M. (2005). Planetary migration. *STScI Symposium A Decade Of Extrasolar Planets Around Normal Stars*.

Baruteau, C. and Masset, F. (2008). On the Corotation Torque in a Radiatively Inefficient Disk. *ApJ*, 672:1054–1067.

Batalha, N. M., Borucki, W. J., Bryson, S. T., Buchhave, L. A., Caldwell, D. A., Christensen-Dalsgaard, J., Ciardi, D., Dunham, E. W., Fressin, F., Gautier, III, T. N., Gilliland, R. L., Haas, M. R., Howell, S. B., Jenkins, J. M., Kjeldsen, H., Koch, D. G., Latham, D. W., Lissauer, J. J., Marcy, G. W., Rowe, J. F., Sasselov, D. D., Seager, S., Steffen, J. H., Torres, G., Basri, G. S., Brown, T. M., Charbonneau, D., Christiansen, J., Clarke, B., Cochran, W. D., Dupree, A., Fabrycky, D. C., Fischer, D., Ford, E. B., Fortney, J., Girouard, F. R., Holman, M. J., Johnson, J., Isaacson, H., Klaus, T. C., Machalek, P., Moorehead, A. V., Morehead, R. C., Ragozzine, D., Tenenbaum, P., Twicken, J., Quinn, S., VanCleve, J., Walkowicz, L. M., Welsh, W. F., Devore, E., and Gould, A. (2011). Kepler's First Rocky Planet: Kepler-10b. *ApJ*, 729:27.

Bell, K. R. and Lin, D. N. C. (1994). Using FU Orionis outbursts to constrain self-regulated protostellar disk models. *ApJ*, 427:987–1004.

Benítez-Llambay, P., Masset, F., and Beaugé, C. (2011). The mass-period distribution of close-in exoplanets. *A&A*, 528:A2.

Birnstiel, T., Dullemond, C. P., and Brauer, F. (2010). Gas- and dust evolution in protoplanetary disks. *A&A*, 513:A79.

Bitsch, B. and Kley, W. (2011). Range of outward migration and influence of the disc's mass on the migration of giant planet cores. *A&A*, 536:A77.

Blabla, B. (20xx). *A&A*, page in review.

Bodenheimer, P., D'Angelo, G., Lissauer, J. J., Fortney, J. J., and Saumon, D. (2013). Deuterium Burning in Massive Giant Planets and Low-mass Brown Dwarfs Formed by Core-nucleated Accretion. *ApJ*, 770:120.

Boss, A. P. (1997). Giant planet formation by gravitational instability. *Science*, 276:1836–1839.

Campante, T. L., Barclay, T., Swift, J. J., Huber, D., Adibekyan, V. Z., Cochran, W., Burke, C. J., Isaacson, H., Quintana, E. V., Davies, G. R., Silva Aguirre, V., Ragozzine, D., Riddle, R., Baranec, C., Basu, S., Chaplin, W. J., Christensen-Dalsgaard, J., Metcalfe, T. S., Bedding, T. R., Handberg, R., Stello, D., Brewer, J. M., Hekker, S., Karoff, C., Kolbl, R., Law, N. M., Lundkvist, M., Miglio, A., Rowe, J. F., Santos, N. C., Van Laerhoven, C., Arentoft, T., Elsworth, Y. P., Fischer, D. A., Kawaler, S. D., Kjeldsen, H., Lund, M. N., Marcy, G. W., Sousa, S. G., Sozzetti, A., and White, T. R. (2015). An Ancient Extrasolar System with Five Sub-Earth-size Planets. *ApJ*, 799:170.

Caselli, P., Benson, P. J., Myers, P. C., and Tafalla, M. (2002). Dense Cores in Dark Clouds. XIV. N_2H^+ (1-0) Maps of Dense Cloud Cores. *ApJ*, 572:238–263.

Casoli, J. and Masset, F. S. (2009). On the Horseshoe Drag of a Low-Mass Planet. I. Migration in Isothermal Disks. *ApJ*, 703:845–856.

Cassen, P. (1993). Why convective heat transport in the solar nebula was inefficient. In *Lunar and Planetary Science Conference*, volume 24 of *Lunar and Planetary Inst. Technical Report*, pages 261–262.

Chang, S.-H., Gu, P.-G., and Bodenheimer, P. H. (2010). Tidal and Magnetic Interactions Between a Hot Jupiter and its Host Star in the Magnetospheric Cavity of a Protoplanetary Disk. *ApJ*, 708:1692–1702.

Cieza, L. and Baliber, N. (2006). Testing the Disk Regulation Paradigm with Spitzer Observations. I. Rotation Periods of Pre-Main-Sequence Stars in the IC 348 Cluster. *ApJ*, 649:862–878.

Clarke, C., Gendrin, A., and Sotomayor, M. (2001). The dispersal of circumstellar discs: the role of the ultraviolet switch. *MNRAS*.

Crida, A. and Morbidelli, A. (2007). Cavity opening by a giant planet in a protoplanetary disc and effects on planetary migration. *MNRAS*, 377:1324–1336.

Crida, A., Morbidelli, A., and Masset, F. (2007). Simulating planet migration in globally evolving disks. *A&A*, 461:1173–1183.

D'Angelo, G., Durisen, R. H., and Lissauer, J. J. (2010). *Giant Planet Formation*, pages 319–346.

D'Angelo, G., Henning, T., and Kley, W. (2002). Nested-grid calculations of disk-planet interaction. *A&A*, 385:647–670.

Dittkrist, K.-M., Mordasini, C., Klahr, H., Alibert, Y., and Henning, T. (2014). Impacts of planet migration models on planetary populations. Effects of saturation, cooling and stellar irradiation. *A&A*, 567:A121.

Duffell, P. C., Haiman, Z., MacFadyen, A. I., D'Orazio, D. J., and Farris, B. D. (2014). The Migration of Gap-opening Planets is Not Locked to Viscous Disk Evolution. *ApJ*, 792:L10.

Dullemond, C. P., van Zadelhoff, G. J., and Natta, A. (2002). Vertical structure models of T Tauri and Herbig Ae/Be disks. *A&A*, 389:464–474.

Edgar, R. G. (2007). Giant Planet Migration in Viscous Power-Law Disks. *ApJ*, 663:1325–1334.

Flock, M., Dzyurkevich, N., Klahr, H., Turner, N. J., and Henning, T. (2011). Turbulence and Steady Flows in Three-dimensional Global Stratified Magnetohydrodynamic Simulations of Accretion Disks. *ApJ*, 735:122.

Fortier, A., Alibert, Y., Carron, F., Benz, W., and Dittkrist, K.-M. (2013). Planet formation models: the interplay with the planetesimal disc. *A&A*, 549:A44.

Fortier, A., Benvenuto, O. G., and Brunini, A. (2007). Oligarchic planetesimal accretion and giant planet formation. *A&A*, 473:311.

Fouchet, L., Alibert, Y., Mordasini, C., and Benz, W. (2012). Effects of disk irradiation on planet population synthesis. *A&A*, 540:A107.

Goldreich, P. and Tremaine, S. (1980). Disk-satellite interactions. *ApJ*, 241:425–441.

Goldreich, P. and Weber, S. V. (1980). Homologously collapsing stellar cores. *ApJ*, 238:991–997.

Goodman, A. A., Benson, P. J., Fuller, G. A., and Myers, P. C. (1993). Dense cores in dark clouds. VIII - Velocity gradients. *ApJ*, 406:528–547.

Guilet, J., Baruteau, C., and Papaloizou, J. C. B. (2013). Type I planet migration in weakly magnetized laminar discs. *MNRAS*, 430:1764–1783.

Gutermuth, R. A., Megeath, S. T., Pipher, J. L., Williams, J. P., Allen, L. E., Myers, P. C., and Raines, S. N. (2005). The Initial Configuration of Young Stellar Clusters: A K-Band Number Counts Analysis of the Surface Density of Stars. *ApJ*, 632:397–420.

Haisch, Jr., K. E., Lada, E. A., and Lada, C. J. (2001). Disk Frequencies and Lifetimes in Young Clusters. *ApJ*, 553:L153–L156.

Hasegawa, Y. and Pudritz, R. E. (2011). The origin of planetary system architectures - I. Multiple planet traps in gaseous discs. *MNRAS*, 417:1236–1259.

Hellary, P. and Nelson, R. P. (2012). Global models of planetary system formation in radiatively-inefficient protoplanetary discs. *MNRAS*, 419:2737–2757.

Hori, Y. and Ikoma, M. (2011). Gas giant formation with small cores triggered by envelope pollution by icy planetesimals. *MNRAS*, 416:1419–1429.

Horn, B., Lyra, W., Mac Low, M.-M., and Sándor, Z. (2012). Orbital Migration of Interacting Low-mass Planets in Evolutionary Radiative Turbulent Models. *ApJ*, 750:34.

Hubeny, I. (1990). Vertical structure of accretion disks - A simplified analytical model. *ApJ*, 351:632–641.

Hueso, R. and Guillot, T. (2005). Evolution of protoplanetary disks: constraints from DM Tauri and GM Aurigae. *A&A*, 442:703–725.

Ida, S. and Lin, D. N. C. (2004). Toward a deterministic model of planetary formation. i. a desert in the mass and semimajor axis distributions of extrasolar planets. *ApJ*, 604:388.

Ida, S. and Lin, D. N. C. (2008). Toward a deterministic model of planetary formation. iv. effects of type i migration. *ApJ*, 673:487.

Ida, S. and Lin, D. N. C. (2010). Toward a Deterministic Model of Planetary Formation. VI. Dynamical Interaction and Coagulation of Multiple Rocky Embryos and Super-Earth Systems around Solar-type Stars. *ApJ*, 719:810–830.

Jijina, J., Myers, P. C., and Adams, F. C. (1999). Dense Cores Mapped in Ammonia: A Database. *ApJS*, 125:161–236.

Jin, L. and Li, M. (2014). Diversity of Extrasolar Planets and Diversity of Molecular Cloud Cores. I. Semimajor Axes. *ApJ*, 783:37.

Johns-Krull, C. M., Valenti, J. A., Hatzes, A. P., and Kanaan, A. (1999). Spectropolarimetry of Magnetospheric Accretion on the Classical T Tauri Star BP Tauri. *ApJ*, 510:L41–L44.

Kley, W., Bitsch, B., and Klahr, H. (2009). Planet migration in three-dimensional radiative discs. *A&A*, 506:971–987.

Kley, W. and Dirksen, G. (2006). Disk eccentricity and embedded planets. *A&A*, 447:369–377.

Kratter, K. M., Matzner, C. D., and Krumholz, M. R. (2008). Global Models for the Evolution of Embedded, Accreting Protostellar Disks. *ApJ*, 681:375–390.

Kretke, K. A. and Lin, D. N. C. (2012). The Importance of Disk Structure in Stalling Type I Migration. *ApJ*, 755:74.

Lada, C. J. and Lada, E. A. (2003). Embedded Clusters in Molecular Clouds. *ARA&A*, 41:57–115.

Lubow, S. H., Seibert, M., and Artymowicz, P. (1999). Disk Accretion onto High-Mass Planets. *ApJ*, 526:1001–1012.

Lynden-Bell, D. and Pringle, J. E. (1974). The evolution of viscous discs and the origin of the nebular variables. *MNRAS*, 168:603.

Lyra, W., Paardekooper, S., and Mac Low, M. (2010). Orbital Migration of Low-mass Planets in Evolutionary Radiative Models: Avoiding Catastrophic Infall. *ApJ*, 715:L68–L73.

Malygin, M. G., Kuiper, R., Klahr, H., Dullemond, C. P., and Henning, T. (2014). Mean gas opacity for circumstellar environments and equilibrium temperature degeneracy. *A&A*, 568:A91.

Mamajek, E. E. (2009). Initial Conditions of Planet Formation: Lifetimes of Primordial Disks. In Usuda, T., Tamura, M., and Ishii, M., editors, *American Institute of Physics Conference Series*, volume 1158 of *American Institute of Physics Conference Series*, pages 3–10.

Marois, C., Macintosh, B., Barman, T., Zuckerman, B., Song, I., Patience, J., Lafrenière, D., and Doyon, R. (2008). Direct Imaging of Multiple Planets Orbiting the Star HR 8799. *Science*, 322:1348–.

Marois, C., Zuckerman, B., Konopacky, Q. M., Macintosh, B., and Barman, T. (2010). Images of a fourth planet orbiting HR 8799. Nature, 468:1080–1083.

Masset, F. S. (2002). The co-orbital corotation torque in a viscous disk: Numerical simulations. *A&A*, 387:605–623.

Masset, F. S. and Casoli, J. (2009). On the Horseshoe Drag of a Low-Mass Planet. II. Migration in Adiabatic Disks. *ApJ*, 703:857–876.

Masset, F. S. and Casoli, J. (2010). Saturated Torque Formula for Planetary Migration in Viscous Disks with Thermal Diffusion: Recipe for Protoplanet Population Synthesis. *ApJ*, 723:1393–1417.

Masset, F. S., D'Angelo, G., and Kley, W. (2006). On the Migration of Protogiant Solid Cores. *ApJ*, 652:730–745.

Mayor, M., Marmier, M., Lovis, C., Udry, S., Ségransan, D., Pepe, F., Benz, W., Bertaux, J. ., Bouchy, F., Dumusque, X., Lo Curto, G., Mordasini, C., Queloz, D., and Santos, N. C. (2011). The HARPS search for southern extra-solar planets XXXIV. Occurrence, mass distribution and orbital properties of super-Earths and Neptune-mass planets. *ArXiv e-prints*, page 1109.2497.

Mayor, M. and Queloz, D. (1995). A jupiter-mass companion to a solar-type star. *Nature*, 378:355.

Megeath, S. T., Gutermuth, R., Muzerolle, J., Kryukova, E., Hora, J. L., Allen, L. E., Flaherty, K., Hartmann, L., Myers, P. C., Pipher, J. L., Stauffer, J., Young, E. T., and Fazio, G. G. (2015). The Spitzer Space Telescope Survey of the Orion A and B Molecular Clouds II: the Spatial Distribution and Demographics of Dusty Young Stellar Objects. *ArXiv e-prints*.

Miguel, Y. and Brunini, A. (2008). Core instability models of giant planet accretion and the planetary desert. *MNRAS*, 387:463.

Mizuno, H., Nakazawa, K., and Hayashi, C. (1978). Instability of a gaseous envelope surrounding a planetary core and formation of giant planets. *Progress of Theoretical Physics*, 60:699.

Mordasini, C., Alibert, Y., and Benz, W. (2009a). Extrasolar planet population synthesis i: Method, formation tracks and mass-distance distribution. *A&A*, 501:1139–1160.

Mordasini, C., Alibert, Y., Benz, W., and Naef, D. (2009b). Extrasolar planet population synthesis ii: Statistical comparison with observation. *A&A*, 501:1161–1184.

Mordasini, C., Alibert, Y., Georgy, C., Dittkrist, K.-M., Klahr, H., and Henning, T. (2012a). Characterization of exoplanets from their formation II: The planetary mass-radius relationship. *ArXiv e-prints*, page 1206.3303.

Mordasini, C., Alibert, Y., Klahr, H., and Henning, T. (2012b). Characterization of exoplanets from their formation I: Models of combined planet formation and evolution. *ArXiv e-prints*, page 1206.6103.

Mordasini, C., Dittkrist, K.-M., Alibert, Y., Klahr, H., Benz, W., and Henning, T. (2011). Application of recent results on the orbital migration of low mass planets: convergence zones. In Sozzetti, A., Lattanzi, M. G., and Boss, A. P., editors, *IAU Symposium*, volume 276 of *IAU Symposium*, pages 72–75.

Mordasini, C., Klahr, H., Alibert, Y., Benz, W., and Dittkrist, K.-M. (2010). Theory of planet formation. In Wolf, S., editor, *Circumstellar Disks and Planets: Science Cases for the Second Generation VLTI Instrumentation*, page [arXiv:1012.5281].

Motte, F., Andre, P., and Neri, R. (1998). The initial conditions of star formation in the rho Ophiuchi main cloud: wide-field millimeter continuum mapping. *A&A*, 336:150–172.

Myers, P. C. (2005). Centrally Condensed Collapse of Starless Cores. *ApJ*, 623:280–290.

Myers, P. C. (2008). Protostar Mass due to Infall and Dispersal. *ApJ*, 687:340–353.

Nagasawa, M., Ida, S., and Bessho, T. (2008). Formation of Hot Planets by a Combination of Planet Scattering, Tidal Circularization, and the Kozai Mechanism. *ApJ*, 678:498–508.

Nakamoto, T. and Nakagawa, Y. (1994). Formation, early evolution, and gravitational stability of protoplanetary disks. *ApJ*, 421:640–650.

Natta, A., Testi, L., and Randich, S. (2006). Accretion in the ρ-Ophiuchi pre-main sequence stars. *A&A*, 452:245–252.

Paardekooper, S., Baruteau, C., Crida, A., and Kley, W. (2010). A torque formula for non-isothermal type I planetary migration - I. Unsaturated horseshoe drag. *MNRAS*, 401:1950–1964.

Paardekooper, S.-J., Baruteau, C., and Kley, W. (2011). A torque formula for non-isothermal Type I planetary migration - II. Effects of diffusion. *MNRAS*, 410:293–303.

Paardekooper, S.-J. and Mellema, G. (2006). Halting type I planet migration in non-isothermal disks. *A&A*, 459:L17–L20.

Paardekooper, S.-J. and Mellema, G. (2008). Growing and moving low-mass planets in non-isothermal disks. *A&A*, 478:245–266.

Papaloizou, J. C. B., Nelson, R. P., and Snellgrove, M. D. (2004). The interaction of giant planets with a disc with mhd turbulence - iii. flow morphology and conditions for gap formation in local and global simulations. *MNRAS*, 350:829.

Papaloizou, J. C. B. and Terquem, C. (1999). Critical protoplanetary core masses in protoplanetary disks and the formation of short-period giant planets. *ApJ*, 521:823.

Perri, F. and Cameron, A. G. W. (1974). Hydrodynamic instability of the solar nebula in the presence of a planetary core. *Icarus*, 22:416.

Pollack, J. B., Hubickyj, O., Bodenheimer, P., Lissauer, J. J., Podolak, M., and Greenzweig, N. C. (1996). Formation of the giant planets by concurrent accretion of solids and gas. *Icarus*, 124:62.

Pudritz, R. E. and Matt, S. (2014). The Early History of Stellar Spin: the Theory of Accretion onto Young Stellar Objects. In *European Physical Journal Web of Conferences*, volume 64 of *European Physical Journal Web of Conferences*, page 4001.

Pudritz, R. E., Ouyed, R., Fendt, C., and Brandenburg, A. (2007). Disk Winds, Jets, and Outflows: Theoretical and Computational Foundations. *Protostars and Planets V*, pages 277–294.

Rasio, F. A. and Ford, E. B. (1996). Dynamical instabilities and the formation of extrasolar planetary systems. *Science*, 274:954–956.

Ruden, S. P. and Pollack, J. B. (1991). The dynamical evolution of the protosolar nebula. *ApJ*, 375:740–760.

Sándor, Z., Lyra, W., and Dullemond, C. P. (2011). Formation of Planetary Cores at Type I Migration Traps. *ApJ*, 728:L9.

Saumon, D., Chabrier, G., and van Horn, H. M. (1995). An Equation of State for Low-Mass Stars and Giant Planets. *ApJS*, 99:713.

Schwarzschild, M. (1958). *Structure and evolution of the stars.*

Shakura, N. I. and Sunyaev, R. A. (1973). Black holes in binary systems. observational appearance. *Astron. Astrophys.*, 24:337.

Shu, F. H. (1977). Self-similar collapse of isothermal spheres and star formation. *ApJ*, 214:488–497.

Siess, L., Dufour, E., and Forestini, M. (2000). An internet server for pre-main sequence tracks of low- and intermediate-mass stars. *A&A*, 358:593–599.

Stahler, S. W. and Palla, F. (2005). *The Formation of Stars*. Wiley-VCH, 1st edition.

Starczewski, S., Gawryszczak, A. J., Wunsch, R., and Rozyczka, M. (2007). Hot Jupiters and Central Cavities of Protoplanetary Disks. Acta Astron., 57:123–138.

Tanaka, H., Takeuchi, T., and Ward, W. R. (2002). Three-dimensional interaction between a planet and an isothermal gaseous disk. i. corotation and lindblad torques and planet migration. *ApJ*, 565:1257.

Testi, L., Birnstiel, T., Ricci, L., Andrews, S., Blum, J., Carpenter, J., Dominik, C., Isella, A., Natta, A., Williams, J. P., and Wilner, D. J. (2014). Dust Evolution in Protoplanetary Disks. *Protostars and Planets VI*, pages 339–361.

Thommes, E. W., Matsumura, S., and Rasio, F. A. (2008). Gas disks to gas giants: Simulating the birth of planetary systems. *Science*, 321(5890):814–817.

Uribe, A. L., Klahr, H., Flock, M., and Henning, T. (2011). Three-dimensional Magnetohydrodynamic Simulations of Planet Migration in Turbulent Stratified Disks. *ApJ*, 736:85.

Veras, D. and Armitage, P. J. (2004). Outward migration of extrasolar planets to large orbital radii. *MNRAS*, 347:613.

Visser, R., van Dishoeck, E. F., Doty, S. D., and Dullemond, C. P. (2009). The chemical history of molecules in circumstellar disks. I. Ices. *A&A*, 495:881–897.

Yamada, K. and Inaba, S. (2012). Type I migration in optically thick accretion discs. *MNRAS*, 424:2746–2756.

Yorke, H. W. and Bodenheimer, P. (2008). Theoretical Developments in Understanding Massive Star Formation. In Beuther, H., Linz, H., and Henning, T., editors, *Massive Star Formation: Observations Confront Theory*, volume 387 of *Astronomical Society of the Pacific Conference Series*, page 189.

Acknowledgment

In no special order:
I thank the International Max Planck Research School for Astronomy and Cosmic Physics at the University of Heidelberg.
I thank the Max Planck Institute of Astronomy for the financial support and providing access to the computer cluster batchelor.
I thank Paul Molliere, Garbriel Marleau, Mykola Malygin, Andreas Schreiber, Christoph Mordasini, Hubert Klahr and all those others I talked to and discussed my work with.
I also thank all those who read part of this thesis and help with countless suggestions and support.
Especially I thank my girlfriend Sabine Schott for her support and patience we me. I could not have done it without her.